Understanding of edge and screw dislocations in nanostructures by modeling and simulations

A DISSERTATION
SUBMITTED TO THE FACULTY OF THE GRADUATE SCHOOL
OF THE UNIVERSITY OF MINNESOTA
BY

Evgeniya Dontsova

IN PARTIAL FULFILLMENT OF THE REQUIREMENTS
FOR THE DEGREE OF
Doctor of Philosophy

Traian Dumitrică

January, 2013

© Evgeniya Dontsova 2013
ALL RIGHTS RESERVED

Acknowledgements

There are many people whose contribution to this work I would like to acknowledge. First of all I would like to gratefully thank my adviser Professor Traian Dumitrică for his continuos support and encouragement throughout my graduate studies. His guidance helped me to overcome challenging problems and succeed in the formulated research projects. The completion of this dissertation would not have been possible without his generous efforts.

I would like to express my gratitude to Professor Ballarini for useful discussions and suggestions during my graduate program. I am thankful to Professors William W. Gerberich, Steven Girshick, Rusen Yang and Roberto Ballarini for serving on my thesis committee. Their efforts in reviewing this dissertation are greatly appreciated. I also would like to thank the former and present members of the Professor Dumitrică's group, including Dong-Bo Zhang and Ilia Nikiforov, for helping me with the available computational codes, giving useful instructions and answering to my numerous questions especially at the initial stage.

Besides, I am very grateful to all teachers who were instructing me during the undergraduate and graduate programs respectively at Novosibirsk State University and the University of Minnesota. The knowledge that they helped me to gain during the educational process became an essential component in fulfillment of this work. I also would like to acknowledge the financial support provided by Mechanical Engineering Departmental Fellowship and Doctoral Dissertational Fellowship from the University of Minnesota. Finally, special thanks go to my parents for always supporting my efforts and desire to study.

Abstract

The role of the extended dislocation defects in nanostructures only recently began to be explored. In bulk materials, dislocations are modeled only away from their cores within the framework of the continuum mechanics. It is known that applying continuum modeling in the core region leads to divergences. In nanostructures, the core region dominates and new investigation methods are needed. This work contributes in combination with recent experimentation to the fundamental understanding of the role of dislocations in carbon and zinc oxide nanostructures, by using atomistic methods. In quasi-zero-dimensional structures, thesis describes the first attempt to rationalize dislocation processes in carbon nano-onions. Experiments show that carbon nano-onions exhibit an unusual dislocation dynamics (relative to those of the crystalline bulk phase) with unexpected attraction of the outer edge dislocation towards the core. Atomistic calculations combined with rigorous energy analysis attribute this behavior to an unusual inward driving force on the outer edge dislocation associated with a reduction in the number of dangling bonds. This finding has various implications, especially for understanding the growth process of carbon nano-onions. Moving on to quasi-one-dimensional nanostructures, we study the stability of screw-dislocated zinc oxide structures in the wurtzite phase with a symmetry-adapted molecular dynamics methodology, which introduces a significant simplification in the simulation domain size by accounting for the helical symmetry explicitly. The goal is to provide the theoretical support for a universal screw-dislocation-driven growth mechanism suggested by recent experiments. Moreover, the effects of axial screw dislocations on the electronic properties in helical zinc oxide nanowires and nanotubes are explored. We demonstrate significant screw-dislocation-induced band gap modifications that originate in the highly distorted cores. Finally, using the same objective technique, we investigate the stability against torsional deformations of quasi-one-dimensional one-atom thick graphene nanoribbons with bare, F-, and OH-saturated armchair edges. The prevalence of twisted nanoribbons prompted the construction of a simple phenomenological model inspired from the Landau phase transition theory. This model is based on the atomistic data and gives the structural parameters of the nanoribbon as functions of its edge chemistry and axial strain.

Contents

List of Tables

List of Figures

Chapter 1

Introduction

Due to their diverse range of applications, from energy conversion to nanoelectromechanical devices, nanostructures are of enormous importance today. Dislocations, known as the extended line defects [8], are recently realized to play crucial role in the mechanical response and growth of nanostructures. For example, it was recognized that screw dislocations provide an important and universal catalyst-free growth mechanism for quasi-one-dimensional nanostructures [2]. Because of the inherent difficulties encountered at the nanoscale, experimental characterization of these materials and identification of dislocations are possible but often problematic. This represents an opportunity for using computer simulation techniques to dramatically advance and accelerate the progress in the area of nanomechanics [9].

Dislocations distort the crystal structure and represent the area, where atoms are shifted from their positions in the perfect crystal. They are currently modeled with continuum mechanics methods, which do not explicitly account for the discrete nature of the material and are even not applicable in the core region of the dislocation (region of highest distortions) that leads to divergences. However, this core region is dominant in nanostructures. Therefore, atomistic investigation approaches are required in order to study such defects with needed atomic-scale resolution.

In the current work the effect of dislocations is studied in different nanostructures, including carbon nano-onions, zinc oxide (ZnO) nanotubes (NTs) and nanowires (NWs). Besides, the role of torsional deformation as a stabilization mechanism is investigated in one-atom thick graphene nanoribbons (GNRs). The peculiarities and importance of

the considered nanostructures are discussed in the following paragraphs.

An idealized carbon nano-onion consists of concentric icosahedral fullerenes [10, 11], starting from buckminsterfullerene C_{60} [12]. Fullerene is defined as a molecule composed entirely of carbon atoms which usually has a closed shape structure. A unique sequence of icosahedral fullerenes $C_{60}@...@C_{60n^2}$ (here n is a shell number), which maintains the constant inter-shell distance close to equilibrium spacing between the layers in graphite, represents the most stable configuration for carbon nano-onion [13]. Because of their outstanding chemical and physical properties, carbon nano-onions have been found to be useful in the range of potential applications such as solid lubrication [14], gas and energy storage [15], electro-optical devices [16], ect. Therefore, the analysis and understanding of possible defects including dislocations in these structures becomes relevant.

Nanostructured tubular materials have attracted vast attention for almost two decades. In addition to carbon (C) NTs, first reported in 1991 [17], a large number of inorganic NT structures have been synthesized from both layered, such as tungsten disulphide [18], molybdenum disulfide [19], boron nitride [20], and non-layered materials, for instance gallium nitrite [21], aluminum nitride [22], zinc oxide [3, 23], etc. While the inorganic NTs formed from layered materials can be typically imagined as layers rolled into cylindrical structures, the NTs made out of non-layered materials are essentially pristine one-dimensional mono-crystalline structures possessing a central vacant space. In this work we focus on ZnO material, which is an important semiconductor well-suited for a large number of applications [24], including solar cells [25], light-emitted diodes [26], optical switches [27], etc. An understanding of the structure-electronic properties relationship is crucial for advancing these applications. However, the applicability of standard microscopic simulations methods for screw-dislocated structures is challenging due to the difficulties associated with handling translational symmetry, which requires some new approaches.

GNRs are the thin strips of graphene layer with widths in the range of nanometers. These structures were originally introduced theoretically to model the edge and nanoscale size effect in graphene [28]. Nowadays, GNRs were synthesized experimentally by different techniques, for instance, via chemical routes applied to graphite material [29] or unzipping of carbon nanotubes [30, 31]. Due to their attractive tunable electronic

properties, GNR structures are widely investigated for potential nanoelectronic applications [32]. Consequently, there is a growing need to understand their stability and electronic properties.

By using the atomistic simulation techniques, the objective of this work is to investigate in connection with the recent experimental studies the role of dislocations in C and ZnO nanostructures in relation with their mechanical and electronic properties, as well as analyze the stability and electronic response to twist deformation of GNRs with different edge types. The structure of the dissertation is described in details below.

- In Chapter 1 the main goals pursued in this thesis are introduced. The importance and relevance of the considered topics are also discussed.

- Chapter 2 briefly presents the concept of dislocations. In the beginning the rigorous definition of a dislocation is given, then the continuum description of dislocations is reviewed. After that, the screw-dislocation-driven growth mechanism is explained. Finally, some examples of dislocations in nanostructures are specified.

- Chapter 3 describes in details the atomistic simulation methods used in this thesis. It provides a review of two computational techniques employed in this work, namely, classical molecular dynamics (MD) based on analytical potential method and non-standart symmetry-adapted tight-binding (TB) MD that can handle helical and angular symmetries aside from widely used translation symmetry.

- Chapter 4 follows the study of the dislocation processes in carbon nano-onions. First, the possible types of dislocations in nano-onions are discussed. Next, the comparison between experimentally-observed dislocation processes and atomistic simulations are presented. Afterward, the continuum level modeling, aimed to explain the investigated behavior, is introduced and conclusions are made. Main results of this work were published in [33].

- Chapter 5 contains the investigations of mechanical and electronic properties of screw-dislocated ZnO NTs and NWs. It starts with the study of the role of axial screw dislocations in one-atom-thin ZnO NTs, specifically, intrinsic twist effect and band gap variation with curvature and chirality are revealed [34]. The thicker ZnO NTs and NWs are considered next. Besides the stability issues of screw

dislocations [35], their influence on electronic structure is presented [36]. Finally, the main findings are summarized.

- In Chapter 6 the study of finite-size and edge effects in monolayer GNRs with bare, F-, and OH-edges is demonstrated. In the beginning the latest works on the subject of the GNR's stability are reviewed. Then the atomistic simulation results, showing the prevalence of twisted ground state structures, are presented. Next, the proposed phase transition model, which adequately captures the most important features obtained in simulations, is described. The band gap variation of F- and OH-GNRs with twist angle is also included. All results, reported in [37], are summarized at the end.

- Chapter 7 gives a final discussion of the presented works in the thesis. The main results and their specific significance are considered.

Publications

- **E. Akatyeva**, J. Y. Huang, and T. Dumitrică. Edge-mediated dislocation processes in multishell carbon nano-onions? *Physical Review Letters*, 105(10):106102, 2010.

- T. Anderson, **E. Akatyeva**, I. Nikiforov, D. Potyondy, R. Ballarini, and T. Dumitrică. Toward distinct element method simulations of carbon nanotube systems. *ASME Journal of Nanotechnology in Engineering and Medicine*, 1(4):041009, 2010.

- D.-B. Zhang, **E. Akatyeva**, and T. Dumitrică. Bending ultrathin graphene at the margins of continuum mechanics. *Physical Review Letters*, 106(25):255503, 2011.

- D.-B. Zhang, **E. Akatyeva**, and T. Dumitrică. Helical BN and ZnO nanotubes with intrinsic twisting: An objective molecular dynamics study. *Physical Review B*, 84(11):115431, 2011.

- **E. Akatyeva** and T. Dumitrică. Eshelby twist and magic helical zinc oxide nanowires and nanotubes. *Physical Review Letters*, 109(3):035501, 2012.

- **E. Akatyeva**, L. Kou, I. Nikiforov, Th. Frauenheim, and T. Dumitrică. Electrically active screw dislocations in helical ZnO and Si nanowires and nanotubes. *ACS Nano*, 6(11):10042–10049, 2012.

- **E. Akatyeva** and T. Dumitrică. Chiral graphene nanoribbons: Objective molecular dynamics simulations and phase transition modeling. *Journal of Chemical Physics* 137(23): 234702, 2012.

Chapter 2

Dislocations

Because of their crucial roles played in the mechanical response and growth of crystalline structures, the extended line defects referred to as dislocations, have been long investigated [8]. Dislocations are mainly studied in relation with the mechanical properties of materials. Dislocations allow plastic deformations to occur at lower applied stresses since they permit glide of one entire crystal plane over the one below in a discrete rather than a coherent way. Besides, the motion, multiplication, and interaction of dislocations cause strain hardening, a common phenomenon in which continued deformation increases the strength of a crystal. The strength and ductility, thereby the mechanical behavior of a crystal, are controlled by dislocations. What is less commonly appreciated is that dislocations are of importance for crystal growth. This is because the screw dislocation offers a non-vanishing growth step on the otherwise flat surface allowing the growth to advance in a spiral manner without the need for nucleation of a new layer [4].

A brief introduction to a concept of dislocations, including the important aspects related to the dislocation presence in crystalline materials, is given in this Chapter. First, it presents the dislocation definition, then it reviews the continuum description of dislocations, discussing two crucial mechanical effects: Frank model for hollowing of the screw dislocation with large Burgers vector in bulk materials and Eshelby twist caused by screw dislocation in a thin cylindrical rod. Next, the screw-dislocation-driven growth mechanism is described. Finally, examples of dislocations in graphene-based nanostructures are illustrated.

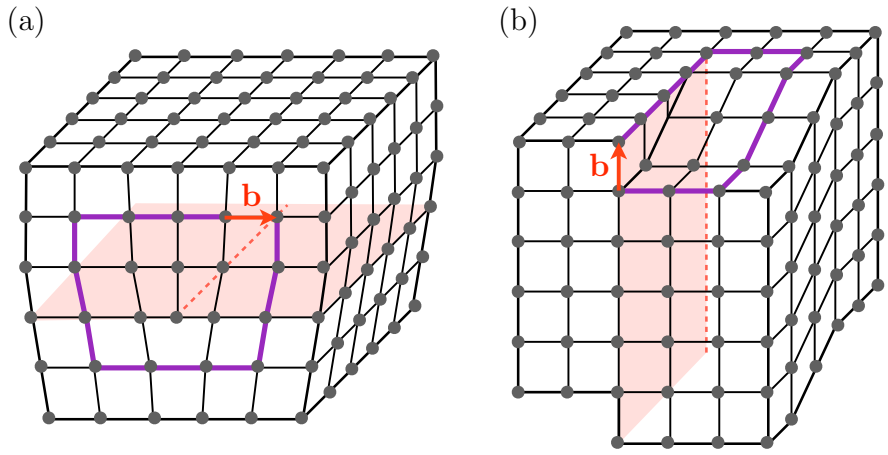

Figure 2.1: Schematic representation of (a) edge and (b) screw dislocations in a simple cubic crystalline material, where filled circles denote the lattice points of a crystal, **b** is a Burgers vector, hatched area and dashed line illustrate the slip plane and dislocation line, respectively.

2.1 Dislocation concept

Technically, dislocation can be defined as a boundary between deformed and undeformed regions in the crystalline structure. In other words, dislocation line represents the slip front of propagation of a line defect. The Burgers vector, which is generally used to define a dislocation in a crystal, depicts the direction and amount of slip. Its magnitude is a characteristic discontinuity of displacement caused by dislocation. Burgers vector can be identified by making a closed circuit around the suspected dislocation. The circuit is created by jumping from one lattice point to neighboring point until the starting point is reached again, where each jump is associated with a jump in a perfect crystal of the same structure, as shown in Fig. 2.1(a) and (b). If the circuit fails to close, then it does surround by a dislocation, and the lattice vector needed to complete this circuit is the Burgers vector of the dislocation [38].

Dislocation types are generally characterized by the relative orientation between the Burgers vector and dislocation line. There are two basic types of dislocations, the edge and screw dislocations, which are just extreme forms of the possible dislocations. In the

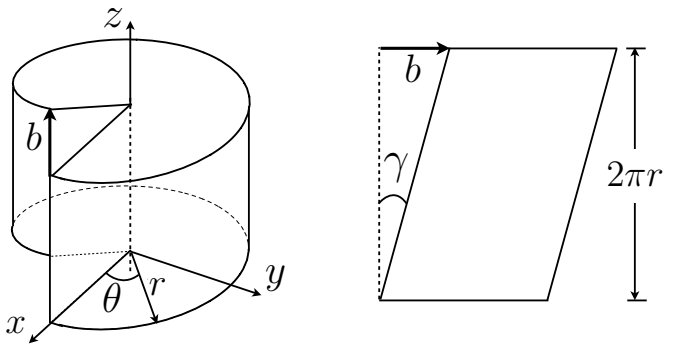

Figure 2.2: Schematic representation of a cylinder that contains an axial screw dislocation lying along z-axis (left) and its unfolded view showing the strain caused by a screw dislocation (right).

situation, when the Burgers vector is perpendicular, parallel or an arbitrary oriented with respect to the dislocation line, the corresponding dislocation is of edge, screw or mixed character. Figure 2.1(a) depicts the edge dislocation, which is represented by an extra half-plane of atoms "defect" in a crystal lattice. This extra half-plane of atoms causes the region above it to be in compression and the region below to be in tension. The screw dislocation, depicted in Fig. 2.1(b), can be created by cutting a crystal along a plane and slipping one half across the other by a Burgers vector.

2.2 Continuum description of dislocations

Dislocation distorts the crystal structure and produces an elastic field around itself [8]. In all regions of the crystal except the dislocation core, the stress produced by a dislocation is small enough to be treated with a linear theory of elasticity. For simplicity let us consider the case with a screw dislocation and describe the generated strain field. The cylindrical coordinate system (r, θ, z) is a convenient choice to study the tubular structure with dislocation lying parallel its axis (z-axis) and sited at the origin, as illustrated in Fig. 2.2. It is expected, that the displacement at any point should be parallel to the dislocation line. Radial symmetry suggests a displacement u_z, the shear strain

$\gamma_{\theta z}$ and stress $\sigma_{\theta z}$ at a radial distance r to be given by

$$u_z = \frac{b\theta}{2\pi}, \qquad \gamma_{\theta z} = \frac{b}{2\pi r}, \qquad \sigma_{\theta z} = G\gamma_{\theta z}, \tag{2.1}$$

where G is the shear modulus of a material. Elastic strain energy per unit length, associated with the presence of screw dislocation in a crystal, can be calculated by integrating the strain energy density over the surface and adding the core energy term E_c (measured per length), which is caused by the high distortions within the core region, resulting in the following expression

$$E_{\text{screw}} = \frac{Gb^2}{4\pi} \ln \frac{R}{r_c} + E_c, \tag{2.2}$$

where R and r_c denote the outer dimension of the structure and the dislocation core size, respectively. The same type of analysis can be done for a generic dislocation of mixed type. The knowledge of the elastic field produced by a dislocation allows to evaluate its interaction with elastic fields from other defects or external forces, and hence, describe processes involving the dislocation motion and further understand the mechanical behavior of the system in question. It should be noted that deformation in the core region, usually estimated as a cutoff radius with the size of a few Burgers vectors, cannot be properly captured by the continuum elasticity treatment. The behavior in the core region is rarely studied and, at least in principle, it should be described by explicitly accounting for the nanomechanics at the atomic scale. While in bulk crystals with dimensions much larger than r_c, this region is less important, in nanoscale structures with dimension on the same order as r_c, this region could become important.

2.2.1 Screw dislocations in bulk and nanoscale structures

Defects in the form of hollow cylindrical pores, which are usually called pipes, were numerously observed in single crystalline materials [1]. Such pipes are also called hollow core dislocations because of their location at the center of a screw dislocation involved in the growth process. Pipes grow together with the crystal and are parallel to the growth direction. Figure 2.3 shows experimentally observed images of hollow core dislocation in bulk material of SiC [1], as well as schematics of the hollow core dislocation forming during screw-dislocation-driven growth.

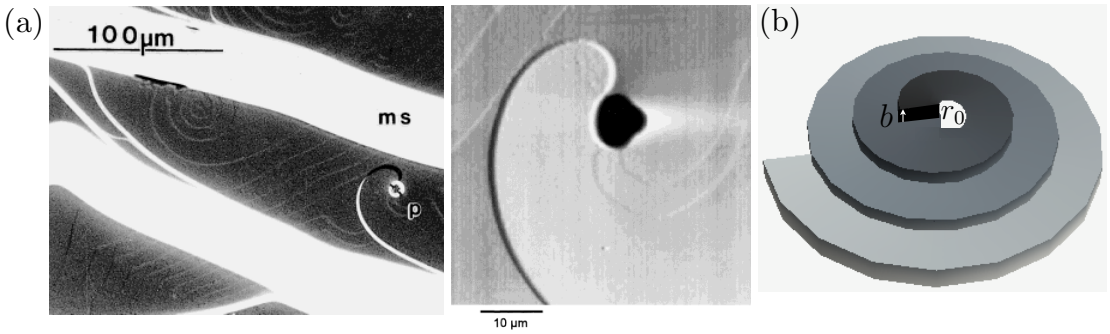

Figure 2.3: (a) Experimental images of growth surface of SiC showing a micropipe (p) formation (left) and enlarged view on this micropipe (right), taken from [1]. (b) Schematic representation of the hollow core screw dislocation in bulk material, where the core radius r_0 and Burgers vector **b** are shown.

An explanation for the pipe formation in bulk materials was given by F.C. Frank in 1951 [39]. He showed that for a screw dislocation with large Burgers vector a state of equilibrium exists, in which the core of the dislocation is an empty tube. Frank model predicts the equilibrium radius for a pipe from the balance between elastic energy due to screw dislocation and surface energy of the formed tube. When Burgers vector exceeds some critical value, it is energetically more favorable for dislocation to become hollow by removing the crystalline material adjacent to the dislocation line and creating an additional surface in the form of hollow tube. The relationship between the magnitude of Burgers vector b and the equilibrium hollow core radius r_0 for a stable pipe can be expressed in the following form

$$b = \sqrt{\frac{8\pi^2 \gamma r_0}{G}}, \tag{2.3}$$

where γ represents the specific surface energy and some restrictions are applied to the magnitude of Burgers vector [39].

The effect of the screw dislocation presence in one-dimensional structures, such as thin rods, was studied by J.D. Eshelby in 1953 [40]. He found that the stress field of an axial screw dislocation in a cylindrical rod causes the torque, which is balanced by twisting. This phenomenon is known as Eshelby twist. Figure 2.4 schematically illustrates Eshelby twist effect in a dislocated cylindrical rod and tube structures. According to elasticity theory, the twist rate α (the twist of lattice in radians per unit length) in a

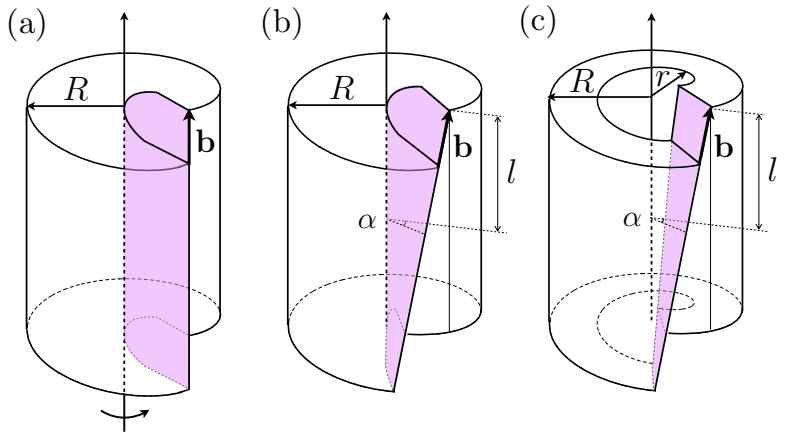

Figure 2.4: The representation of an axial screw dislocation with Burgers vector **b** in tubular structures. (a) Dislocated rod of radius R with fixed ends. (b) One of the ends of the rod is free to rotate, resulting in Eshelby twist, where α and l are the twist rate and unit length, respectively. (c) Hollow tube containing an axial screw dislocation with one free to rotate end, where r is the inner radius of this tube.

thin cylindrical structure in terms of its geometric parameters (outer and inner radii, R and r) and the screw component of the Burgers vector b can be expressed as

$$\alpha = \frac{cb}{\pi(R^2 + r^2)}. \tag{2.4}$$

Here c is a constant factor that depends on the shape of the cross-section, for circular cross-section $c = 1$, while for the square shape with the same cross-sectional area it deviates from unity only by small amount (about 5%) [41].

This phenomenon was investigated for a long time for whiskers, and there are numerous experimental studies, which demonstrate the twist in a whisker along its axis [42, 43]. Recently Eshelby twist phenomenon was directly visualized on chiral branched nanowire structures (PbS, PbSe), where they observed the so-called pine tree nanowires, consisting of the central trunk and branches, which are helically rotated, highlighting the twist of the central trunk [44, 45]. Figure 2.5 illustrates the observed pine tree nanowire with rotated branches, as well as the equilibrium structure of ZnO nanotube containing hollow core screw dislocation.

It is clear that both dislocation hollowing due to high strains within the core region and shear strain relief through twisting deformation of the whole structure are important

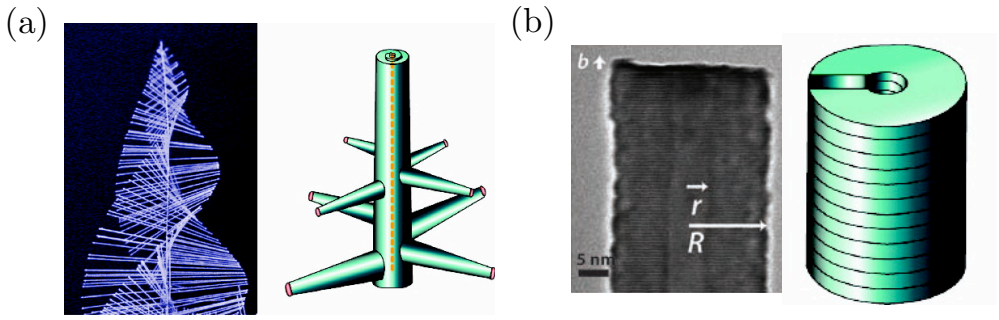

Figure 2.5: (a) Electron microscopy image of a pine tree nanowire of PbS (left) and schematic representation of screw-dislocation-driven trunk growth combined with slower epitaxial vapor-liquid-solid-driven branch growth (right), taken from [2]. (b) Experimental image of the screw-dislocated ZnO nanotube (left) and its schematic representation (right), taken from [3].

for screw-dislocated tubular structures, that are the subject of our interest. In order to rationalize the stability of these structures Frank model, which characterizes the stability of screw dislocations in bulk crystalline material, should be modified by accounting for the strain energy relief through Eshelby twist. One may obtain the following relationship between the magnitude of Burgers vector and equilibrium radius

$$b = \sqrt{\frac{8\pi^2\gamma r_0}{G}}\frac{R^2 + r_0^2}{R^2 - r_0^2}, \tag{2.5}$$

performing the total energy minimization procedure [46].

2.3 Screw-dislocation-driven growth

The role of dislocations in crystal growth is usually less recognized because of the slow growth rates. A crystal growth theory based on screw dislocations was introduced by F.C. Frank in 1949 [47]. The screw dislocation implies the non-vanishing growth step on the surface because this step can advance in a spiral manner without the need for nucleation of a new layer. Figure 2.6 schematically demonstrates a screw-dislocation-driven crystal growth mechanism. When a growth step advances, a new step is generated in the perpendicular to the original step direction, therefore, the growth step is always presented on the surface. Screw-dislocation-driven growth mechanism was well studied theoretically [48] and experimentally [46, 42, 43] for whiskers, but now it is realized as

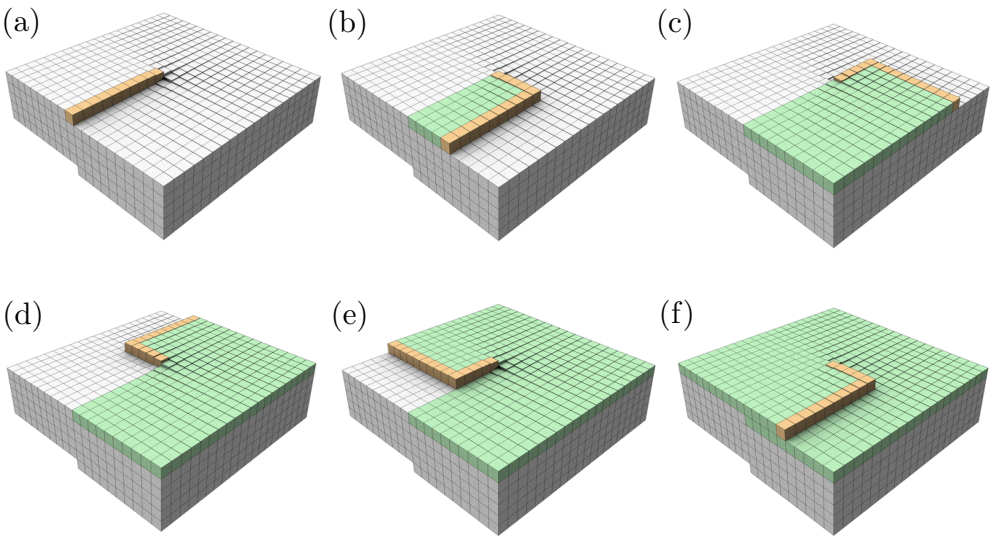

Figure 2.6: (a)-(f) Illustration of a crystal growth around a screw dislocation. The growth steps are shown in yellow and newly grown surfaces are in green color. The figure was taken from [4].

an important and appropriate catalyst-free growth mechanism for quasi-one-dimentional nanostructures [2], which are known by their diverse range of applications and, hence, they are intensively investigated these days.

The growth mechanism of single-crystal nanotubes is usually thought to be unrelated to that of nanowires. However, very recent works suggest that both nanowires [2] and nanotubes [2, 6] can grow via a common mechanism of the propagation of an axial screw dislocation. According to classical crystal growth theory, the supersaturation of a system defines the growth mechanism of a crystal. At low supersaturation a dislocation-driven spiral growth prevails, at intermediate a layer-by-layer growth mechanism is followed, and at high supersaturation a dendritic growth becomes dominant. Screw dislocation line defects, frequently presented in crystalline materials, by intersecting with the crystal surface make steps, that propagate as spirals, and thus become an endless source of crystal steps and enable crystal growth at low supersaturation conditions. The theoretical model for dislocation-driven crystal growth, which is known as

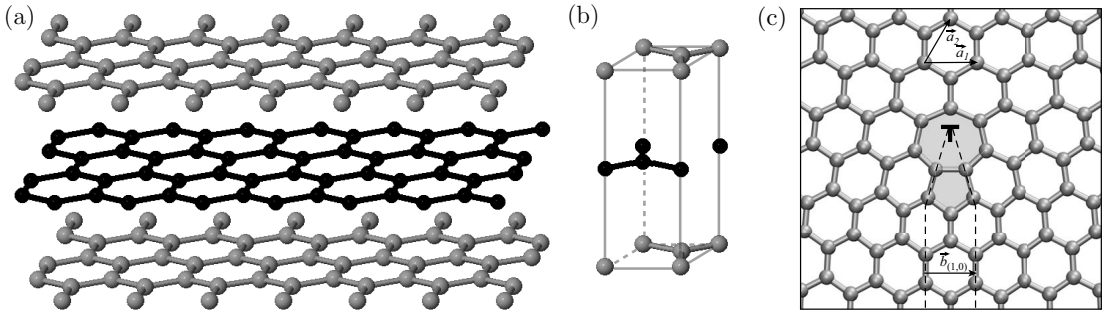

Figure 2.7: (a) Side view of layer stacking in graphite structure (called AB stacking) and (b) graphite's unit cell. (c) Atomic structure of the edge dislocation core, comprised of pentagon-heptagon pair, in two-dimensional graphene, where $\vec{a_1}$ and $\vec{a_2}$ are the basis vectors, this picture was taken from [5].

the Burton-Cabrera-Frank theory [48], predicts that the growth rate at low supersaturation regime is proportional to the magnitude of the Burgers vector. At this point, atomic-level examination of the structural stability of dislocated nanowires and nanotubes becomes important for understanding this growth mechanism at the nanoscale.

2.4 Examples of dislocations in graphite materials

The role of the dislocations in nanostructures only recently began to be explored. Because dislocations are conceptualized as extended defects, it is counterintuitive that they may be even present in quasi zero-dimentional and quasi one-dimentional structures. For this reason we next illustrate examples of known dislocations that have been already proved to be highly important at the nanoscale.

Graphite is generally considered as a model material to understand dislocations. In fact, an early work on natural graphite provided factual evidence for the existence of screw dislocations [49]. Graphite material is composed of parallel-stacked graphene layers and it has hexagonal crystal structure with two atom basis and four atoms per unit cell, as shown in Fig. 2.7(a) and (b). The possible dislocations in graphite system are classified with respect to the direction of Burgers vector and dislocation line as

follows [50]: (i) both are in basal plane (graphene plane); (ii) Burgers vector is perpendicular to the basal plane and dislocation line is in the basal plane; (iii) Burgers vector and dislocation line are in non-basal direction; (iv) Burgers vector is in the basal plane, dislocation line is parallel to hexagonal axis.

From the possible dislocations summarized above, case (i) is the most relevant at the nanoscale as it corresponds to the dislocations in graphene. In this recently discovered two-dimensional nanomaterial represented by honeycomb lattice of carbon atoms, only edge dislocations are possible. More specifically, edge dislocation is formed by inserting a semi-infinite strip of atoms into the perfect crystalline lattice. The core of an edge dislocation in flat graphene is comprised of pentagon-heptagon pair defect, denoted by 5|7 symbol, as demonstrated in Fig. 2.7(c). Pentagon (heptagon), five (seven) membered ring, introduces positive (negative) disclination in flat graphene. Hence, dislocation in such structure can be viewed as a pair of positive and negative disclinations with net zero effect, where the distance between these disclinations defines the Burgers vector [5]. The onset of a dislocation dipole composed of two 5|7 cores via a 90° bond flip, known in chemistry as Stone-Wales isomerization [51], marks the yield point of a carbon (C) single-walled nanotube (SWNT) in tension. Further, the ductile behavior of carbon nanotubes, structures formed by the rolling of a graphene sheet into a tube, has also been attributed to the dislocation motion, the glide of a 5|7 edge dislocation core by further 90° bond flips, causing reduction in diameter and overall elongation of the tube [52, 53].

Recently, Ding et al. proposed the dislocation theory of chirality-controlled growth for C SWNTs by imposing to view any chiral tube (nanotubes are known to vary by the angle, called chiral angle, at which they are twisted) as a dislocated zigzag tube [6]. In other words, any chiral tube can be represented as a basis zigzag tube with the center-hollow screw dislocation, as demonstrated in Fig. 2.8. The choice of zigzag rather than armchair tube as a basis one was based on the computed barriers for re-initiation after atomic ring is complete. Zigzag tube appears to be more inert, while armchair tube can grow ring-by-ring almost unobstructed by the re-initialization, which means that armchair tube is a dislocated structure with respect to zigzag configuration. According to crystal growth theory [48], the growth rate is proportional to the magnitude of Burgers vector, which leads to overall dominance of nearly-armchair material. Their predictions can not be verified because of the lack of corresponding data. Nevertheless, connecting

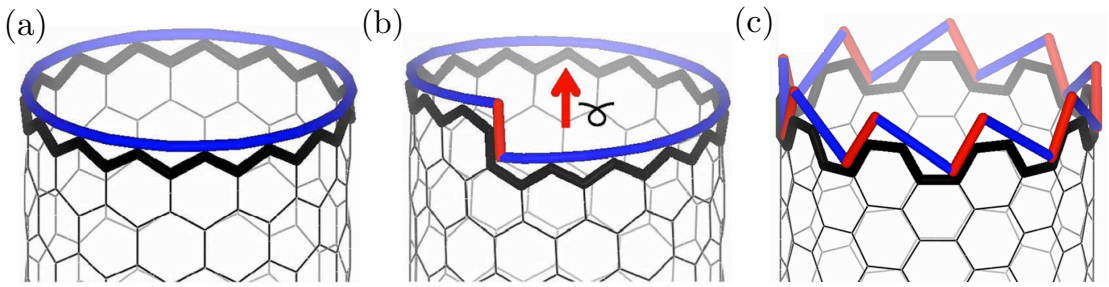

Figure 2.8: An axial screw dislocation in the C SWNT. (a) An achiral zigzag $(n, 0)$ tube, viewed as a perfect crystal, can be transformed into (b) a chiral tube $(n, 1)$ by cutting and shifting with Burgers vector shown in red. (c) In a similar manner an achiral armchair (m, m) tube can be also formally viewed as a dislocated zigzag (short blue zigzag segments) with m times larger Burgers vector than for $(n, 1)$ tube. This figure was taken from [6].

lengths of the grown C SWNTs and their chirality angles, Ding et al. found quantitative correlation of their theory predictions with the various known experiments.

In an attempt to verify the validity of "screw-dislocation-like" growth mechanism of C SWNTs proposed by Ding et al. [6], the experimental work was performed by Marchand et al. [54]. Field emission microscopy allowed them to observe the axial rotation of an individual C SWNT during the growth from nickel nanoparticle. Relying on the frame-by-frame analysis of the experimental video, which shows the axial rotation of the tube by discrete steps, they conclude that the screw dislocation growth of a C SWNT was directly observed with one carbon dimer at a time.

Chapter 3

Atomistic simulation methods

Since nanoscale structures comparable with the core of the dislocations, atomistic methods are best suited to model them. Two different computational techniques will be used in this work, namely *empirical* and *semi-empirical* molecular dynamics (MD) methods. Originally developed in the context of quantum chemistry and condensed matter physics and now used in various engineering contexts, these powerful methods combine fundamental quantum-mechanical predictive power with atomic resolution in length and time. Continuum mechanics models will be also constructed based on the atomistic simulation data. The goal is to provide a simplified understanding and to scale-up our results to dimensions that cannot be computationally afforded with microscopic methods.

MD simulations is a popular method for studying the mechanical properties of the nanostructures at the most fundamental atomic level [55, 56, 57, 53, 58]. MD is a computer simulation technique, where the classical equations of motion, describing a set of interacting atoms, are numerically solved in order to determine the trajectories of atoms [59, 60, 61]. The interatomic interactions are typically calculated either from full quantum-mechanical energy methods or from simplified mathematical expressions for potential energy, that attempt to incorporate the quantum mechanical interactions of electrons and nuclei in some simple analytical form, the latter is also called classical MD method. MD simulations can provide detailed information about the deterministic evolution of the molecular system during a given process, as well as its equilibrium configuration found at zero temperature. The latter type of MD simulations corresponds to the energy minimization mode (sometimes called molecular mechanics), where atoms

are displaced according to the net forces acting on them until these forces become negligibly small.

The interatomic potentials used in MD can be determined by several different approaches [62]. The most accurate methods are so-called *ab initio* or first-principles methods. These approaches explicitly account quantum-mechanical effects and, as a result, are computationally intensive and even prohibitive for big systems. Because of the limitation on the number of simulated atoms, their usage in the study of mechanical behavior is also limited. However, *semi-empirical* and *empirical* methods contain parameters that are found from fitting to experimental data or the results of first-principles calculations. Generally these techniques can correctly describe qualitative trends and they are usually the most appropriate methods available for modeling relatively large systems. For example, tight-binding (TB) is a basic *semi-empirical* method, which offers a satisfying description of the electronic structure and bonding of covalent systems in an intuitive localized picture and, therefore, it is useful for the large number of situations in which quantum-mechanical effects are significant, but the system size makes first-principles calculations impractical. *Empirical* methods based on classical interatomic potentials have been widely used in studies of the mechanical behavior of relatively large systems because of less computational requirements.

The interatomic potentials are crucially influencing the outcomes of MD simulations. This Chapter provides a review of two atomistic simulation techniques used in this work: classical MD with the reactive empirical bond-order (REBO) potential, and MD based on density-functional tight-binding (DFTB) models under periodic and objective boundary conditions (OBC). The recent technical implementations made in our DFTB code for modeling atoms containing d-orbitals are also discussed. In addition, illustrative examples of calculations with both methods are included.

3.1 Classical molecular dynamics: REBO potential

Classical or *empirical* potentials, which enter *classical* MD methods, are simplified analytical expressions that are intended to model the true interatomic forces originated from the quantum mechanical interactions of electrons and nuclei. There are several different types of *empirical* methods used for calculating interatomic potentials such as

the embedded atom method (EAM) [63], the Stillinger-Weber potential [64], the REBO potential [65], etc., that were designed to model particular materials. In our case, we focus only on the REBO potential, which is the most appropriate among the others for studying the mechanical properties of relatively large carbon nanostructures.

The empirical bond-order potential was initially developed and parameterized by Tersoff to model tetrahedrally-bonded materials such as carbon and silicon [66, 67]. It was based on the analytic bond-order potential energy formalism originally introduced by Abell [68]. While the energetics and behavior of the carbon-carbon bonds with defined character, namely, single, double, and triple bonds, were properly described by Tersoff potential for hydrocarbons, the intermediate bonding situations were not covered. In order to correct this deficiency and the non-physical overbinding of radicals, an improved form of Tersoff-type potential was developed by Brenner et al. [69]. However, this first generation REBO potential for hydrocarbons was not able to model processes involving energetic atomic collisions because of the Morse-type functions chosen to represent the pair interactions that lead to finite values for interaction energy as distance between atoms decreases [69]. Afterwards, Brenner et al. [65] developed so-called second generation REBO potential, where the different form for pair interactions was used to overcome the mentioned above problem, as well as the fitting database was expanded to improve the outcome. As a result, the second generation REBO potential, that realistically describes the behavior of carbon nanostructure systems and predicts reasonable physical properties [70, 71, 72], was built.

The chemical binding energy E_b of a set of atoms is calculated by summing over the interactions between atoms described by the short-ranged REBO potential as follows

$$E_b = \sum_i \sum_{j>i} [V_R(r_{ij}) - \overline{b}_{ij} V_A(r_{ij})], \tag{3.1}$$

where $V_R(r_{ij})$ and $V_A(r_{ij})$ are repulsive and attractive pairwise potentials that depend only on the distance r_{ij} between the two atoms i and j. In the second generation REBO potential these terms are given as

$$\begin{aligned} V_R(r_{ij}) &= f_c(r_{ij}) \left[1 + Q/r_{ij}\right] A \cdot e^{-\alpha r_{ij}}, \\ V_A(r_{ij}) &= f_c(r_{ij}) \sum_{n=1}^{3} B_n \cdot e^{-\beta_n r_{ij}}, \end{aligned} \tag{3.2}$$

where A, B, Q, α, and β_n are parameters determined by interacting atom types. The function $f_c(r_{ij})$ is a cutoff function that is used to limit the range of the covalent interactions, and hence, to guarantee that the potential is short-ranged and only nearest neighbors interactions are included. The so-called bond-order term $\overline{b}_{ij}$ between atoms i and j in equation (3.1) is responsible for the many-body interactions.This term depends on the local atomic environment, and hence, it is able to describe various chemical effects such as coordination numbers, bond angles, torsion angles, and conjugation effects. It can be expressed as

$$\overline{b}_{ij} = \frac{b_{ij}^{\sigma\pi} + b_{ji}^{\sigma\pi}}{2} + b_{ij}^{\pi}, \tag{3.3}$$

where $b_{ij}^{\sigma\pi}$ and $b_{ji}^{\sigma\pi}$ functions depend on the local coordination and bond angles for atoms i and j . The term b_{ij}^{π} is composed of two terms,

$$b_{ij}^{\pi} = \Pi_{ij}^{RC} + \Pi_{ij}^{DH}, \tag{3.4}$$

where Π_{ij}^{RC} term characterizes conjugated bonds and radical character between atoms i and j , and Π_{ij}^{DH} term is a function of the dihedral angle for carbon-carbon bonds, that accounts for torsion effects in molecules. Therefore, this bond-order term in REBO potential allows to model chemical reactions and complicated processes, where the bonding between carbon atoms changes, as well as bond formation or breakage occur.

Above the short-range interactions well-described with REBO potential, the long-range van der Waals interactions also should be accounted. The van der Waals bonding is defined as a bonding type based on different kinds of dipole interactions. London dispersion interactions or van der Waals interactions between instantaneous induced dipoles dominate in non-polar molecules and usually approximated with the pairwise Lennard-Jones potential [73], which has the following functional form

$$V_{LJ}(r_{ij}) = 4\varepsilon_{ij}\left[\left(\frac{\sigma_{ij}}{r_{ij}}\right)^{12} - \left(\frac{\sigma_{ij}}{r_{ij}}\right)^{6}\right], \tag{3.5}$$

where ε_{ij} and σ_{ij} are the Lennard-Jones parameters determined by the types of modeled atoms i and j.

Consequently, classical MD simulation code based on the interatomic potential composed of the short-range second generation REBO potential, that captures covalent interactions, and the Lennard-Jones potential, which describes the the long-range van der Waals interactions, was chosen in this work to study carbon nanostructures.

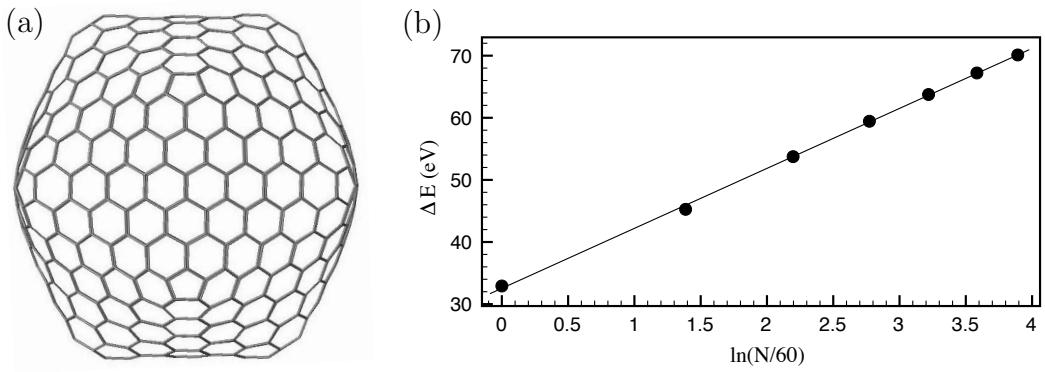

Figure 3.1: (a) Atomistic representation of icosahedral fullerene C_{540}. (b) The excess energies of icosahedral fullerenes calculated with energy minimization based on REBO potential via conjugate gradient relaxation (filled circles) and the prediction of equation (3.6) (solid line).

3.1.1 Illustrative example: energetics of icosahedral fullerenes

To demonstrate the suitability of the REBO potential, we study here the energetics of icosahedral fullerenes, molecules composed entirely of carbon atoms. These structures are of interest for this work since carbon nano-onions are composed of special sequence of icosahedral fullerene molecules. This nanostructure can be represented by the deformed graphene layer, which under the continuum elastic approximation can be considered as a thin plate and, thus, the formation energy of this structures relative to the graphene layer is the strain energy needed to deform a flat plate into desired shape. Based on the Cauchy-Born rule [74], the strain energy density at the continuum level is the energy stored in atomic bonds. By equating the excess energy of carbon nanostructure from atomistic calculations to strain energy due to deformation, we can compute important mechanical characteristics of graphene such as the bending rigidity. This type of analysis was performed long time ago by Tersoff [75], as well as there are more recent works where REBO potential is used to calculate the energies of fullerenes [71].

Idealized carbon nano-onion, represented by a set of concentric icosahedral fullerenes of different sizes, is composed of the following fullerene sequence $C_{60}@...@C_{60n^2}$, where n is a shell number. This configuration is recognized as the most favorable and stable one for carbon nano-onions [13]. An example of an icosahedron fullerene C_{540} is given

in Fig. 3.1(a). Icosahedral fullerene contains 12 pentagonal disclinations of 60° situated at vertices of an icosahedron. Therefore, the excess energy relative to the piece of infinite graphene associated with fullerene shape comes from both bending of the layer and the energy needed to create disclinations. Since the shape of minimum energy for pentagonal disclination is a truncated cone, an icosahedron can be approximated by the union of 12 truncated cones. In this case the expression for the total excess of energy for a single icosahedral fullerene containing $N = 60n^2$ atoms relatively to infinite graphene sheet is

$$\Delta E_{C_N} = E_{C_{60}} + \frac{11\pi}{5} D \ln (N/60), \tag{3.6}$$

where D is a bending rigidity, $E_{C_{60}}$ is the total excess energy of C_{60} (the used potential predicts $E_{C_{60}} = 32.92$ eV) which includes the core energy of disclinations [75, 71]. Figure 3.1(b) shows the results of minimization of the total energy of icosahedral fullerenes by using the second generation REBO potential [65] together with the prediction of eq. (3.6), where the fitting procedure gives $D = 1.4$ eV. The result for bending rigidity of graphene, obtained from the described above methodology based of atomistic calculation with REBO potential, is in good agreement with the value 1.5 eV found from the more accurate *ab initio* methods [76].

3.2 Density-functional tight-binding molecular dynamics

Standard TB implementations are designed for modeling an infinite bulk crystalline system. In this formulation, only atoms located in the repeated unit cell, which obeys solely the translation repetition rules, are simulated. As a result, the infinite-size problem is reduced to a finite number of atoms that usually within the computational reach for TB methods. For instance, the minimal unit cell with only two atoms is needed to calculate the bulk properties of graphene monolayer.

Unfortunately, taking advantage of translational symmetry for nano-objects containing screw dislocations does not bring a significant simplification in terms of the number of atoms. For this reason, atomistic calculations based on standard codes, where only translational symmetry is considered, are computationally prohibitive. However, if one can exploit the helical symmetry composed of translation and rotation operations the

smaller repeating cells can be selected. In this case, the simulation size can be drastically reduced for systems that have helical symmetry such as screw-dislocated structures. Therefore, the symmetry-adapted DFTB MD, which explicitly accounts for helical symmetry, is used in this work to study nano-objects with screw dislocations. In the next sections the density functional theory-based TB model together with its translational and symmetry-adapted formulations is described.

3.2.1 Formulation of tight-binding MD method

In standard TB method formulated for a periodic structure the electronic states are obtained by solving the one-electron Schrödinger equation that writes as

$$\left[-\frac{\hbar^2}{2m}\bigtriangledown^2 + V(\mathbf{r})\right]|j\rangle = \epsilon_j|j\rangle, \tag{3.7}$$

where m is the mass of electron, $\hbar$ is the Plank's constant, $V(\mathbf{r})$ is the periodic potential, $|j\rangle$ and ϵ_j are the one-electron wavefunction and energy for the state j, respectively. The main assumption of the method is that a set of atomic-like orbitals is sufficient to describe the wave function solution for the one-electron problem. As a result, the solution of this equation for the single electron states is represented by a linear combination of atomic orbitals located on each atomic site. The localized atomic orbitals of s, p, and d types are illustrated in Fig. 3.2. The number of considered orbitals n_α is specific to the treated chemical elements and it usually equals the number of valence electrons. For instance, carbon has $n_\alpha = 4$, while zinc (Zn) has $n_\alpha = 12$. Then the one-electron eigenfunctions $|j\rangle$ composed of the localized orbitals denoted by $|\alpha n\rangle$, where α labels the orbital symmetry (e.g. for carbon s, p_x, p_y, and p_z orbitals) and n corresponds to the atomic location, can be written as

$$|j\rangle = \sum_{\alpha,n} C_{\alpha n}(j)|\alpha n\rangle, \qquad j = 1, ..., N. \tag{3.8}$$

Here N is the number of eigenstates that equals the total number of valence electrons in the simulated structure, $C_{\alpha n}(j)$ are the coefficients. If translation symmetry is not accounted $N = n_\alpha N_0 N_t$, where N_t is a large number of translation cells, N_0 is the number of atoms in this unit cell. Next, substituting eq. (3.8) into (3.7) and integration between basis functions $|\alpha n\rangle$ the following generalized $N \times N$ eigenvalue problem needs

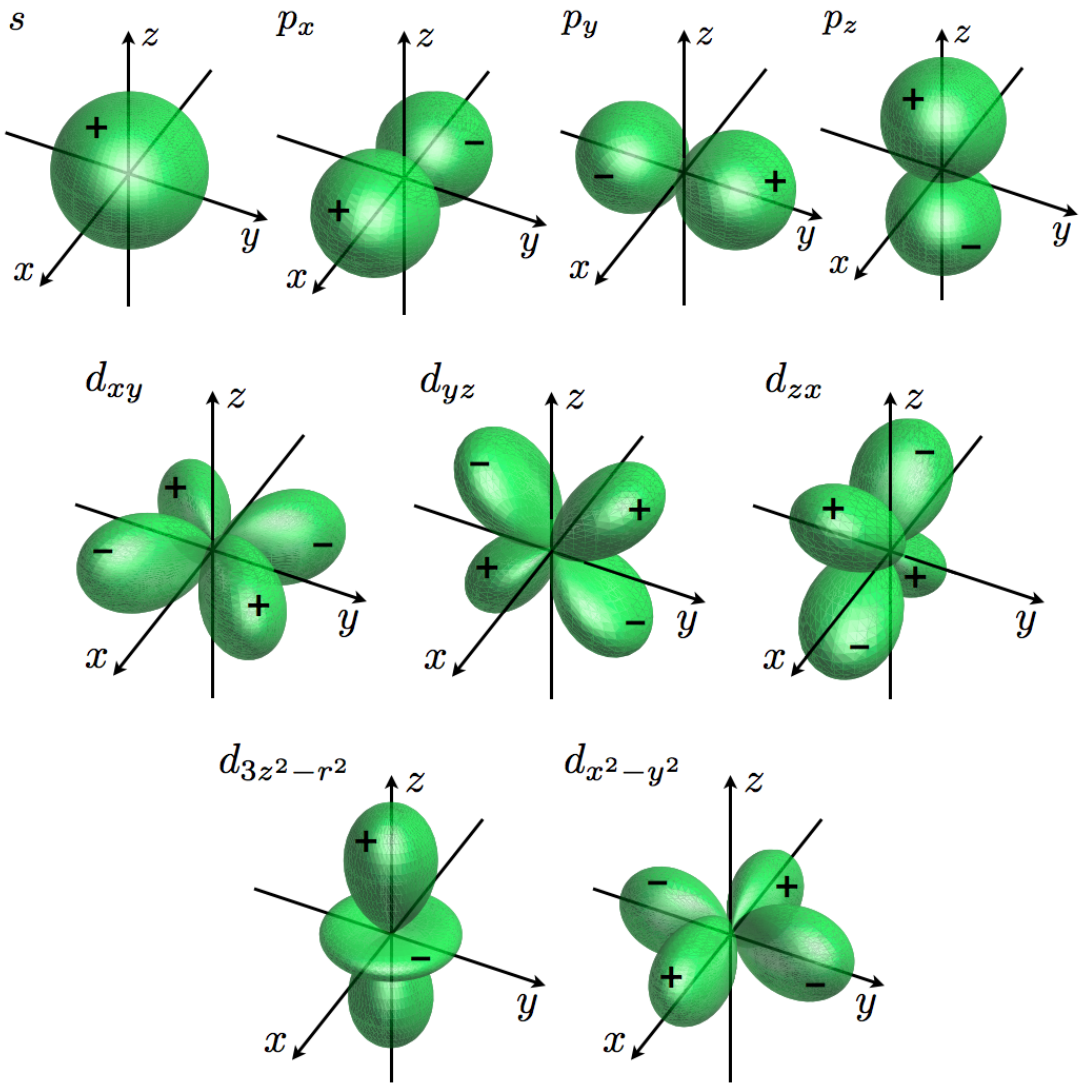

Figure 3.2: A schematics of the localized atomic orbitals s, p_x, p_y, p_z, d_{xy}, d_{yz}, d_{zx}, $d_{3z^2-r^2}$ and $d_{x^2-y^2}$. The plus sign corresponds to the positive wavefunction amplitude, while the minus indicates the negative wavefunction amplitude.

to be solved in order to obtain the vector of coefficients $\mathbf{C}(j)$ and the energy eigenvalues

$$\mathbf{H} \cdot \mathbf{C}(j) = \epsilon_j \mathbf{S} \cdot \mathbf{C}(j), \qquad j = 1, ..., N, \tag{3.9}$$

where $\mathbf{H}$ and $\mathbf{S}$ correspond to Hamiltonian and overlap matrices, respectively. For simplicity in *semi-empirical* TB method the Hamiltonian matrix elements are not explicitly calculated, instead they are replaced with some functions that depend only on the interatomic distances and symmetry of interacting orbitals. And then these functions are parametrized by the data from more accurate first-principles calculations [77, 78] calculations or experimental results [79]. Next, using this one-electron solution and filling the energy levels according to the Fermi-Dirac distribution, function f, the following expression for the total electronic energy, that depends parametrically on the coordinates of the nuclei, can be written as

$$E_{band} = 2 \sum_{j=1}^{N} f_j \epsilon_j, \tag{3.10}$$

where the factor of 2 reflects the fact that electron has two possible values of spin. Employing the Born-Oppenheimer approximation [80], which separates the electronic and nuclear degrees of freedom, the found electronic energy can be directly used to give the motion of the nuclei, that are treated classically. Finally, the forces acting on the atoms, that are needed to perform molecular dynamics, can be calculated for atom i as $\mathbf{F}_i = -\partial E_{band}/\partial \mathbf{X}_i$, where $\mathbf{X}_i$ represents its coordinate.

Two-centre Harrison's orthogonal TB model

Before presenting the more complex model, let us review first the simple orthogonal (i.e. the overlap matrix is simply an identity matrix $\mathbf{S} = \mathbf{I}$) TB model proposed by Harrison [81]. This model assumes that the hopping or off-diagomal Hamiltonian matrix element $t_{\alpha n, \alpha' n'}$ between atomic orbitals α and α' at sites n and n' has a power law dependance on the internuclear distance d_0.

The hopping Hamiltonian matrix elements presented in this convenient approximation are given in [81]. As an example, some of these matrix elements are given below

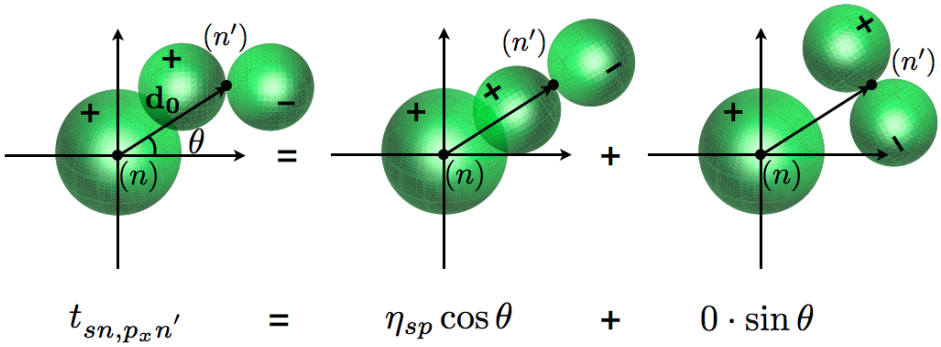

Figure 3.3: Schematic representation of the off-diagonal matrix element $t_{sn,p_x n'}$ evaluation. Here p orbital is decomposed into parallel and perpendicular components with respect to the joining vector $\mathbf{d_0}$ between the sites n and n' in order to calculate the σ and π interactions.

$$
\begin{aligned}
t_{sn,sn'} &= \eta_{ss}\frac{\hbar^2}{m_e}\frac{1}{d_0^2}, \\
t_{sn,p_\mu n'} &= l_\mu \eta_{sp}\frac{\hbar^2}{m_e}\frac{1}{d_0^2}, \\
t_{p_\mu n,p_\upsilon n'} &= [l_\upsilon l_\eta(\eta_{pp}-\eta_{pp}^{'})+\delta_{\upsilon\eta}\eta_{pp}^{'}]\frac{\hbar^2}{m_e}\frac{1}{d_0^2}, \\
t_{sn,d_{\mu\upsilon}n'} &= \sqrt{3}l_\mu l_\upsilon \eta_{sd}\frac{\hbar^2}{m_e}\frac{r_d^{3/2}}{d_0^{7/2}},
\end{aligned}
\tag{3.11}
$$

Here μ, υ and ι denote the cartesian indexes, namely, x, y or z. l_υ, l_μ and l_ι are the direction cosines between n and n' sites located on different nuclei and separated by distance d_0. r_d is a parameter specific for an element containing the d orbitals which can be found in the Solid State Table [81]. The η parameters characterize the amount of overlap between orbitals of defined symmetries, and hence, they are responsible for the strength of the chemical bonds. Unprimed and primed η coefficients are related with the σ and π bonds, respectively. The values for η parameters are fitted to correctly reproduce the electronic properties of simulated structure such as the band gap. To illustrate how the hopping matrix element are evaluated, Fig. 3.3 shows the interactions between s and p orbitals. Since s and p have odd and even parity, π interactions vanish and only σ interactions between overlapping orbitals remain.

Two-centre density-functional-based nonorthogonal TB model

Density functional theory (DFT) is a first-principle method widely used nowadays to study the behavior of many-electron systems [82, 83]. The main idea of the method is to express the properties of a system, such as ground energy, as functionals of the electron density function $n(\mathbf{r})$, that depends on position $\mathbf{r}$, and then use the variational principle to find it. The so-called Kohn-Sham equation, which is the one-electron Schrödinger equation of a fictitious system of non-interacting electrons, where effects of electron-electron interactions are incorporated in the effective potential, needs to be solved. However, this method is time consuming and becomes even prohibitive for relatively large systems. That is why the simplified *semi-empirical* DFTB method was developed.

Performing the first-principles simulations with an atomic-like basis set to calculate the band structure, and then fitting these data to get the best suited Hamiltonian matrix elements, Porezag et al. [78] constructed the DFTB model. In this model the well-established Slater-type orbitals [84] are used to form an atomic basis, as

$$|\alpha\rangle = \sum_{n,\xi,l_\alpha,m_\alpha} a_{n\xi} r^{l_\alpha+n} e^{-\xi r} Y_{l_\alpha m_\alpha}\left(\frac{\mathbf{r}}{r}\right), \tag{3.12}$$

where $Y_{l_\alpha m_\alpha}$ are the spherical harmonics, $a_{n\xi}$ is a normalizing constant. Here they construct the interatomic potential in three steps by: (1) solving the modified Kohn-Sham equation; (2) calculating all Hamiltonian and overlap matrix elements; and (3) fitting the short-range repulsive potential V_{rep}. In the first step the solution of the modified Kohn-Sham equation gives the wavefunctions and energy eigenvalues for the one-electron problem. The used Kohn-Sham potential, which is constructed to account for the electron-electron interactions, writes as

$$V^{psat}(\mathbf{r}) = V_{nucleus}(\mathbf{r}) + V_{Hartree}[n(\mathbf{r})] + V_{xc}^{LDA}[n(\mathbf{r})] + \left(\frac{\mathbf{r}}{2r_{cov}}\right)^2, \tag{3.13}$$

where $V_{nucleus}$ represents the ionic potential, $V_{Hartree}$ potential captures the electron-electron Coulomb repulsion, and V_{xc}^{LDA} is an exchange-correlation potential in local-density approximation, r_{cov} is a covalent radius of the element. Then, the Hamiltonian and overlap matrix elements are calculated using the potential (3.13), but without the last term. Next, the data are fitted by equating the short-range repulsive potential with a difference between *ab initio* value and computed electronic band energy for various

Table 3.1: Comparison of the optimized lattice parameters of wurtzite ZnO bulk structure (see Fig. 3.4(a)) obtained with DFTB model, DFT calculations and experiment.

parameter:	DFTB (present)	DFTB [87]	DFT [87]	Experiment [88]
a, ($\mathring{A}$)	3.252	3.202	3.193	3.254
c, ($\mathring{A}$)	5.283	5.271	5.187	5.212
u	0.376	0.388	0.376	0.382

interatomic distances. In this way the DFTB parameterization is usually performed for diatomic molecules. Filnally, the total DFTB energy is determined as a sum of band structure and pair-repulsion terms:

$$E_{tot} = E_{band} + E_{rep} = 2\sum_{i} f_i \epsilon_i + \sum_{n} \sum_{n'>n} V_{rep}(|\mathbf{X}_{n'} - \mathbf{X}_n|), \tag{3.14}$$

where the term E_{rep} includes the ion-ion repulsion and the electron-electron interaction.

Developed to model the behavior of crystalline structures including the electronic properties, the DFTB is a powerful method that has been successfully applied to various problems with different materials such as carbon [78], silicon [85], boron [86], and zinc oxide [87]. As an example, Table 3.1 shows the optimized lattice parameters of wurtzite ZnO bulk structure, illustrated in Fig. 3.4(a), obtained with different approaches, including the most theoretically accurate and reliable DFT model, the DFTB methods used in this and other works, as well as experiments. A good agreement between all these data confirms the validity of the described above DFTB methodology.

Being rather accurate and having the high transferability and the variety of available parameterizations, the DFTB approach became quite popular in modeling of crystalline structures. Consequently, the DFTB model has been selected to study the mechanical and electronic properties of nanostructures in the present study.

3.2.2 Tight-binding MD under periodic boundary condition

Obviously, a bulk crystalline materials with N on the order of 10^{23} can not be modeled directly. The translation symmetry, that determines the crystal structures, allows to reduce the number of simulated atom, and hence, make the calculations computationally

accessible. For simplicity, the approach for the one-dimensional periodic structure is introduced below.

The positions of atoms for the whole structure can be generated by shifting the atomic coordinated within the unit cell $\mathbf{X}_n$ (n runs from 1 to N_0) by the vector $\mathbf{T}$ (with magnitude $|\mathbf{T}| = T$) that describes the lattice periodicity as

$$\mathbf{X}_{n,\zeta} = \zeta\mathbf{T} + \mathbf{X}_n, \tag{3.15}$$

where ζ labels the translation replicas ranged from 0 to $N_t - 1$. In order to satisfy the periodic boundary condition (PBC), instead of eq. (3.8) the one-electron solutions should be represented in terms of the Bloch sums as follows

$$|\alpha n, k\rangle = \frac{1}{\sqrt{N_t}} \sum_{\zeta=0}^{N_t-1} e^{ikT\zeta} |\alpha n, \zeta\rangle, \tag{3.16}$$

where $k \in [-\pi/T, \pi/T)$ is the wavevector (scalar for the considered one-dimensional problem) that takes N_t uniformly spaced values with a step $\delta k = 2\pi/TN_t$, and $|\alpha n, \zeta\rangle$ denotes the orbital α of atom n located in the translational cell ζ. Because of the fact that the overlap matrix elements between Bloch sums solutions with different k values are zeros, the eigenvalue problem becomes block-diagonal and can be solved separately for each N_t block labeled by k:

$$\mathbf{H}(k) \cdot \mathbf{C}(j,k) = \epsilon_j(k)\mathbf{S}(k) \cdot \mathbf{C}(j,k), \quad j = 1, ..., N/N_t. \tag{3.17}$$

Consequently, $N \times N$ eigenvalue problem (3.9) can be splitted into N_t eigenvalue problems (3.17) of size $N/N_t \times N/N_t$ to calculate the same N electronic states, which is much more computationally efficient. Lastly, the total energy of the electronic states in the translation formulation is computed in the following manner

$$E_{band} = 2 \sum_{j=1}^{N/N_t} \sum_{k=-\pi/T}^{\pi/T-\delta k} f_j(k)\epsilon_j(k), \tag{3.18}$$

and then it is used as an interatomic potential to run MD simulations.

3.2.3 Tight-binding MD under objective boundary conditions

The detailed description of objective MD methodology is given in [89]. Briefly, the symmetry-adapted formulation is aimed to simulate the objective atomic structures [90],

in which every atom has the same atomic environment up to rotation and translation. In other words, it characterizes the structure that obeys helical and angular symmetries:

$$\mathbf{X}_{n,(\zeta_1,\zeta_2)} = \mathbf{R}_2^{\zeta_2}\,\mathbf{R}_1^{\zeta_1}\mathbf{X}_n + \zeta_1\mathbf{T}_1, \tag{3.19}$$

where n runs over the N_0 atoms located inside the objective domain, indexes ζ_1 and ζ_2 label various replicas of the domain. The helical operation applied to the objective domain is defined by the rotational matrix $\mathbf{R}_1$ of angle θ_1 and the axial vector $\mathbf{T}_1$, while the angular symmetry is described by the rotational matrix $\mathbf{R}_2$ of angle θ_2.

The next step is to find the one-electronic solution. However, the Bloch theorem used for PBC structures should be adapted in order to properly treat these new boundary conditions. For N_s number of helical operations and N_a number of angular rotations, the symmetry-adapted Bloch sums are written as

$$|\alpha n, l\kappa\rangle = \frac{1}{\sqrt{N_a \cdot N_s}} \sum_{\zeta_1=0}^{N_s-1} \sum_{\zeta_2=0}^{N_a-1} e^{il\theta_2\zeta_2 + i\kappa\zeta_1} |\alpha n, \zeta_1\zeta_2\rangle, \tag{3.20}$$

where $l = 0, 1, ..., (N_a - 1)$ represents the angular number, $\kappa \in [-\pi, \pi)$ is a helical wavevector introduced to avoid the usage of helical distances. Also $|\alpha n, \zeta_1\zeta_2\rangle$ refers to the orbital with symmetry α located on atom n in the domain indexed by ζ_1 and ζ_2, which is obtained by applying a $\mathbf{R}^{(\zeta_1,\zeta_2)}$ rotation matrix with angle $\Theta = \zeta_1\theta_1 + \zeta_2\theta_2$ to the initial $(0, 0)$ cell. Specifically, for *sp* system case it reads as

$$\begin{pmatrix} |sn, \zeta_1\zeta_2\rangle \\ |p_x n, \zeta_1\zeta_2\rangle \\ |p_y n, \zeta_1\zeta_2\rangle \\ |p_z n, \zeta_1\zeta_2\rangle \end{pmatrix} = \begin{pmatrix} 1 & 0 & 0 & 0 \\ 0 & \cos\Theta & -\sin\Theta & 0 \\ 0 & \sin\Theta & \cos\Theta & 0 \\ 0 & 0 & 0 & 1 \end{pmatrix} \cdot \begin{pmatrix} |sn\rangle \\ |p_x n\rangle \\ |p_y n\rangle \\ |p_z n\rangle \end{pmatrix}, \tag{3.21}$$

Note that some orbitals are invariant to this transformation, namely, *s* orbital is not affected because of its symmetry, while the p_z is oriented along the rotation axis. For modeling carbon systems, the set of *sp* valence orbitals suffices. However, we are also interested in studying the structures containing elements with the *d* level filled such as Zn. The *d* orbitals have two units of angular momentum, and therefore, there are five independent orbitals, d_{xy}, d_{yz}, d_{zx}, $d_{x^2-y^2}$, and $d_{3z^2-r^2}$ shown in Fig. 3.2, that are equal in energy but have different symmetry properties. For the *sd* case needed to describe

materials containing Zn atoms the matrix is

$$\begin{pmatrix} |sn,\zeta_1\zeta_2\rangle \\ |d_{x^2-y^2}n,\zeta_1\zeta_2\rangle \\ |d_{xy}n,\zeta_1\zeta_2\rangle \\ |d_{zx}n,\zeta_1\zeta_2\rangle \\ |d_{yz}n,\zeta_1\zeta_2\rangle \\ |d_{3z^2-r^2}n,\zeta_1\zeta_2\rangle \end{pmatrix} = \begin{pmatrix} 1 & 0 & 0 & 0 & 0 & 0 \\ 0 & \cos 2\Theta & -\sin 2\Theta & 0 & 0 & 0 \\ 0 & \sin 2\Theta & \cos 2\Theta & 0 & 0 & 0 \\ 0 & 0 & 0 & \cos\Theta & -\sin\Theta & 0 \\ 0 & 0 & 0 & \sin\Theta & \cos\Theta & 0 \\ 0 & 0 & 0 & 0 & 0 & 1 \end{pmatrix} \cdot \begin{pmatrix} |sn\rangle \\ |d_{x^2-y^2}n\rangle \\ |d_{xy}n\rangle \\ |d_{zx}n\rangle \\ |d_{yz}n\rangle \\ |d_{3z^2-r^2}n\rangle \end{pmatrix}.$$

Here $d_{3z^2-r^2}$ orbital is also invariant because of the orientation along the rotation axis.

Analogously, the Hamiltonian and overlap matrix elements between the symmetry-adapted Bloch sums with different angular and helical numbers vanish. As a result, the block-diagonal eigenvalue problem is converted into N_sN_a problems of $n_\alpha N_0 \times n_\alpha N_0$ size, but now each block is labeled by l and κ:

$$\mathbf{H}(l\kappa)\cdot\mathbf{C}(j,l\kappa) = \epsilon_j(l\kappa)\mathbf{S}(l\kappa)\cdot\mathbf{C}(j,l\kappa), \qquad j = 1,...,n_\alpha N_0. \tag{3.22}$$

Next, the total electronic energy comprised in symmetry-adapted domains is found as

$$E_{band} = 2\sum_{j=1}^{n_\alpha N_0}\sum_{\kappa=-\pi}^{\pi-\delta\kappa}\sum_{l=0}^{N_a-1} f_j(l\kappa)\varepsilon_j(l\kappa), \tag{3.23}$$

where $\delta\kappa = 2\pi/N_s$. Finally, the computed electronic energy, that represents the interatomic potential, is used to calculated the forces acting on each atom, and hence, MD simulations can be performed under this symmetry-adapted mode.

Illustrative example: band structure of ZnO nanotube

In this paragraph we demonstrate the ability of our d-orbitals enhanced code to describe the electronic structure of ZnO nanotubes in both standard-translational and symmetry-adapted formulations that should give equivalent results for the electronic band structures. The analytical derivatives of the energy integrals under the two-center approximation for recently implemented d orbitals are shown in Appendix B. The simple case of (5, 5) armchair single-wall ZnO nanotube, shown in Fig. 3.4, is considered here. For the direct comparison between these two methods the particular simulation domain is chosen for the symmetry-adapted formulation, namely, it consists of 4 atoms and has

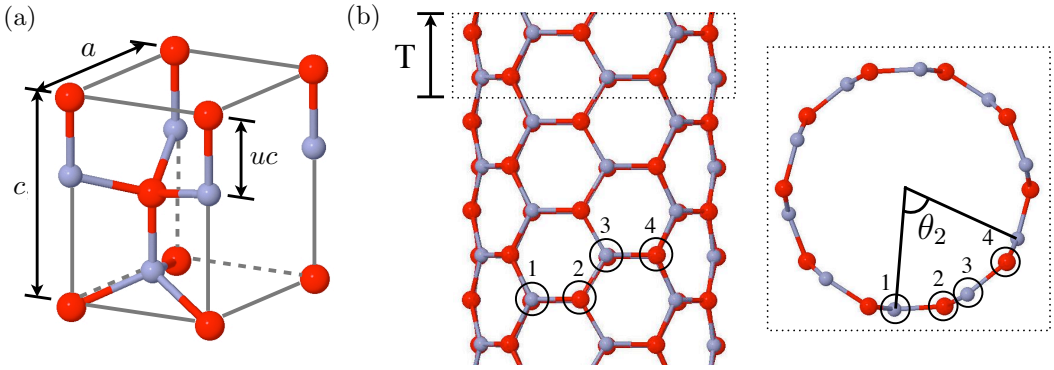

Figure 3.4: Atomistic representations of (a) the periodic unit cell of bulk ZnO material in wurtzite phase and (b) (5, 5) single-wall ZnO nanotube, where violet and red spheres denote zinc and oxygen atoms, respectively. In (b) the periodic unit cell is depicted by the dotted lines in both side (left) and axial (right) views, its translation vector **T** is also shown by an arrow, as well as four atoms forming the objective domain are labeled.

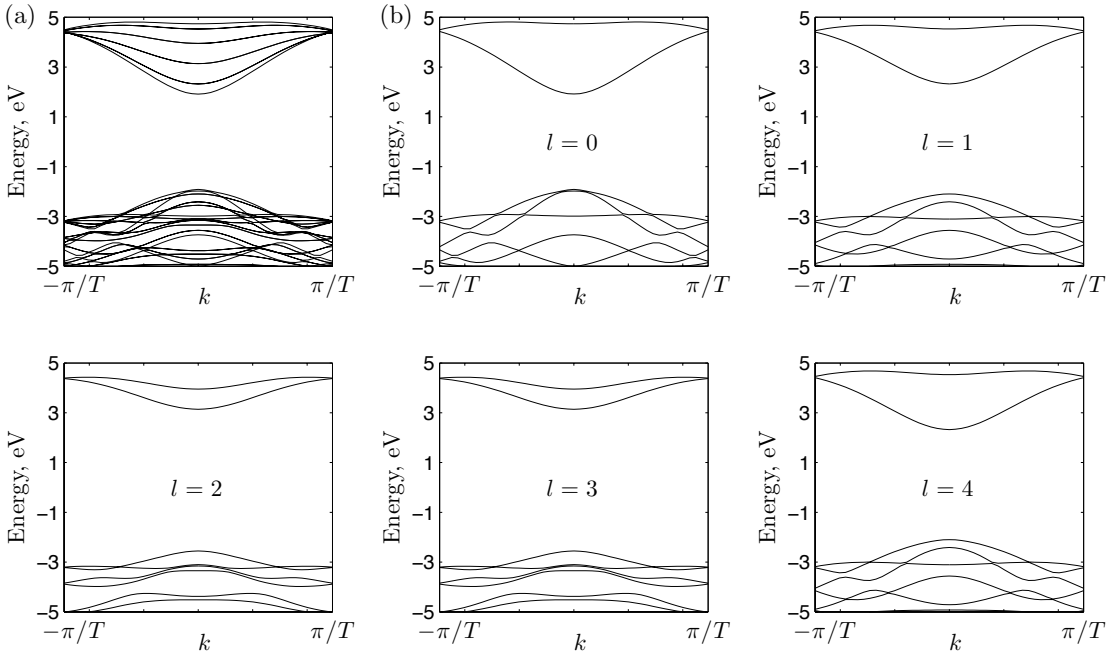

Figure 3.5: Electronic energy bands of a $(5, 5)$ armchair single-wall ZnO nanotube as obtained with (a) translation and (b) symmetry-adapted formulation. Here 45 k-points were used to perform the band structure calculation of a static relaxed configuration. The Fermi level located at the middle of the band gap is set to zero.

angular symmetry of angle $\theta_2 = 2\pi/5$ and helical symmetry with $\theta_1 = 0$, $T_1 = T$, where T is a translation period, meaning that helical operation becomes purely translation and helical wavevector coincides with the linear wavevector.

Figure 3.5 shows the numerically calculated electronic band structure of armchair ZnO nanotube under periodic (a) and objective (b) boundary conditions. In the case of PBC, the bands of the full translation cell containing 20 atom are computed by solving 180×180 eigenvalue problem. While under OBC the angular symmetry is accounted and the electronic bands with different angular numbers l are calculated. In other words, five 36×36 eigenvalue problems are solved instead. Note that due to symmetry, the $l = 1, 4$ and $l = 2, 3$ bands are degenerate. The equivalence between these two approaches is evident if plot all l bands given by symmetry-adapted method together and compare with the result obtained for the full translation cell. The perfect overlap between these results can be seen by inspecting the plots illustrated in Fig. 3.5.

Chapter 4

Dislocation processes in carbon nano-onions

Graphite has long served as a model material to understand dislocations. For instance, an early work on natural graphite provided factual evidence for the existence of screw dislocations [49]. Recently, synthetic carbon nanostructures began to be explored [91, 92] in order to understand dislocations at the nanoscale.

We are interested in studying the dislocation-driven processes in carbon nano-onions at high temperatures. The experimental part of this work was carried out in collaboration with Sandia National Laboratories, whose area of interests is focused on the *in situ* electron microscopy of nanostructured materials. By studying the experimental movies and high resolution images of heated nano-onions we identify, model and simulate processes driven by the presence of dislocations. Our goal is to model these processes at the atomistic and continuum levels in order to explain experimentally-observed behavior. This Chapter presents our study performed to understand the dislocation dynamics in carbon nano-onions which was published in [33].

4.1 Dislocations in carbon nano-onions

We study the well-known $\frac{1}{2}\langle 0001\rangle$ edge dislocation [50] in nested multishell carbon onions [10, 11], a complex system that was not considered before. The differences with respect to the planar case transpire from Figure 4.1, presenting the screw dipole

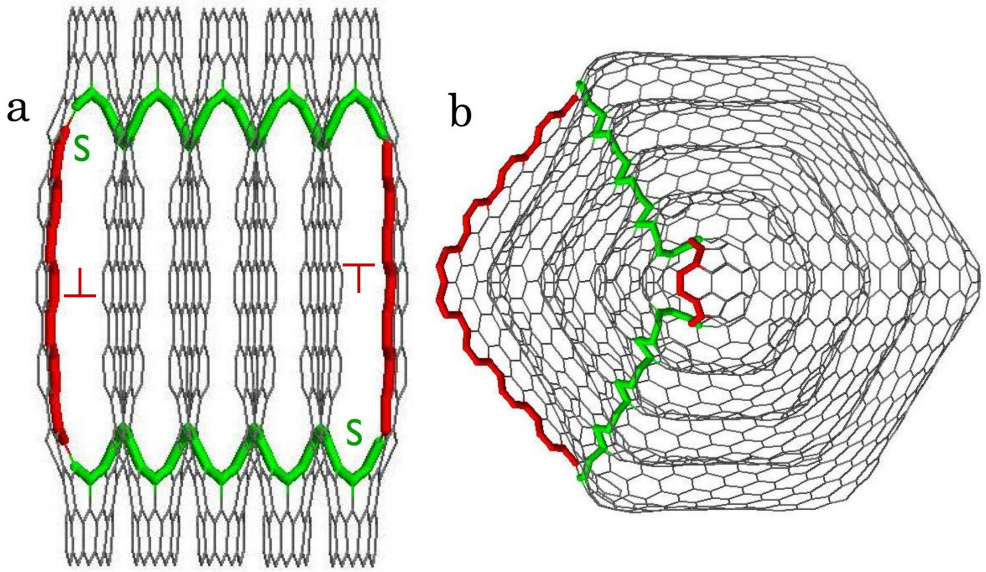

Figure 4.1: (a) A screw dipole in AA graphite corresponds to (b) a 3D spiroid [7] in a carbon nano-onion. The later structure was derived from of a C_{60}@...@C_{60n^2}@...@C_{1500} sequence of five icosahedral fullerenes. The length of the free-edge (red) is twice the length of the icosahedral edge. The inner (outer) edge contains four (sixteen) undercoordinated atoms.

of the AA graphite [93] accommodated in an icosahedral nano-onion. In the planar case, Figure 4.1(a), the dislocation loop contains two parallel screws (green), which link neighboring shells through deformed sp^2 bonds, and two unpaired (red) parallel armchair edges of the same size. In the spherical case, Figure 4.1(b), the screw components are directed radially. The two edges left unpaired (red) in the outermost and innermost shells not only have different curvatures but also show a significant disparity in length. All shells are cross-linked and an Archimedean spiral can be traced between the two edges.

The most important finding is that carbon onions exhibit dislocation dynamics very different from those of the crystalline bulk phase and even carbon nanotubes. The asymmetry introduced by the spherical topology reflects in an unexpected attraction of dislocations towards the core, as abundantly observed experimentally in dislocation dissociation and annihilation processes. Atomistic calculations carried out on idealized onions combined with rigorous energy analysis reveal a robust inward driving force on

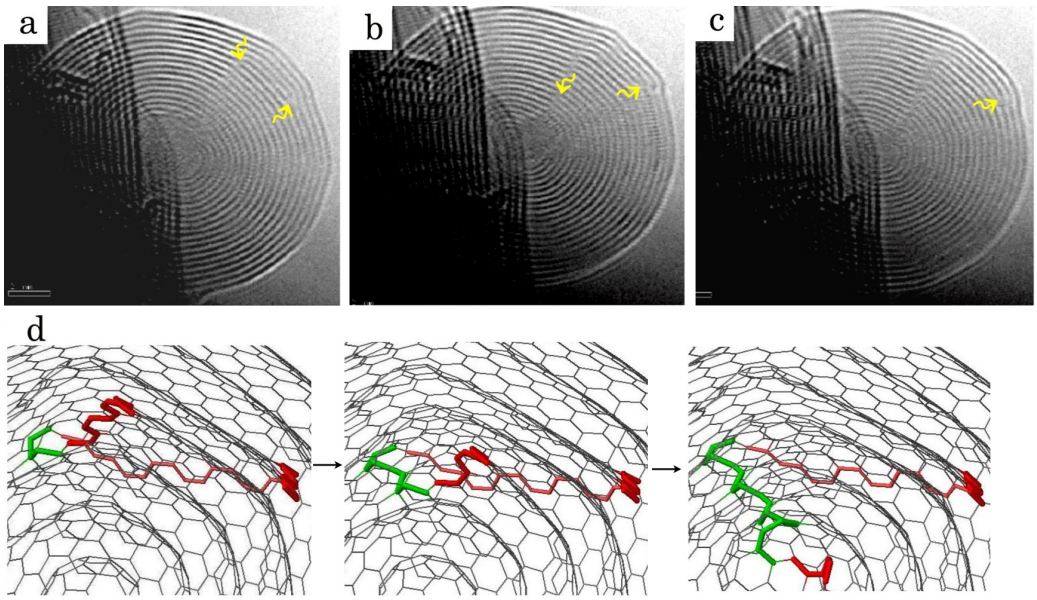

Figure 4.2: (a-c) *In situ* observation of dislocation dissociation in a nano-onion of $\sim$ 10 nm in radius. Arrows point out the dislocation edges. (d) An atomic structural model for the inwards glide of the lower edge with cross-linking of the shells. The atoms in red (green) belong to the edge (screw) component of the dislocation loop.

the outer $\frac{1}{2}\langle 0001\rangle$ edge associated with a reduction in the number of dangling bonds. This force, intrinsic to the spherical topology, is able to account for the experimental observations. The provided microscopic modeling is the first attempt to describe and rationalize dislocation processes in nano-onions.

4.2 Modeling of dislocation processes

The experiments with carbon nano-onions were conducted inside a high resolution transmission electron microscope attached to a Nanofactory scanning tunneling microscope. Carbon nano-onions coexist with nanotubes produced by arc-discharge, with the onions being attached to the surface of the tubes. The STM probe inside this platform was manipulated to contact individual nanotubes, but not nano-onions. A high current is passed through these nanostructures to Joule heat them to a temperature close to

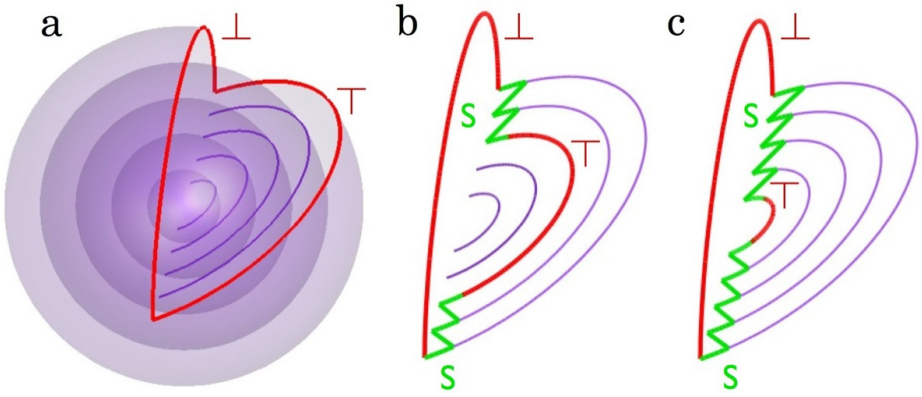

Figure 4.3: Proposed mechanism for the creation of a dislocation loop in a nano-onion exposed to high temperature and electron irradiation. (a) The outermost shell breaks, creating a void with two edges (thicker red lines). (b), (c) The right edge glides inwards, cross-linking the shells left behind. A dislocation loop composed of two edge and two screw components is formed. For clarity, only the dislocation loop and the gliding edge former or future position are shown.

2000^0C [94]. At such a high temperature and under electron radiation, preexisting dislocations in nano-onions become highly mobile, without the application of any mechanical forces.

Figure 4.2 illustrates the observed interactions of two nonradially aligned $\frac{1}{2}\langle 0001\rangle$ and $\frac{1}{2}\langle 000\bar{1}\rangle$ edges located three shells under the surface of a nearly spherical onion. Although immediately next to each other, due to the large azimuthal distance the two edges cannot recombine. Instead they dissociate in a sequential way, with the lower edge migrating radially inwards, crossing eight shells, Figure 4.2(b), and eventually vanishing into the core, Figure 4.2(c). Note that this intriguing inwards glide phenomenon was not observed in multiwalled carbon nanotubes [91, 92]. During the same time span the upper edge exhibits a contrasting slow mobility in the outward direction. As shown in Figure 4.2(c), this edge is visible under the two outermost shells. Figure 4.2(d) provides microscopic insight into the dislocation dissociation process. It is important to realize that the two edges are initially connected by two screw dislocations (only one visible in the shown cross sections), which link the two shells. Next, the inwards migration of the lower edge occurs with cross-linking of the shells.

In several nano-onions we observed isolated $\frac{1}{2}\langle 0001\rangle$ edges on the outermost shell.

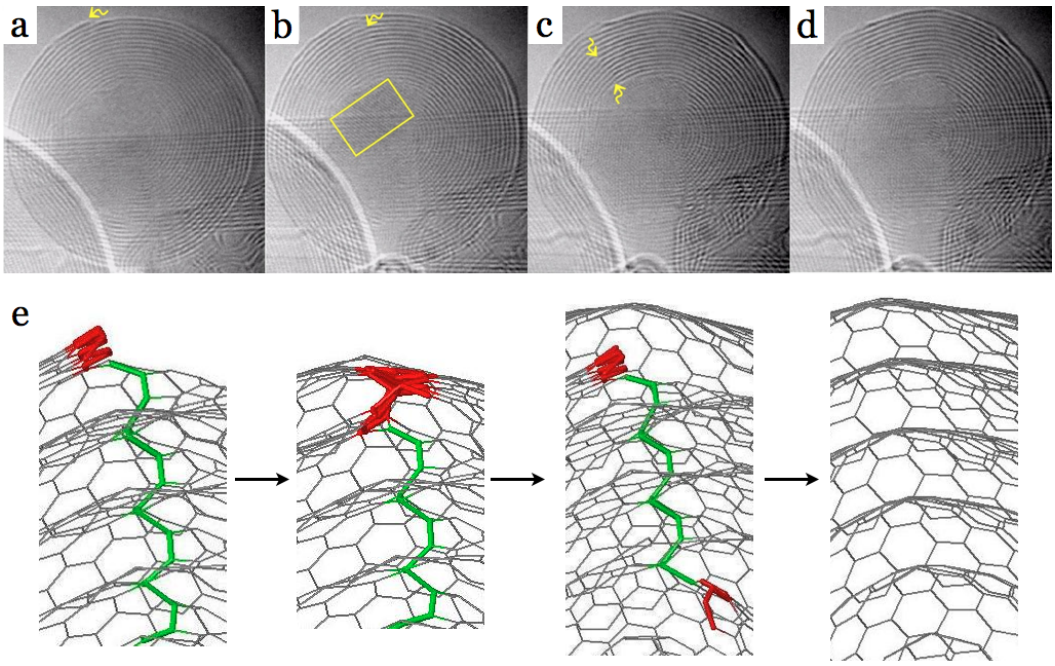

Figure 4.4: (a-d) *In situ* observation of dislocations annihilation. Arrows point out the dislocation edge. In (b), a cubic-diamond region is visible in the highlighted rectangle. (e) An atomic structural model of the annihilation process accompanied by unlinking of the shells. The atoms in red (green) belong to the edge (screw) component of the dislocation loop.

Based on the observed dislocations dissociation, we propose in Figure 4.3 a logical explanation for the presence of such edges: The evaporation of carbon atoms leads to localized breakage of the outermost shell and creation of a void exhibiting two edges of opposite sign, $\frac{1}{2}\langle 0001\rangle$ and $\frac{1}{2}\langle 000\bar{1}\rangle$. Because of the large azimuthal separation, these edges cannot recombine. Instead one edge may undergo an inwards glide accompanied by cross-linking of the shells left behind. This way, a 3D spiroid is created, which is characterized by a dislocation loop composed of two edges residing near the innermost and on the outermost shell.

Turning back to experiment, Figure 5.2 shows the opposite process of dislocation annihilation. Under prolonged electron radiation, nano-onions are known to behave as self-compressed high-pressure cells [95], to the extent that the large pressure buildup within the cores can lead to the nucleation of cubic-diamond crystals [96, 94]. Such

a transformation is observed here, Figure 5.2(b), signaling that the inhomogeneous pressure build is significant for the present experimental conditions. An edge dislocation with a Burgers vector of $\frac{1}{2}\langle 0001\rangle$ is visible on the outermost shell, Figure 5.2(a). This edge undergoes an inwards glide, in spite of the high pressure at the core: The edge is shown after crossing two, Figure 5.2(b), and six outer shells, Figure 5.2(c). A second edge dislocation of $\frac{1}{2}\langle 0001\rangle$ emerges slowly from the core, Figure 5.2(c). The two edges recombine fast in the neighborhood of the core, as the azimuthal separation is smaller. Nearly-spherical concentric shells can be noted in the last sequence of Figure 5.2(d). Based on the model shown in Figure 4.3, it is now easy to see the underlying microscopic path for this process: the nano-onion contains a dislocation loop consisting of one inner and one outer edge and two radial screw components linking the shells located in between. The inward glide of the outer edge unlinks the shells left behind, Figure 5.2(e).

4.2.1 Atomistic calculations based on REBO potential

Essential to the observed dissociation and annihilation processes is the vigorous inwards motion of an edge located on or near the outermost shell. It is important to recall that in our experimental conditions shells may lose carbon atoms, especially at the edges. Atom migration between shells might occur [97]. However, due to the stochastic nature, these aspects might not play a main role in the coherent inwards glide. It is also worth noting that the known effect of inhomogeneous pressure build up makes the motion towards the higher pressure inner region unexpected. Our observations are also against the known effect of the attraction of dislocations by free surfaces [92]. What else, besides cross-linking and unlinking of shells, goes on in the course of the inwards glide?

In order to address this question, we carried out the atomistic calculations based on REBO potential [65]. Although not a genuine representation of the nano-onions encountered in experiment, a 3D idealized spiroid derived from a nano-onion with icosahedral equispaced shells can give significant insights. An icosahedral fullerene is composed of 20 identical equilateral triangles of graphene disposed such that their corners form 12 5-membered rings. In the most stable onion structure, the triangular surfaces in different shells lie directly above one-another in a AA-like stacking. The 5-shell model spiroid shown in Figure 4.1(b) was generated by cutting each shell along like edges. In each shell, the two created armchair edges undergo slipping across each other in the radial

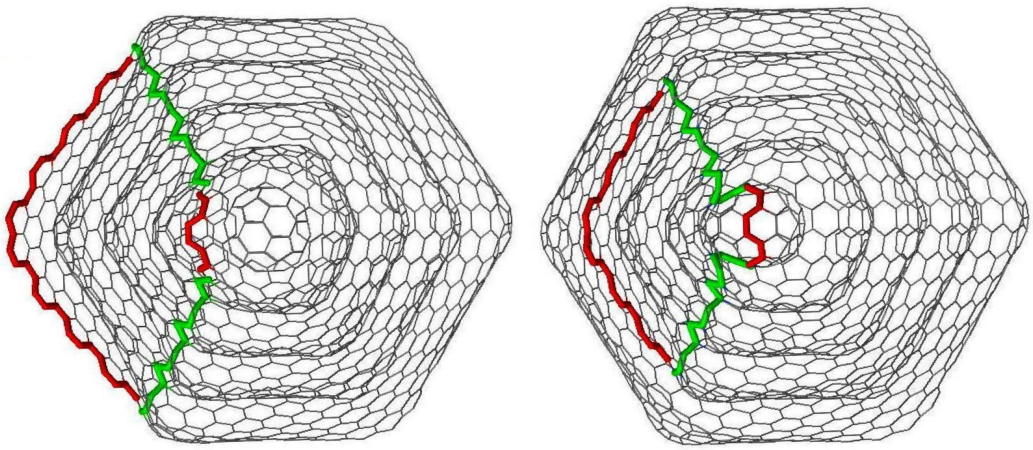

Figure 4.5: Configuration of the second stage for the two considered routes: inside-to-outside (left) and outside-to-inside (right).

direction by an amount equal to the interlayer spacing. Note that each edge, except C_{60}, contains $2(n-1)$ dangling bonds per triangular site (where n denotes the shell number with $n = 1$ for C_{60}) and, thus, neighboring edges, containing two triangular sites, differ by four dangling bonds. Although of different size, the triangle edges of the neighboring shells will fit together seamlessly (without dangling bonds) through sp^2 bonding and sp^3 bonding at the corners. Because of the van der Waals forces there is still equal spacing, $h = 3.4$ Å, between shells.

To probe the dislocation dynamics, we studied the detailed energetics of the sequential spiroid-to-onion transformation. Because the spiroid is less energetically favorable, the transformation to the optimal onion form is likely. There are two ways in which this transformation may occur: starting from the innermost shell and gliding outward, and the other way around. Figure 4.5 shows the configurations of the first glide sequence for each route, while Figure 4.6 plots the calculated energies for the full spiroid-to-onion transformation. As suggested by experiment, an intermediate sp^3 linking state between the stages was considered as the edge passes each shell. Interestingly, we obtain that the two routes are nonequivalent and only the inwards glide of the upper edge is energetically downhill. Hence, this route should dominate the dynamics, as also seen in experiment.

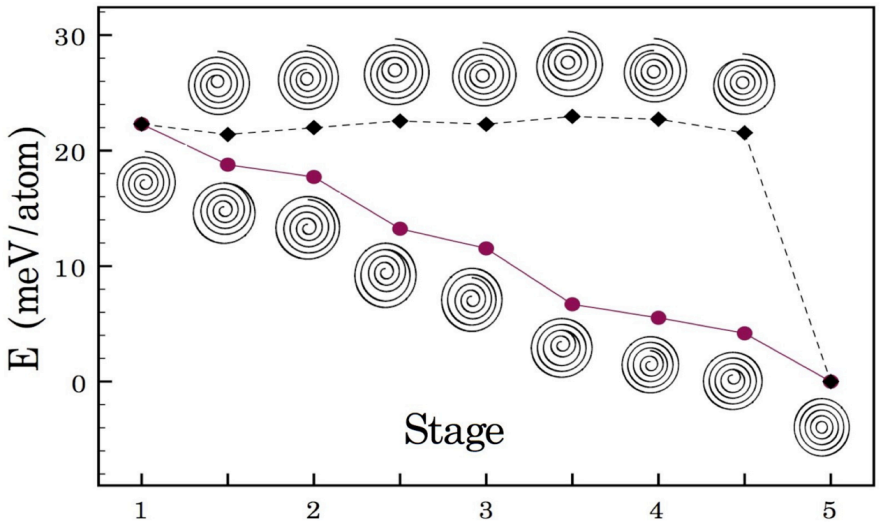

Figure 4.6: Energetics of the transformation at each stage: inside-to-outside (filled squares) and outside-to-inside (filled circles). A schematic of the cross-section is shown at each point.

4.2.2 Energy analysis and continuum modeling

Subsequently, it is useful to elaborate on the energy between two consecutive stages, i and $i+1$

$$E_{i+1} - E_i = \delta E_{\text{edge}} + \delta E_{\text{strain}}. \tag{4.1}$$

Here, the difference in van der Waals energy has been neglected. δE_{edge} captures the change in edge energy, which is stage independent for the ideal case studied here. Most importantly, it should be noted that δE_{edge} has a negative value only in the outside-to-inside route. The release of strain energy, δE_{strain}, is stage dependent and negative for both routes. In the outside-to-inside route, δE_{edge} and δE_{strain} are negative and both contribute to the inwards glide. By contrast, the outwards glide is driven only by the release of strain. Figure 4.6 indicates that the lowering in strain energy is countered by the increase in edge energy. Thus, although possible, no efficient outwards glide is expected in the nano-onion's core.

Gaining insight into larger systems is possible by relating the individual bond strain with the gross elastic deformation. We first approximate δE_{strain} with the difference in strain energy of the specific shell that undergoes the spiroid-to-onion change at a given

stage. Next, we account for the microscopic strain in the icosahedral shell viewed as the union of 12 truncated cones (pentagonal disclinations of 60°), where the strain energy of one cone comprises both bending energy of the sheet and local effects [75, 71]. The energetics of icosahedron fullerenes was discussed in Chapter 3, where the bending rigidity of graphene sheet was calculated. The total excess of energy of a single icosahedral shell is given by equation 3.6. We will further approximate the icosahedral shell by a sphere, which formation energy equals to bending energy of a thin layer (graphene) with a size-dependant effective bending rigidity. This effective bending rigidity is introduced in such a way, that the cone approximation is held. It can be found by equating the strain energy of a sphere (with this effective parameter) with energy of a union of 12 truncated cones (equation (3.6)). Such effective treatment of a problem allows us to calculate the formation energy of a spiroid shell and, thus, the strain energy difference, δE_{strain}, by performing the standard procedures of linear elasticity theory [98].

Strain energy calculations: continuum framework

In the framework of continuum elastic theory, the strain energy of carbon nanostructures is associated with the bending energy of a graphene layer, which can be approximated by a thin plate. Stress-strain relationship for a thin plate can be described as follows

$$\begin{cases} \epsilon_1 = \dfrac{\zeta}{R_1}, & \sigma_1 = \dfrac{Y\zeta}{(1-\nu^2)}\left(\dfrac{1}{R_1}+\dfrac{\nu}{R_2}\right), \\ \epsilon_2 = \dfrac{\zeta}{R_2}, & \sigma_2 = \dfrac{Y\zeta}{(1-\nu^2)}\left(\dfrac{1}{R_2}+\dfrac{\nu}{R_1}\right), \end{cases} \tag{4.2}$$

where σ and ϵ denote stress and strain tensors, R_1 and R_2 are principal radii of curvature, ζ is a coordinate in direction perpendicular to the plane, Y and ν represent Young modulus and Poissons ratio of hexagonal graphite, respectively. Using stress-strain relationship (4.2), the total strain energy can be computed by integration of the strain energy density over the entire volume as follows

$$\begin{aligned} E_{\text{strain}} = \int_V \left(\frac{\sigma_1\epsilon_1}{2}+\frac{\sigma_2\epsilon_2}{2}\right) dV &= \frac{D}{2}\int_A \left(\left(\frac{1}{R_1}+\frac{\nu}{R_2}\right)\frac{1}{R_1}+\left(\frac{1}{R_2}+\frac{\nu}{R_1}\right)\frac{1}{R_2}\right) dA, \\ D &= \frac{Yt^3}{12(1-\nu^2)}, \end{aligned} \tag{4.3}$$

where t, A and V denote thickness, surface area and volume of a plate, respectively, and D is a bending rigidity.

For a simple spherical case curvature radii (R_1 and R_2) are both equal to the radius of a sphere R. In this case, substituting the radii of curvature in equation (4.3), the strain energy becomes

$$E_{\text{strain}}^{\text{sphere}} = 4\pi D(1+\nu). \tag{4.4}$$

In order to calculate the bending energy for 3D spiroid shell, it is necessary to propose the analytical form describing its shape. One possibility is to approximate the shape of spiroid by a function, which in cylindrical coordinates (θ, z) reads as

$$\rho(\theta, z) = \left[h\left(\theta/2\pi - 1/2\right) + R_n\right]\sqrt{1 - z^2/R_n^2}, \tag{4.5}$$

where h is the inter-shell spacing and R_n is a mean radius. Knowing the shape of spiroid given by (4.5), the principal radii of curvature of this structure, $R_1(\theta, z)$ and $R_2(\theta, z)$ (correspond to the principal curvatures κ_1 and κ_2), can be calculated. To compute the principal curvatures the vector valued function in cylindrical coordinates was introduced, $\vec{r}(\theta, z) = \rho(\theta, z)\vec{e_\rho} + z\vec{e_z}$, where $\vec{e_\rho} = (\cos\theta, \sin\theta, 0)$, $\vec{e_\theta} = (-\sin\theta, \cos\theta, 0)$ and $\vec{e_z} = (0, 0, 1)$. Then a unit normal vector to the surface is

$$\vec{n} = \frac{\vec{r_{,z}} \times \vec{r_{,\theta}}}{|\vec{r_{,z}} \times \vec{r_{,\theta}}|} = \frac{-\rho\vec{e_\rho} + \rho_{,\theta}\vec{e_\theta} + \rho\rho_{,z}\vec{e_z}}{\sqrt{\rho_{,\theta}^2 + \rho^2 + \rho^2\rho_{,z}^2}}. \tag{4.6}$$

Using equation (4.6), the coefficients of the first (E, F, G) and second (L, M, N) fundamental forms are the following

$$\begin{cases} E = (\vec{r_{,\theta}}, \vec{r_{,\theta}}) = \rho_{,\theta}^2 + \rho^2, & L = (\vec{r_{,\theta\theta}}, \vec{n}) = \dfrac{2\rho_{,\theta}^2 + \rho^2}{\sqrt{\rho_{,\theta}^2 + \rho^2 + \rho^2\rho_{,z}^2}}, \\ F = (\vec{r_{,\theta}}, \vec{r_{,z}}) = \rho_{,\theta}\rho_{,z}, & M = (\vec{r_{,\theta z}}, \vec{n}) = \dfrac{\rho_{,\theta}\rho_{,z} - \rho\rho_{,\theta z}}{\sqrt{\rho_{,\theta}^2 + \rho^2 + \rho^2\rho_{,z}^2}}, \\ G = (\vec{r_{,z}}, \vec{r_{,z}}) = \rho_{,z}^2 + 1, & N = (\vec{r_{,zz}}, \vec{n}) = \dfrac{-\rho\rho_{,zz}}{\sqrt{\rho_{,\theta}^2 + \rho^2 + \rho^2\rho_{,z}^2}}. \end{cases} \tag{4.7}$$

Gaussian and mean curvatures K and H, correspondingly, are found as

$$K = \kappa_1\kappa_2 = \frac{LN - M^2}{EG - F^2}, \qquad H = \frac{\kappa_1 + \kappa_2}{2} = \frac{EN - 2FM + GL}{2(EG - F^2)}. \tag{4.8}$$

Using the definition of Gaussian and mean curvatures and substituting them into equation (4.3), the strain energy can be represented in a more convenient way as

$$E_{\text{strain}} = D\int_A \left(2H^2 + (\nu - 1)K\right)\, dA. \tag{4.9}$$

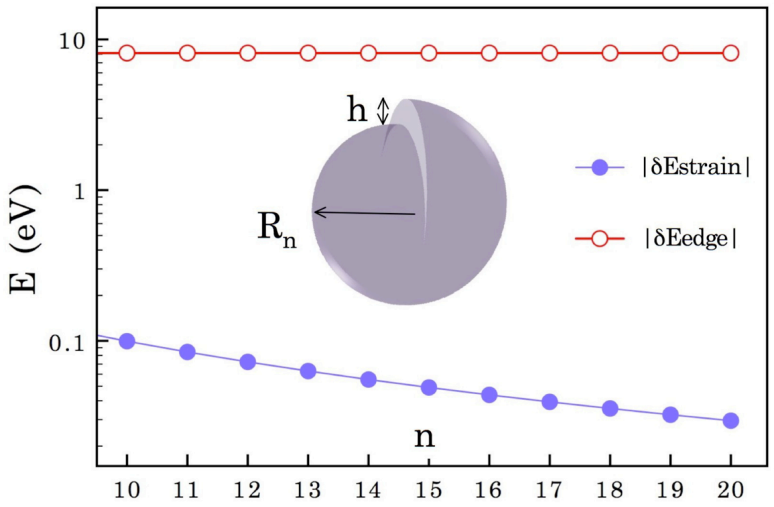

Figure 4.7: $|\delta E_{\text{edge}}|$ and $|\delta E_{\text{strain}}|$ in large radius C_{60n^2} shells, as extrapolated from the simulation data. n is the shell index and δE_{strain} is the difference in strain energy between a spherical and spiroid shell (inset) of same radius R_n.

Then we make the spherical shell approximation (4.4) and equate this energy with $4\pi D_n^{eff}(1+\nu)$ (the Poisson ratio for graphene is $\nu = 0.165$). This way a continuum shell with a size-dependent effective rigidity D_n^{eff} is defined. By substituting equation (4.7) into (4.8) and finally into (4.9), and in case, when $h/R_n \ll 1$ (valid for larger diameter shells), the total strain energy of a spiroid can be expanded in Taylor series to obtain the following relation:

$$\begin{aligned} E_{\text{strain}}^{\text{spiroid}} &= 4\pi D_n^{eff}(1+\nu) + C_0\, D_n^{eff}\,\frac{h^2}{R_n^2} + O\Big(\frac{h^4}{R_n^4}\Big), \qquad (4.10)\\ C_0 &= \frac{75+16\pi^2+45\nu}{45\pi} \approx 1.70. \end{aligned}$$

From equation (4.10) it follows, that the strain energy difference for n-th shell writes as

$$|\delta E_{\text{strain}}| = C_0\, D_n^{eff}\,\frac{h^2}{R_n^2} + O\Big(\frac{h^4}{R_n^4}\Big). \qquad (4.11)$$

The comparison between the contribution of two different components of the total change in energy (equation (4.1)) of the the specic shell, that undergoes the spiroid-to-onion transformation, namely, δE_{strain} and δE_{edge}, is shown in Figure 4.7. The

microscopically calculated value of 2.0 eV/atom for edge energy was used. Edge energy component is clearly dominated for the considered larger diameter shells. Hence, the outside-to-inside route becomes more favorable than inside-to-outside motion of the edge, which coincides with our atomistic calculations and experimental observations.

4.3 Conclusion

Fitting of the results from continuum approach (shown in Figure 4.7) to our atomistic data (see Figure 4.6) by linear least square method gives $D = 1.67$ eV. This result is in good agreement with the actual value for the bending rigidity of a graphene layer. With this parametrization, equations (4.1) and (4.11) provide a reliable basis for comparing the two routes outside the core region. Using that, we predict that for larger diameter shells, as those encountered in experiment, $|\delta E_{\text{strain}}|$ is negligible in comparison with $|\delta E_{\text{edge}}|$, Figure 4.7. Thus, the outwards glide should be very unlikely outside the core region. Because of the consistent edge lowering effect, the inwards glide appears viable for processes involving both cross-linking, such as dislocations dissociation, and unlinking, such as dislocations annihilation.

Dislocation processes have important implications, especially for mechanical properties. Because of their spherical shape, nano-onions are researched for tribological applications [99]. The efficient cross-linking achieved by dislocation glide may prevent shell sliding, thus, modifying the friction-reducing properties. The transport of carbon atoms in graphitic lattices is of great importance and the ability of carbon atoms to jump between the graphitic shells has been already recognized [97]. An inwards glide appears an easier route to transport atoms through the dislocation line and could shed light on the growth mechanism of nano-onions. Ozawa et al. [7] proposed spiroidal growth, in which all shells become first cross-linked through an onion-to-spiroid interchange. The spiroid stage favors accretion of carbon atoms on the outside edge. In light of our results, a post-growth retrieving of the nested onion via an inwards glide appears very likely.

Chapter 5

Axial screw dislocations in zinc oxide nanotubes and nanowires

The variety of one-dimensional zinc oxide (ZnO) nanostructures, such as nanorods (NRs), nanowires (NWs), and nanotubes (NTs), has been investigated experimentally and theoretically for the last few decades due to their unique physical and chemical properties [100, 101, 102]. Recent experimental advances have provided unprecedented level of control in synthesis of NW and NT of ZnO [3, 103] and other materials [44, 45, 104] grown by engaging dislocations, where a seeded axial screw dislocation of a well-defined Burgers vector provides the self-perpetuating steps for enabling the quasi-one dimensional growth.

In this work we focus on studying the effects of the screw dislocations in ZnO NTs and NWs, which possess a regular wurtzite structure and appear to grow into twisted configurations of specific sizes [3]. This class of highly anisotropic structures is exciting for many reasons. Twisted NWs and NTs with finite thickness made out of nonlayered materials represent a novel organization of matter, similar but not identical to multi-walled NTs made out of layered materials, such as carbon or boron nitrite. The way in which a screw dislocation influences the stability and the extraordinary mechanical and electrical properties of these nanostructures remains an open and important problem.

To properly describe the screw-dislocated ZnO NTs and NWs structures, this research employs the fundamental atomistic simulation techniques, discussed in Chapter 3,

that are specially adapted for this purpose. The current Chapter presents the study of the role of axial screw dislocations introduced in (1) one-atom-thin ZnO NTs, the work reported in [34], and (2) thick ZnO NWs and NTs with the thickness greater than one-atom layer, published in [35, 36].

5.1 One-atom thin ZnO nanotubes

The dislocation concept as well as continuum description of dislocations were introduced in details in Chapter 2. According to elasticity theory, a screw dislocation lying parallel with the axis of a thin rod or a tube, Fig. 2.4, is stabilized at a central location by an Eshelby twist [40] of well-defined magnitude given by eq. (2.4). The formation energy per unit length of a screw-dislocated isotropic tube with outer and inner radii denoted by R and r writes as

$$E = \frac{Gb^2}{4\pi} \ln \frac{R}{r} - \frac{Gb^2}{4\pi} \frac{R^2 - r^2}{R^2 + r^2} + S, \tag{5.1}$$

where G is the shear modulus. The above expression contains three different terms: energy associated with elastic strain field created by the screw dislocation (first term), energy reduction attributed to the Eshelby twist (second term), and surface energy (third term) of both outer and inner surfaces for non-layered materials (e.g. ZnO) or bending energy related with rolling of a sheet into a tube for layered materials such as carbon or boron nitride. From a continuum perspective, the one-atom thick tube can be represented by shell of a certain thickness, i.e. $r \neq R$. Then, the first two terms due to the presence of dislocation will bring non-vanishing contributions and the NT total strain energy will contain shear strain. Alternatively, the monolayer can be represented by a continuum membrane without thickness, i.e. $r = R$. Then, the first two terms in eq. (5.1) vanish. This implies that there is no shear energy cost to create an axial screw dislocation and, hence, the Burgers vector magnitude can be large.

Because in general the mechanics of an axial glide in a nanostructure is not yet understood, the magnitude of the atomic-scale Eshelby twist, and hence the resulting translational periodicity, is not a priori known. This makes it difficult to carry out systematic microscopic calculations in the standard periodic framework.

Efficient microscopic modeling of screw dislocated NTs was only recently achieved [105] due to the development of objective molecular dynamics (MD) [89], a relatively new

microscopic technique based on the objective structures [90] concept. By coupling [58] it with the computationally efficient DFTB treatment of the chemical binding implemented in the code Trocadero [106], objective MD enables simulating with minimal symmetry constraints the interplay between the classical ionic and quantum electronic degrees of freedom under an arbitrary twist and chirality. Using objective MD and well tested two-center nonorthogonal DFTB models described in Chapter 3, we investigate the Eshelby's twist mechanics in one-atom thin hexagonal layers of ZnO. The motivation for our study is threefold.

Firstly, it would be interesting to understand and compare rolling traits of ZnO as this material is representative for the nanotubes made out of nonlayered material. ZnO exhibits a typical wurtzite structure and helical ZnO NTs have been synthesized along the c direction by catalyst-free dislocation-driven growth [2]. While the thicker-walled ZnO NTs are faceted and display a hexagonal cross section [23, 3, 2], the single-wall nanotube (SWNT) has a ZnO hexagonal wall and a cylindrical cross section [107].

Secondly, the SWNTs of ZnO are the structural analogue of carbon (C) NTs with alternating Zn and O atoms substitute for C atoms, and are isotropic in the linear elastic regime. When this approximation holds, the magnitude of the Eshelby's twist can be analytically predicted based on the standard rolled-up construction of C NTs. Recent investigations [108, 109] indicated that the thicker, three-atomic-layers of MoS_2 and TiS_2 exhibit a departure from the rolled-up predictions, manifested in diameter-, chirality-, and wall-structure- dependent intrinsic twists. Other symmetry-constrained DFTB calculations [110] indicated that due to the well-known strain-sensitivity of the electronic properties, even the widely-studied C NTs exhibit intrinsic twist, although of a much lower magnitude. Hence, it would be interesting to know if such intrinsic twists are present in other one-atom thick NTs with electronic properties which are markedly less sensitive to strain.

Thirdly, these NTs offer a number of appealing properties. ZnO NTs are especially investigated in relation with their wide-bandgap semiconducting, mechanical, and piezoelectric attributes. Understanding the effects of the extended screw-dislocations is important as it could provide a general means for tuning these properties.

This section is organized as follows: (1) the standard rolled-up construction and the original screw dislocation construction introduced by Iijima [17] and employed

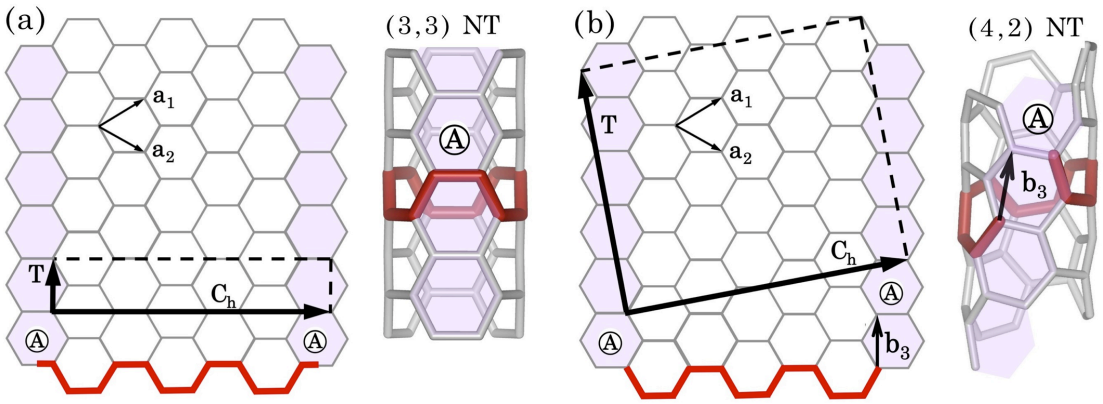

Figure 5.1: Schematics for the two ways of forming (a) (3,3) and (b) (4,2) NT, from the ideal flat hexagonal layer: by rolling-up the big rectangle bounded by the chiral $\mathbf{C_h}$ and translational $\mathbf{T}$ vectors, and by rolling-up a ribbon such as the hexagons labelled with "A" become superimposed. Lattice vectors $\mathbf{a_1}$ and $\mathbf{a_2}$, and Burgers vector $\mathbf{b_3}$ along the hatched hexagon are also shown. The row of hatched hexagons form a helix on the tube. The objective unit cells used in the calculations are shown with thicker (red) lines.

in [105, 108, 109] to simulate chiral nanotubes are reviewed; (2) the simulation results of the obtained relaxed structures and comparison with the ideal rolled-up structure predictions for helical ZnO NTs together with the behavior of electronic properties with chirality and diameter are presented; and (4) the results are summarized and discussed.

5.1.1 Screw dislocation representation of hexagonal nanotubes

We anticipate that in the one-atom-thin layer, the Eshelby's twist executed by this layer coincides with the nanotube chirality, as predicted by the standard rolled-up construction. The one-atom thin or SWNT of ZnO is the structural analogue of carbon SWNT with alternating Zn and O atoms substituting for C atoms. An (n, m) SWNT is commonly conceptualized in the literature by the rolled-up construction, which involves *pure* mechanical rolling of a flat hexagonal-lattice strip along the (n, m) hexagonal lattice vector into a seamless cylinder [111]. In the unrolled representation, the n and m indices represent the components of the circular circumference vector $\mathbf{C_h}$ of the nanotube on the lattice vectors $\mathbf{a_1}$ and $\mathbf{a_2}$ of the honeycomb lattice, i.e. $\mathbf{C_h} = n\mathbf{a_1} + m\mathbf{a_2}$. By convention, $\mathbf{a_1}$ and $\mathbf{a_2}$ are taken along the two zigzag chains as shown in Fig. 5.1. The radius of this tubule writes $R_0 = |\mathbf{C_h}|/2\pi = a\sqrt{n^2 + nm + m^2}/2\pi$. Here $a = |\mathbf{a_1}|$ is

the length of the primitive vector of the flat layer. The SWNT chirality is measured by the angle $\chi = \pi/6\text{-arcsin}[(\sqrt{3}m)/(2\sqrt{n^2+nm+m^2})]$ enclosed by $\mathbf{C_h}$ and the closest of the three armchair chains in the flat graphene sheet. The special cases corresponding to $(n,0)$ and (n,n) are the zigzag and armchair configurations, respectively.

The fundamental property of an infinitely long NT is apparently its translational periodicity, described by the translational vector $\mathbf{T}$ pointing along the axial direction of the NT. In the unrolled representation, the translational vector $\mathbf{T}$ is orthogonal to $\mathbf{C_h}$. While the precise expression of $\mathbf{T}$ can be found in literature [111], what matters here is that it points into a direction which is distinct from one of the glide directions of the graphene sheet, Fig. 5.1. The underlying assumption is that during the rolling process of the unit cell delineated by $\mathbf{T}$ and $\mathbf{C_h}$, the translational symmetry is preserved even though the bond lengths and angles between atoms will change due to finite curvature effects. The infinitely long NT structure is then described with:

$$\mathbf{X}_{j,\zeta} = \mathbf{X}_j + \zeta\mathbf{T}, \tag{5.2}$$

where $\mathbf{X}_j$ are the coordinates of the atoms located in the unit cell, integer ζ indexes the unit cell replica.

An ideal NT possesses also helical symmetry, described in the unrolled representation by screw vectors comprised of both rotational and translational components, i.e. with components along both $\mathbf{C_h}$ and $\mathbf{T}$. One such vector is the Burgers vector $\mathbf{b_3} = \mathbf{a_1} - \mathbf{a_2}$, shown in Fig. 5.1. By evaluating its axial and circumferential components, one obtain that screw vector $\mathbf{b_3}$ is associated with a θ_0 angular rotation and a T_0 axial translation given by

$$\theta_0 = \frac{\pi(n-m)}{n^2+nm+m^2}, \qquad T_0 = \frac{\sqrt{3}a(n+m)}{2\sqrt{n^2+nm+m^2}}. \tag{5.3}$$

The makeup of helical C NTs was depicted by Iijima in another way, namely by the rolling-up along the tube axis of a graphene ribbon in the armchair orientation (along the glide direction indicated by the Burgers vector b_3), see Fig. 5.1, such that the hatched edge hexagons are superimposed [17]. In the cylindrical geometry, the gliding of the edges past one another represents an axial screw dislocation [105, 108]. Indeed, in the cylindrical structure of an (n,n) NT, its chiral vector keeps a closed ring composed of $4n$ atoms. A slip along the nearly-axial helical glide path introduces an integer number of hexagons i between the head and the tail of the old chiral vector and thus leads to

a change in NT's chirality. Of course, during this process the cylindrical structure of the armchair NT is maintained and its new chiral vector keeps a closed ring, i.e. the dislocation between the head and the tail of the new chiral vector is zero. The wrapping indexes of the new chiral pattern can be easily obtained by identifying on the unrolled NT representation the new chirality vector connecting the overlapping hexagons. It is an easy task to show that one glide step introduces a characteristic $(+1, -1)$ change in NT's indexes [105]. The repeated glide defines a nearly equal radius family of NTs with indexes (n, n), $(n+1, n-1)$,...,$(2n, 0)$. An arbitrary NT with indexes $(n+i, n-i)$, where $i \in [0, n]$, can be viewed as a screw-dislocated armchair NT that undergoes a twist of a lattice per unit length given by

$$\gamma_0 = \frac{\theta_0}{T_0} = \frac{b}{2\pi R_0^2 \sqrt{1 - \left(\frac{b}{2\pi R_0}\right)^2}}. \tag{5.4}$$

Here, $b = i|\mathbf{b_3}|$ is the magnitude of the Burgers vector. According to eq. (2.4), the twist rate for an one-atom thick tube, where inner and outer radii coincide, is $\gamma'_E = b/2\pi R_0^2$. This means that the twist rate calculated under pure rolling assumption, as given in eq. (5.4), converges to continuum membrane elasticity result when the tube radius increases (valid for $i < n$). Even for the extreme case of zigzag NT ($i = n$) the calculated twist rate of $\gamma_0 = b/\sqrt{3}\pi R_0^2$ is very close to continuum predictions.

What is useful in the screw-dislocation construction based on the nearly-axial glide is that under the helical repetition rule indicated by $\mathbf{b_3}$, one can alternatively describe the set of NTs from these families based on the same $4n$ atoms contained in the small translational unit cell of the armchair (n, n) NT. Let $\mathbf{X}_j$ be the atomic positions in the open ring, after the axial glide took place. Positions $\mathbf{X}_{j,\zeta}$ of the atoms located in the objective cell replica indexed by integer ζ are then obtained with

$$\mathbf{X}_{j,\zeta} = \mathbf{Q}^\zeta \mathbf{X}_j + \zeta \mathbf{T_0},\ j = 1, ..., 4n. \tag{5.5}$$

The rotational matrix $\mathbf{Q}$ and the axial vector $\mathbf{T_0}$

$$\mathbf{Q} = \begin{pmatrix} \cos\theta_0 & -\sin\theta_0 & 0 \\ \sin\theta_0 & \cos\theta_0 & 0 \\ 0 & 0 & 1 \end{pmatrix}, \quad \mathbf{T_0} = \begin{pmatrix} 0 \\ 0 \\ T_0 \end{pmatrix} \tag{5.6}$$

describe the helical transformation indicated by the screw vector $\mathbf{b}_3$.

We emphasize that other views of chiral NTs as screw-dislocated achiral NTs are possible. To address C NT growth [6], an ingenious representation was proposed that involves $(n,0)$, $(n,1)$, ..., (n,n) obtained via glides along $-\mathbf{a_1}+2\mathbf{a_2}$ direction combined with addition and removal of atom chains. The representation used here base on Iijima's construction of helical NTs has relevance in the torsional mechanical response [17]. It relates (n,n), $(n+1,n-1)$, ..., $(2n,0)$ NTs without involving removal or addition of atomic chains.

5.1.2 Simulation results

Using the DFTB symmetry-adapted theoretical framework, we have performed objective calculations on four ZnO NT families ($n=3,6,8$) generated by introducing axial screw dislocations in (n,n) NT structures. Additionally, a large collection of armchair and zig-zag ZnO NTs in the $1-4$ nm diameter range was considered. For a comparison, the systematic calculations performed on ZnO NTs, were supplemented with additional calculations carried out on selected small diameter C NTs.

The linear combinations of atomic orbitals were sampled for 50 κ values of the helical Bloch phase. The initial structural information for any NT is adopted from the rolled-up approximation, for which the free parameters θ_0 and T_0 can be obtained with the simple expressions given before. Next, the stress-free atomic positions and the actual DFTB Eshelby's twist parameters θ_E and T_E are identified by applying a conjugate gradient minimization procedure to the potential energy.

Optimized nanotube structures

One advantage of the current approach is that it enables us to separate the curvature from the chirality effects. The first goal is to determine how well the translational symmetry and the ideal rolled-up predictions hold. The results of our structural optimizations indicate that for small diameter chiral NTs, the axial relaxation under fixed angle θ_0 is not sufficient to obtain the stress-free states. As exemplified in Fig. 5.2 for the $(3,3)$, ..., $(6,0)$ NT family, further angular relaxation under fixed $|T_E|$ exhibits a parabolic dependence and can lower the energy. The angle values of the stress-free chiral structures θ_E deviate substantially from the predicted θ_0.

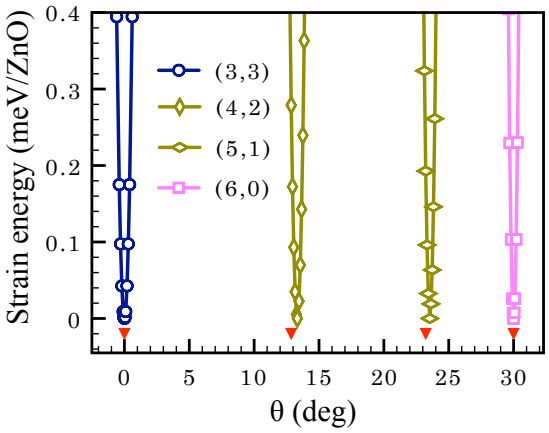

Figure 5.2: Torsional strain energy versus θ for the (3,3), (4,2), (5,1), and (6,0) ZnO SWNTs. The energy minima indicate the θ_E angles of the stress-free NTs, while the arrowheads indicate the θ_0 values.

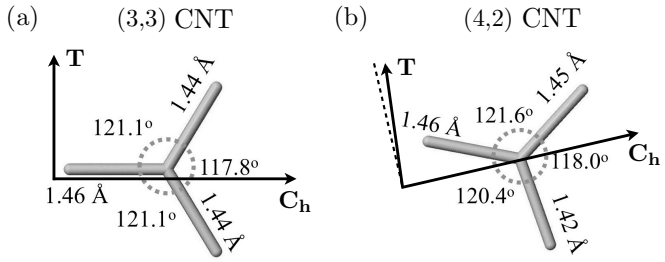

Figure 5.3: Bond lengths and angles obtained by mapping in 2D the DFTB optimized (a) $(3,3)$ and (b) $(4,2)$ C SWNTs. The NT axis is in the vertical direction.

Unlike the flat layer, the structure of these narrow NTs is characterized by non-equal bond-lengths and bond-angles. The data for $(4,2)$ NTs summarized in Table 5.1, detail the significant departure from the bond lengths and angles given by the rolled-up prediction. The most circumferentially-oriented bonds are the most affected. For example, while the rolled-up prediction gives a 1.399 $\AA$ length for the most circumferential bonds in a $(4,2)$ C NT, the DFTB relaxations obtained a 1.430 $\AA$ value. Such atomistic relaxations lead to differences not only between the optimized R and non-optimized R_0 radii, but also between the optimized θ_E and T_E and the non-optimized θ_0 and T_0 structural parameters. Hence, with respect to the the rolled-up construction, the $(4,2)$ NT structures store both a circumferential and a helical pre-strain.

Table 5.1: The DFTB structure of (4,2) ZnO, and C SWNTs compared with the rolled-up predictions.

Material:	ZnO	C
Bond lengths ($\mathring{A}$):		
DFTB	1.925, 1.913, 1.922	1.430, 1.420, 1.449
Rolled-up predictions	1.870, 1.904, 1.898	1.399, 1.425, 1.420
DFTB mapped in 2D	-	1.456, 1.420, 1.454
Bond angles (deg):		
DFTB	119.5, 119.2, 117.8	118.4, 119.1, 115.1
Rolled-up predictions	118.1, 120.3, 113.2	118.1, 120.3, 113.2
DFTB mapped in 2D	-	120.4, 118.0, 121.6
NT Radius ($\mathring{A}$):		
DFTB	2.852	2.142
Rolled-up predictions	2.778	2.079
Structural parameters:		
DFTB T_E ($\mathring{A}$), θ_E (deg)	3.240, 13.33	2.411, 13.42
Rolled-up T_0 (Å), θ_0 (deg)	3.239, 12.86	2.424, 12.86
Buckling ($\mathring{A}$):		
DFTB	0.134	0
Rolled-up predictions	0	0

The presence of helical pre-strains alters the translational unit cells identified on the ideal flat hexagonal layer. To illustrate this point, we mapped in 2D the DFTB relaxed structures of the (3,3) and (4,2) C NTs. The obtained bond lengths and angles, depicted in Fig. 5.3, reflect that hexagonal layer is deformed. For the (3,3) C NT, the lattice is elongated along the $\mathbf{C_h}$ and $\mathbf{T}$ directions, which remain perpendicular onto each other. However, for the (4,2) C NT case the lattice is additionally sheared and vector $\mathbf{T}$ acquires a small component along $\mathbf{C_h}$, thus becoming a screw vector. Hence, the translational symmetry depicted by the translation vector $\mathbf{T}$ is broken by the intrinsic twist $(\theta_E - \theta_0)/T_E$.

Our calculations indicated helical ZnO NTs store intrinsic twists. Focusing on the $(3,3)$, ..., $(6,0)$ NT family, $(4,2)$ and $(5,1)$ NTs possess 1.5°/nm and 1.0°/nm values of twist rate for ZnO case, while for C NTs values are slightly larger, namely, 2.3°/nm and 1.1°/nm, respectively. The results for C NT family are close to reported earlier [110] from calculations based on higher symmetry two-atoms "helical-angular" cells.

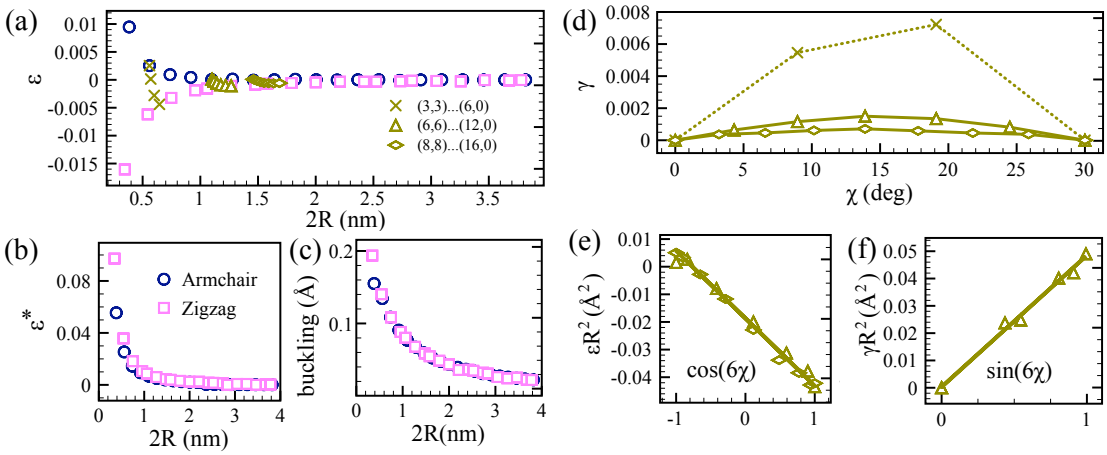

Figure 5.4: Optimized structures of ZnO SWNTs. Dependence of the intrinsic (a) axial pre-strain, (b) radial pre-strain, and (c) wall buckling on diameter. (d) Dependence of the intrinsic shear on chirality. Scaling of (e) the axial pre-strain and (f) intrinsic shear strain (both multiplied by R^2) with lowest symmetry-allowed order in chiral angle.

To give a broader view of the deviations from the ideal rolled-up construction, Fig. 5.4 plots the variations with the NT diameter of the axial pre-strain $\varepsilon = (T_E - T_0)/T_0$, the radial pre-strain, defined as $\varepsilon^* = (R - R_0)/R_0$, the buckling of the surface, defined as the mean radius of the O atoms minus the mean radius of the Zn atoms, and the shear pre-strain, defined as $\gamma = R(\theta_E - \theta_0)/T_E$. We obtain the following insights: (i) The rolled-up construction works very well for ZnO only at diameters larger than ~ 2 nm. (ii) As the NT diameter decreases, ε displays an increased spread after chirality. In the nearly-equal diameter families, the armchair tubes are the most elongated while the zig-zag ones are the most compressed. (iii) As the NT diameter decreases, ε^* is also significant but appears to be chirality-independent. Our data for ZnO can be fitted with the power law as $\varepsilon^* = 0.2(R/\mathring{A})^{-2}$. (iv) The amount of buckling is independent of the tube helicity as well. In ZnO NTs the wall bucking is however presented to some degree even at large diameters, as reflected by the scaling law $0.4(R/\mathring{A})^{-1}$ for ZnO obtained by fitting the atomistic data presented in Fig. 5.4(c). Finally, (v) the γ stored in the NT's wall is both diameter and chirality dependent. It is significant only at the smallest diameters. As can be seen in Fig. 5.4(d), γ is absent in the armchair and zig-zag NTs and it is maximal near the 15° chirality.

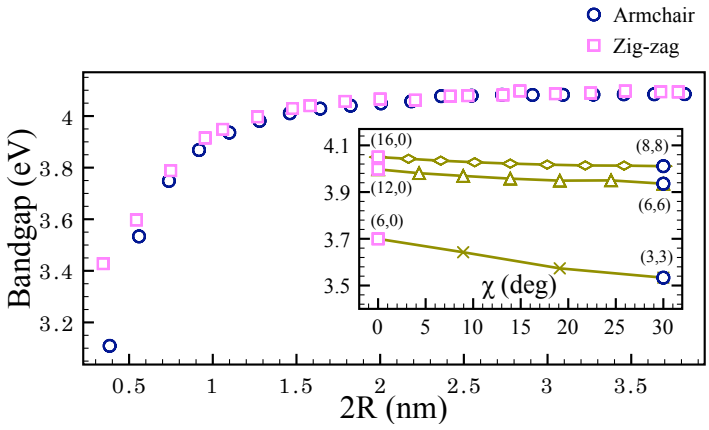

Figure 5.5: Bandgap dependence on diameter and chirality for ZnO SWNTs.

For a compact characterization of the ZnO SWNT structural parameters, we appeal to simple functional forms constructed based on symmetry arguments. At constant R, the developed anisotropy between special armchair and zig-zag directions implies that both the ε and γ pre-strains must have a 60° period in their chirality angle dependence. Additionally, we find that the radial scaling law identified for ε^* is suitable for ε and γ data as well. Indeed, Fig. 5.4(e,f) show nearly linear dependences of the R^2 augmented ε and γ to the lowest symmetry-allowed order in chiral angle. Specifically, we obtained $\varepsilon = -0.03(R/\mathring{A})^{-2}\cos(6\chi) - 0.02(R/\mathring{A})^{-2}$ and $\gamma = 0.05(R/\mathring{A})^{-2}\sin(6\chi)$.

Electronic properties of single-walled ZnO nanotubes

Having identified the stress-free NT morphologies, we are now in the position to analyze their electronic states. Our DFTB parameterization is designed to describe well the structural properties of ZnO materials. Unfortunately, it overestimates the bandgap values. For example, the used parameterization predicts a bandgap of 6.3 eV for the bulk wurtzite ZnO phase, while the experimentally measured value is 3.4 eV. For the purposes of predicting the fundamental bandgaps in ZnO NTs, the original parameters have been slightly altered: the on-site energy value for the 4s electron of Zn was replaced by the experimental first ionization energy (the parameter is changed from -0.2079 a.u. to -0.3527 a.u.). This modification insures that the bandgap of the wurtzite phase is reproduced.

The electronic structure of ZnO NTs appears to be more sensitive to curvature than to chirality. The calculated bandgaps of all the ZnO NTs studied are displayed in Fig. 5.5 as function of their diameters. The bandgap increases with diameter. Above $\sim$ 2 nm, it converges rapidly, regardless of chirality, to the 4.08 eV value of the flat layer. Below $\sim$ 2 nm in diameter, the bandgap begins to exhibit a weak dispersion after chirality, that becomes non-negligible for the smallest diameter NT considered here, Fig. 5.5 (inset).

5.1.3 Summary

The objective molecular dynamics technique, which accounts for helical symmetry explicitly, allowed us to systematically investigate the Eshelby's twist mechanics in ZnO monoatomic layers. We addressed a large catalog of NTs and obtain scaling laws beyond the errors of the numerical procedures.

For ZnO SWNTs with $2R >\sim$ 2 nm, we obtained that the Eshelby's twist mechanics is equivalent with the rolled-up construction, and hence, isotropic continuum idealization can be used for these structures. This also means that, as predicted by eq. (5.1) in the $r = R$ limit, chiral NTs store only bending strain energy S. The lack of shear strain energy in the NT wall once more [112] suggests the invalidity of the continuum shell model associated with the monolayer. For $2R <\sim$ 2 nm, the detailed structure analysis of our optimized NTs indicated a systematic departure from the rolled-up construction manifested in radial, axial, and shear pre-strains that exhibit a power law scaling with curvature. The presence of the shear strain, manifested into an intrinsic structural twist, removes the NT translational periodicity predicted by the rolled-up prediction. Therefore, care must be exercised in future numerical studies of chiral nanotubes relying on periodic boundary conditions.

Qualitatively similar results in the rolling traits were obtained for SWNTs made out of boron nitride [34], which is a layered material, in comparison with non-layered ZnO structures. Differences can be found only in the scaling laws of pre-strains with the NT radius and in the magnitudes of pre-strains and wall bucklings. Consequently, the intrinsic twist effects become important for NTs with $2R <\sim$ 2 nm in both layered and non-layered structures, and they are common for a variety of SWNTs made out of different materials.

The presence of the pre-strains in small diameter NTs, indicate that the NT wall stores not only bending but also in-plane axial and shear strain energy. The discrepancy with the prediction given by eq. (5.1) in the $r = R$ limit is due to the loss of isotropy in the NT wall. It is useful to realize that the axial and shear pre-strains observed in smaller diameter NTs are ultimately related to the significant distortion of the hexagonal lattice symmetry.

5.2 Thick ZnO nanotubes and nanowires

Based on macroscopic elastic theory, Eshelby predicted that a whisker containing a screw dislocation exhibits a stabilizing torsional deformation, which depends directly on the magnitude of the Burgers vector. Interestingly, all the experimentally observed NWs and NTs containing axial screw dislocations were twisted, prompting comparisons [44, 45, 3, 113] with the Eshelby model originally developed for the much larger scale. Nevertheless, the measured [113] was sometimes found to be only in semi-qualitative agreement with predicted by model value. On a broader view, it is unclear if any disagreement between experiment and the continuum model should be attributed to a possible invalidation of the classical continuum model by the presence of surface effects, or to the extraordinary challenges associated with measuring the atomic scale twist.

The open-core elastic dislocation model of Frank [39] and the elastic Eshelby model predicting the macroscopic twist underwent by a thin rod [40, 41] containing a screw dislocation, provide a starting point for understanding the structural transition from screw-dislocated NWs to NTs. For large Burgers vectors, it is energetically more favorable for dislocation to become hollow by removing the crystalline material adjacent to the dislocation line and creating an additional surface in the form of hollow tube. Nonetheless, the detailed stabilization mechanism leading to the observed NTs is unknown mainly because the applicability of the Eshelby model to screw-dislocated nanostructures is not warranted by recent experimentation [45, 113]. In twisted PbSe NWs with R in the 30-50 nm range [45], the estimation of the Burgers vector magnitude using the Eshelby model [40] indicated a somewhat surprisingly large value [113], attributed by those authors to the presence of a super screw dislocation. In InP NWs with $R = 10$ nm, the measured twist rate exceeded by up to 100% the value estimated

with Eshelby model [40] based on the minimal Burgers vector [113]. This result was interpreted as a significant deviation from continuum.

Whereas the stability and properties of pristine ZnO NWs and NTs have been relatively well explored [114, 115, 116, 117, 118], particularly through microscopic simulation, the screw-dislocated structures are not within the reach of standard approaches. The connection between thermodynamical stability and Eshelby's mechanics in these structures calls for a fresh approach.

5.2.1 Methodology

Similar to the case of SWNTs, twisted screw-dislocated structures of thick ZnO NTs and NWs with a uniform helical symmetry have a unit cell size corresponding to the size of the helical motif. Such large number of atoms prohibits calculations adopting translational symmetry via PBC. Instead, the calculations reported here were carried out with objective MD [89] coupled [58, 119, 34] with a DFTB methodology [120, 106] discussed in details in Chapter 3. The valence shell basis set used here comprises *sp* basis functions for O and *spd* for Zn. In objective MD, we describe the infinitely long pristine and screw-dislocated NWs and NTs as objective structures [90], from basic repetition rules involving translations and rotations

$$\mathbf{X}_{j,(\zeta_1,\zeta_2)} = \mathbf{Q}_2^{\zeta_2}\,\mathbf{Q}_1^{\zeta_1}\mathbf{X}_j + \zeta_1\mathbf{T}_1. \tag{5.7}$$

Index j runs over the N_0 atoms at the positions $\mathbf{X}_j$ inside the objective domain, while index ζ_1 and ζ_2 label various replicas of the domain. The helical operation applied to the objective domain is defined by the rotational matrix $\mathbf{Q}_1$ of angle θ_1 and the axial vector $\mathbf{T_1}$, the angular symmetry is described by the rotational matrix $\mathbf{Q}_2$ of angle θ_2. With the symmetry-adapted treatment of the electronic states [58], the structural parameters $\mathbf{T_1}$ and θ_1 can take arbitrary values, permitting us to find the optimal configuration via conjugate gradient relaxations. As an example, translational and objective unit cells are demonstrated for pristine ZnO NW and NT structures in Fig. 5.6. In addition, the calculations for two screw-dislocated NTs of the same stoichiometry L and Burgers vector magnitude, but unequal wall thickness, which exhibit different intrinsic twist values and very different formation energies E_f, are also shown in Fig. 5.7.

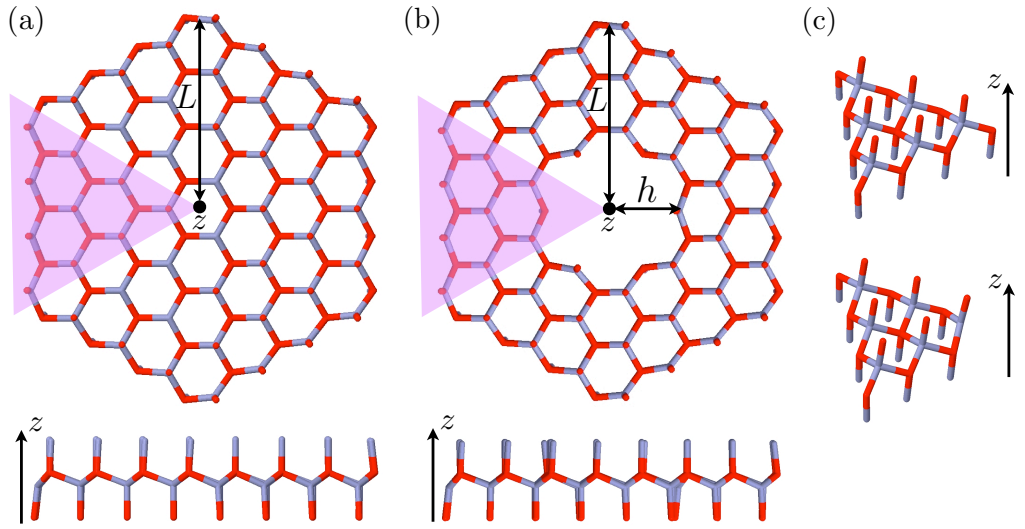

Figure 5.6: Axial (top) and side (bottom) views on the optimized translational unit cells of pristine (a) $L = 4$, $h = 0$ NW and (b) $L = 4$, $h = 1$ NT made out of ZnO in wurtzite phase, where the hatched areas denote the objective simulation domains that are shown in (c) for $\{4, 0\}$ NW (top) and $\{4, 1\}$ NT (bottom).

Symmetries of pristine and screw-dislocated ZnO nanotubes.

An arbitrary pristine NW, defined as a solid structure, is characterized by the number of the atomic layers L, as shown in Fig. 5.6(a). From each pristine NW a collection of NTs can be created by systematically removing inner atomic layers. These NTs can be uniquely denoted by $\{L, h\}$, where $h = 1, ..., N - 2$ is the number of missed inner atomic layers, which quantifies the size of the central hole, see Fig. 5.6(b). The particular $h = L - 1$ monolayer case, which deserves special attention, was considered in the previous section. The presence of an axial screw dislocation is denoted by a subscript giving the magnitude of the Burgers vector, as $\{L, h\}_{kb}$, where b represents the magnitude of the minimal possible Burgers vector and k is an integer number. As an illustration, the two relaxed screw-dislocated ZnO NTs, namely $\{5, 1\}_{3b}$ and $\{5, 2\}_{3b}$, are shown in Fig. 5.7.

ZnO NT characterized as $\{L, h\}$, as well as NW $\{L, 0\}$, can be represented by a set of faceted zigzag SWNTs denoted by $(6l - 3, 0)$, where $l = h + 1, h + 2, ..., L$, as

Table 5.2: Objective domain parameters of ZnO NTs, where N_0 denotes the number of atoms in the domain, $n^{'}$ is the greatest common divisor of $(6l-3-k)$ and $2k$. θ_s and T_s are given in eq. (5.8), $\bar{\theta}_s$ and $\bar{T}_s$ are some averaged quantities.

NT	SWNT	θ_1	θ_2	T_1	N_0
$\{L, L-1\}$	$(6L-3, 0)$	$\pi/3$	$2\pi/3$	$T/2$	$2(2L-1)$
$\{L, h\}$	$\sum_{l=h+1}^{L}(6l-3, 0)$	$\pi/3$	$2\pi/3$	$T/2$	$2(L^2-h^2)$
$\{L, L-1\}_{kb}$	$(6L-3-k, 2k)$	θ_s	$2\pi/n^{'}$	T_s	$12(2L-1)/n^{'}$
$\{L, h\}_{kb}$	$\sum_{l=h+1}^{L}(6l-3-k, 2k)$	$\bar{\theta}_s$	$2\pi/n^{'}$	$\bar{T}_s$	$12(L^2-h^2)/n^{'}$

shown in Table 5.2. Then each faceted zigzag tube should contribute $(2l-1)$ atoms into the objective unit cell of the whole NT structure with $\theta_1 = \pi/3$, $\theta_2 = 2\pi/3$ and $T_1 = T/2$, where T is a translation periodicity for a zigzag tube. As a result, the objective treatment reduces the simulation domain size by six times in comparison with the unit cell constructed according to PBC.

To rationalize the description of screw dislocated NTs, first consider SWNTs. Either armchair [17, 34] or zigzag [6] configuration can be chosen to represent the non-dislocated structure for hexagonal SWNTs because of the lack of the shear energy cost to create an axial screw dislocation, which leads to the arbitrary values of Burgers vector. However, the reference structure becomes important for thicker NTs with well-defined thickness that is larger than one-atom. Since faceted zigzag SWNTs represent the pristine ZnO NT structure, zigzag (but not armchair, as it was done in the previous section) configuration should be taken as a reference perfect structure.

Based on the theorem about the dislocation representation, an arbitrary (n, m) SWNT, formed by rolling up a sheet of atoms, ordered in hexagonal pattern, into a tube, can be viewed as a dislocated zigzag tube with a corresponding Burgers vector. According to the proposed by Ding et al. representation [6], any C SWNT with conventional indices (n, m) corresponds to a zigzag $(n+m/2, 0)$ with an axial screw dislocation

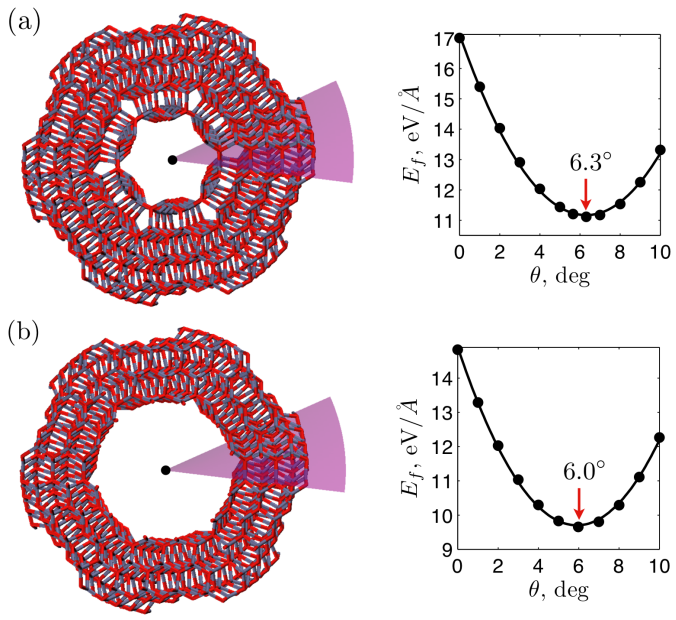

Figure 5.7: Atomistic representations of the relaxed configurations (left) and graphs of the formation energy versus the twist angle (right) for (a) $\{5,1\}_{3b}$ and (b) $\{5,2\}_{3b}$ ZnO NTs with optimal angles of 6.3° and 6.0°, respectively. Zn and O atoms are shown in gray and red, respectively. The outer radius is $R = 14.7$ Å. The purple plane is the cut made to create the dislocation. Note the intrinsic twist.

of Burgers vector $b_\gamma = m(-1/2, 1)$ for an even m, and $(n + m/2 + 1/2,\ 0)$ tube with a screw component $b_\gamma = m(-1/2, 1)$ and a small edge component $b_\perp = (-1/2, 0)$ for an odd m. This idea is visualized in Figure 2.8. Therefore, the glide with Burgers vector $\mathbf{b}_z = k(-\mathbf{a}_1 + 2\mathbf{a}_2)$ of a perfect zigzag tube $(n, 0)$ leads to $k(-1, +2)$ change in wrapping indexes or $(n - k, 2k)$ tube, where k is an integer number, $\mathbf{a}_1$ and $\mathbf{a}_2$ are the lattice vectors of a flat honeycomb structure, depicted in Fig 5.1. Hence, screw dislocated ZnO NT denoted by $\{L, h\}_{kb}$ can be described similarly by a set of faceted $(6l - 3 - k, 2k)$ SWNTs, where l runs from $h + 1$ to L, as shown in Table 5.2. Each $(6l - 3 - k, 2k)$ SWNT is characterized by the helical symmetry with twist angle θ_s and axial translation T_s that can be found from the evaluated axial and circumferential components of

the screw vector $\mathbf{b}_z$ as

$$\theta_s = \frac{2\pi k}{3(2l-1)^2 + k^2}, \qquad T_s = \frac{\sqrt{3}T(2l-1)}{\sqrt{3(2l-1)^2 + k^2}}. \tag{5.8}$$

Note that for NT with $n^{'} = 1$ the simulation cell is given by a dislocated strip of atoms that represents a translation domain of pristine NT, and hence, the whole structure can be constructed by applying helical operation to the defined unit cell. However for some specific values of k, when $n^{'} > 1$, angular symmetry of the NT can be accounted, which leads to additional reduction in the simulation cell size. In the case of $\{L, h\}_b$ NT ($k = 1$) each SWNT undergoes the glide step of Burgers vector b and has common $\theta_2 = \pi$ angular symmetry, which causes two times reduction in the domain size, together with different helical parameters for a screw-dislocated strip of atoms that lead to some common values $\bar{\theta_s}$ and $\bar{T_s}$ for a whole NT unit cell. However $\{L, 0\}_{kb}$ NW cannot be represented by a set of screw-dislocated SWNTs since it contains the dislocation core, where the glide step becomes a fraction of the Burgers vector magnitude. This results in lose of the angular symmetry, and hence, larger simulation domain for NWs.

5.2.2 Comparison between atomistic results and continuum modeling

The ZnO wurtzite crystal presents a hexagonal lattice with parameters $a = 3.23$ Å and $c = 5.32$ Å along the basal plane and the vertical axis, respectively, see Fig. 3.4(a). Here we studied ZnO NTs and NWs with translational periodicity $\sim c$ (precise value was found by conjugate gradient energy minimizations) along the [0001] direction and bounded by six non-polar $\{10\bar{1}0\}$ surfaces, which are the most stable surfaces in ZnO. In comparison with other surfaces, the ZnO dimers located on $\{10\bar{1}0\}$ are known to exhibit significant relaxation [121] but not reconstruction. We focused on ultrathin structures since in this size limit any potential deviations from Eshelby model are maximal. In NWs, the number of layers L in the cross-section was varied from 2 to 6. There are two ways to define R, as Ld_{100} where $d_{100} = \sqrt{3}a/2$ is the distance between $(10\bar{1}0)$ planes, or as $(4L-1)d_{110}/2$, where $d_{110} = a/2$ is the distance between $(11\bar{2}0)$ planes, where a is evaluated from the relaxed pristine configurations. We took R as the averaged values obtained with these two approaches. Then R ranged from 5.5 Å to 17.7 Å. In NTs with $h = 1, ..., L-2$ the inner radius r was defined in an analogous manner with R. Then

r ranged from 2.6 Å to 11.8 Å. In all these structures we introduce screw dislocations with the axis located at the center or ξ distance apart from it and with the minimal Burgers vectors $b = 5.4$ Å in NWs and larger (multiple of b) in NTs. For this, we used the morphologies of the pristine relaxed structures. Starting from the dislocation axis location, the atoms in the vicinity of the cut-plane were gradually displaced along this axis until atomic displacements equal to the magnitude of the desired Burgers vector were reached and maintained up to the surface atoms. Note that the chosen location of the dislocation axis is not crossing any atomic site.

The energetics of the pristine NWs and NTs was analyzed using a standard Wulff decomposition of the formation energy E_f, measured per unit length, approach. E_f is defined as difference between the total and bulk energies. The functional form [89] of E_f contains bulk strain energy correction, that captures the elastic strain stored in the NW or NT walls, surface, and edge energy terms. By fitting it to our DFTB data, we determined that the last two components can be neglected, in agreement with what was previously found in hexagonal Si NW [58]. Thus, E_f contains only the surface energy term $2\pi\gamma(R + r)$, with a surface energy value $\gamma = 64.3\,\mathrm{meV}/\mathring{A}^2$. It is worth to note that γ compares well with the DFTB value of $63.2\,\mathrm{meV}/\mathring{A}^2$ and the *ab-initio* value of $72.4\,\mathrm{meV}/\mathring{A}^2$ [122] for the $(10\bar{1}0)$ surface of bulk ZnO.

As in experiment [113], we explored screw dislocations with Burgers vectors **b** of the minimum allowable length c and triple that magnitude, as a model for a super-screw dislocation. To rationalize the NW core-surface interaction, we considered the location of the dislocation core at the NW center as well as at a distance ξ away. One immediately recognizes that E_f contains two terms: a surface energy and a strain energy of the dislocation E_d term. Since the dislocations do not change the surface energy, E_d is obtained by subtracting E_f of the pristine structure from the dislocated one. The E_d term will be addressed next.

We first discuss dislocated ultrathin NWs. It is reasonable to expect that due to the close vicinity of surfaces, NWs would eject the dislocation to revert to the pristine structure. However, there is convincing evidence that they remain stable [113, 45, 44]. We directly probed the stability of the screw-dislocated NWs and the role of twisting by carrying out two separate constant energy MD simulations under both PBC and stress-free OBC. A number of 108 atoms located in the primitive cell of a $\{3, 0\}_b$ were evolved

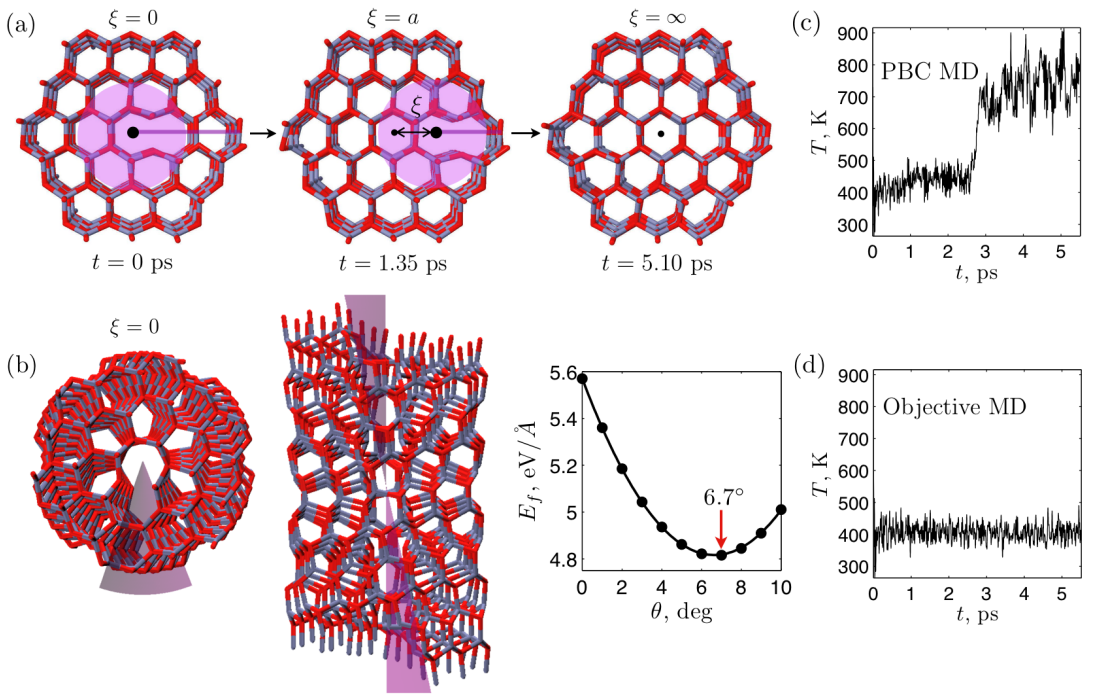

Figure 5.8: (a) Snapshots from PBC MD simulations of a untwisted $\{3,0\}_b$ ZnO NW, where the hatched area depicts the dislocation core region. (b) Axial (left) and side (central) views of the relaxed $\{3,0\}_b$ ZnO NW under objective boundary conditions and graph of the formation energy versus the twist angle (right). The plots of temperature time dependence for MD simulations under (c) PBC and (d) OBC for $\{3,0\}_b$ ZnO NW.

in time for 5.5 ps with a time step of 1 fs. Although the initial temperature was in both cases $T = 400$ K, the two simulations led to very different outcomes. On the one hand, in the PBC MD solution, the screw dislocation is gradually ejected from the untwisted NW, Fig. 5.8(a), until the lowest-energy defect-free structure is regained. The dynamics of this process is reflected in the dramatic increase in instantaneous T in Fig. 5.8(c), that signifies a lowering of the potential energy. On the other hand, the objective MD solution retains the dislocation axis at the central location of the twisted by 6.7° or, equivalently, 1.26°/Å NW equilibrium structure, shown in Fig. 5.8(b). Figure 5.8(d) displays this dynamical process with usual equilibrium T fluctuations.

The contrasting dynamical behavior observed above is further supported by the

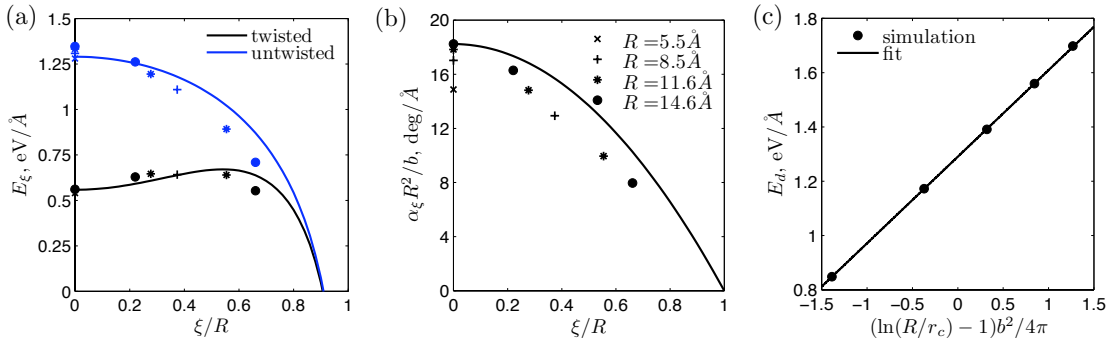

Figure 5.9: The graphs of the (a) shifted strain energy E_ξ for twisted and untwisted ZnO NWs and (b) rescaled twist rate versus the dislocation line position. (c) The plot of the simulation data fitting for $\xi = 0$ case that gives $G = 0.32$ eV/Å^3 for shear modulus and $E_c = 1.29$ eV/Å for core energy. Here the simulation results and continuum predictions are represented by symbols and solid lines respectively.

dislocation energy data for a collection of $\{L, 0\}_b$ NWs when the core is situated at different ξ locations. In Fig. 5.9(a) it can be seen that when the twist is neglected (as under PBC), the axis ($\xi = 0$) location is unstable. When the intrinsic twist effect is considered by the objective boundary conditions, the $\xi = 0$ location becomes stable. Only when it is displaced about half-way to the surface, the dislocation can be ejected. The rescaled intrinsic twist rate dependence on ξ/R is summarized in Fig. 5.9(b).

We note that objective MD ability to accurately account for the small intrinsic twist enables the understanding the stability of these NWs. From a different perspective, our microscopic findings are in excellent agreement with the elastic theory predictions: a dislocation is stable at the center of a cylinder with stress-free surfaces only when it is allowed to undergo an Eshelby twist [40]. E_d (per unit length) produced by an axial screw dislocation in a cylindrical rod ($r = 0$) of radius R writes as

$$E_d = E_c + \frac{Gb^2}{4\pi}\left[\ln\frac{R}{r_c} + \ln\left(1-\frac{\xi^2}{R^2}\right) - \left(1-\frac{\xi^2}{R^2}\right)^2\right]. \tag{5.9}$$

Here E_c and r_c represent the non-classical core energy (per unit length) and the core size of the dislocation while G is the shear modulus. The first two terms in brackets are caused by the screw dislocation elastic strain field, while the last term captures the

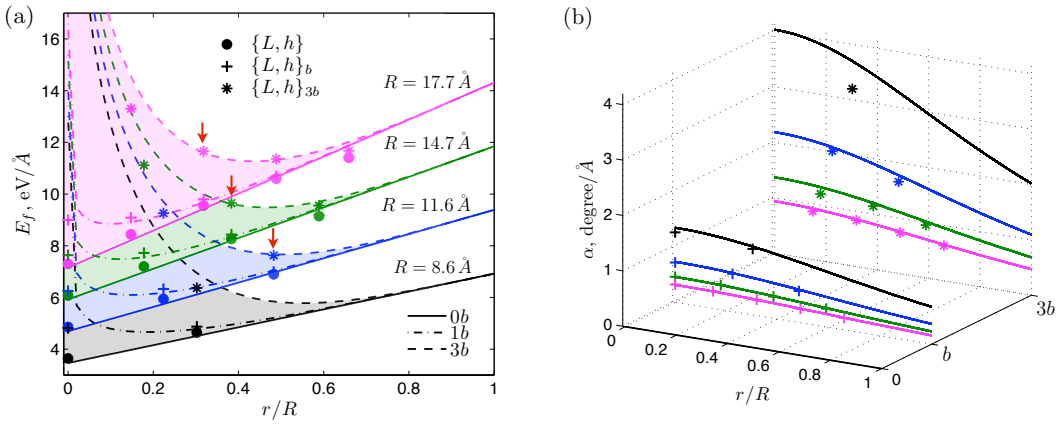

Figure 5.10: (color) (a) Formation energy and (b) intrinsic twist rate for ZnO NTs with different Burgers vector magnitudes, $0b$ (pristine structures), $1b$, and $3b$, versus the ration r/R. NTs with equal outer radii R are shown in the same color. Lines correspond to eqs. (5.11) and (5.12) and symbols are the simulation data. Arrows indicate the "magic" twisted NT structures.

energy gained by acquiring the twist rate

$$\alpha_\xi = \frac{b}{\pi R^2}(1 - \frac{\xi^2}{R^2}). \tag{5.10}$$

Of course, this continuum treatment cannot be applied within the dislocation core region characterized by high lattice distortions. Nevertheless, both r_c and E_c can be determine from the objective MD data [119, 34]. We determined r_c by comparing the relaxed configuration and the structure generated by displacing atoms according to continuum strain field of a dislocation. Defining the dislocation core by the region with the highest (greater than $0.4\mathring{A}$) relative displacements between these two configurations, we obtained $r_c = 2a/\sqrt{3} = 3.73\ \mathring{A}$, as also depicted by the hatched areas in Fig. 5.8(a). By fitting eq. (5.9) to our data with $\zeta = 0$, see Fig. 5.9(c), we obtained $E_c = 1.29\,\mathrm{eV}/\mathring{A}$ and $G = 51$ GPa, which is in good agreement with the bulk value of 44 GPa [123]. For a comprehensive comparison, we plot in Fig. 5.9(a) and (b) shifted strain energy E_ξ, where the R-dependence is eliminated by subtracting $(Gb^2/4\pi)\ln(R/r_c)$ term from eq. (5.9), and rescaled twist rate versus the dislocation line position. The surprisingly

good agreement between our atomistic data and continuum predictions brings the fortunate conclusion that Eshelby's theory remains valid even with regard to ultrathin screw-dislocated ZnO NWs.

We now discuss dislocated NTs. The above finding allows us to quantify with confidence E_d and the stabilizing twist rate. When $r > r_c$, i.e. when $h \geq 2$

$$E_f = 2\pi\gamma R(1 + \frac{r}{R}) + \frac{Gk^2b^2}{4\pi}\left[\ln\frac{R}{r} - \frac{1 - r^2/R^2}{1 + r^2/R^2}\right], \tag{5.11}$$

and

$$\alpha = \frac{kb}{\pi R^2}\frac{1}{1 + r^2/R^2}. \tag{5.12}$$

Indeed, Fig. 5.10(a) and (b), showing the formation energy and twist rate for ZnO NTs as functions of r/R for different R, demonstrate a good agreement between the simulation data (symbols) and the curves given by the continuum model in eqs. (5.11) and (5.12). Recall that in pristine NTs, E_f contains only the surface term, in dislocated NTs E_f contains also E_d captured by the second term in eq. (5.11). Hence, at constant R, the differences between the dislocated and pristine curves in Fig. 5.10(a), are attributed to E_d. For the super screw dislocation, the interplay between the surface and dislocation strain energies delineates a local minimum. The closest discrete realization corresponds to a favorable NT with a well defined wall thickness (see down arrows in Fig. 3(a)). This kind of argument should be relevant to the observed NTs [3, 103] since the continuum theory is readily applicable at larger sizes. However, for the NTs with minimal Burgers vector we find no thermodynamic minima with $r > r_c$. As in pristine NTs, E_f is dominated by the inner surface energy term. Since $E_c < 2\pi r_c\gamma$, $\{L, 0\}_b$ NWs appear to be more favorable than $\{L, h\}_b$ NTs. When $r < r_c$, our predictive framework no longer holds as the continuum leads to divergences, Fig. 5.10(a). To gain insight into this small region, we make recourse solely to our DFTB direct calculations which obtained $\{L, 0\}_b$ NWs slightly more stable than corresponding $\{L, 1\}_b$ NTs.

5.2.3 Electronic properties of axial screw dislocations

Modulating the electronic structure of semiconducting NWs and NTs presents great importance for device applications, as these structures have been proposed as important components in electronic and optoelectronic nanodevices. To achieve this goal, several

possibilities are investigated including change in quantum confinement by diameter variations and orientation [116, 124], doping with impurities [125], and surface doping [126]. Uniaxial and biaxial strain variations were also shown to significantly affect the electronic properties of semiconducting nanowires and nanoribbons [127, 128]. Along this latter line of research, here we identify a new way to influence the electronic band structure at the nanoscale, via the high strain generated at the core of an axial screw dislocation. The effect is demonstrated in calculations performed on ZnO, an important semiconducting nanomaterial, that already found many applications including photonics [129] and solar energy conversion [25]. Classical investigations of dislocations in bulk [130, 131] were conducted mainly from the perspectives of the dislocation-induced gap states and band bending of the bulk due to the presence of such states. Here we pursue an investigation from a microscopic and nanoscale level viewpoint and propose a new utility.

The dislocation core, which cannot be treated with the linear elasticity, is the highly distorted central region close to the dislocation axis. The deformation outside the core is less dramatic and linear elasticity works very well. This fact was confirmed for ZnO NW and NT structures in the study [35] described in the previous section. In the center of the relaxed ZnO NWs we identified broken Zn-O bonds and new homo-elemental Zn-Zn and O-O interactions. For instance, in the DFTB relaxed screw-dislocated $\{3,0\}_b$ ZnO NW, the length of originally connected 2.0 Å axial Zn-O bonds became 3.3 Å long. The smallest distances between Zn-Zn and O-O atoms in the core region are 2.8 Å and 2.7 Å, respectively. Note that even the open-core NTs can contain Zn-Zn and O-O atom pairs at these distances when the Burgers vector is large enough, such as in the $\{6,1\}_{3b}$ case. In the DFTB relaxed pristine NW, these Zn-Zn and O-O distances measure 3.28 Å.

We now examine the consequences of the screw dislocation on the electronic properties, focusing on the fundamental band gap, Fig. 5.11. All pristine NWs and NTs present direct band gaps with values consistent with the values in bulk material. The results summarized in Fig. 5.11(a) evidence considerable downshifts in the band gaps of screw-dislocated ZnO NWs, which persist at all considered diameters. Extrapolation of the obtained monotonic dependence suggests that these differences are well maintained at larger L. In ZnO NTs, the band gap shifts are correlated with the wall thickness and size of the Burgers vector, Fig. 5.11(b), and are more significant in thick $\{L,h\}$ NTs

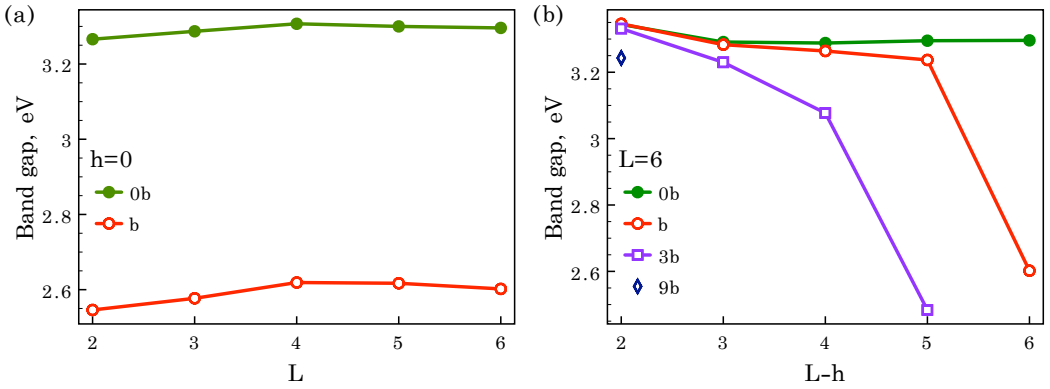

Figure 5.11: DFTB band gap variations (a) with number of layers L in stress free pristine and screw dislocated ZnO NWs and (b) wall thickness, as measured by L-h, and Burgers vector size, in $\{6, h\}_{kb}$ ZnO NTs.

with large Burgers vector. Unlike in carbon NTs [132], here we observe that the shear strain stored in the ZnO NT walls modifies the band gap very little.

More insight about this notable behavior can be gained by inspecting the band structures displayed in Fig. 5.12. Responsible for the band gap decreases are the new gap states developed in the screw dislocated NWs and NTs, see the dashed line in Fig. 5.12(a) and (c). As the number of atoms per cell in the screw dislocated and pristine counterpart structures is the same, the gap states cannot be related to an extra number of electrons. An important observation is that the screw-dislocated but untwisted structures, Fig. 5.12 (right), already display significant differences with their pristine partners, Fig. 5.12 (left). The further occurrence of the Eshelby twist, Fig. 5.12 (center), modifies the band gap very little in ZnO. However, in the case of $\{3, 1\}$ NT, the hollow core screw dislocation does not bring any new gap states or significant change in the band structures, only the dislocation-induced symmetry lowering effect, manifested in splitting of some degenerate energy levels, can be seen in Fig. 5.12(b). Overall, this analysis suggests that the core of the screw dislocation is the primary cause for the dramatic band gap modifications noted in Fig. 5.11 and not the linear shear strain located outside the core region.

To validate the DFTB predictions, the more accurate DFT calculations of the same

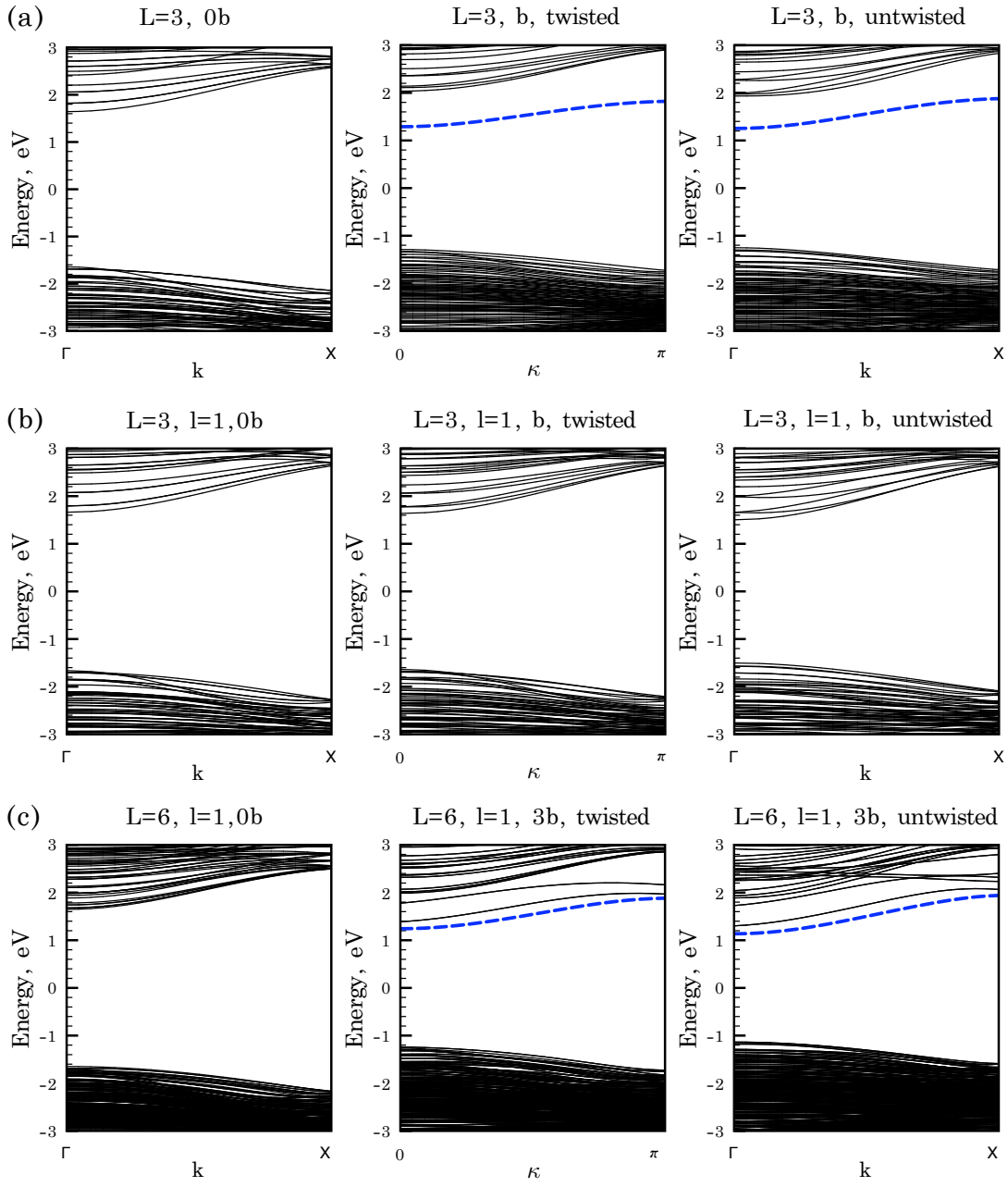

Figure 5.12: DFTB band structures for ZnO pristine (left) and screw-dislocated (center and right) (a) $\{3,0\}$ NW, (b) $\{3,1\}$, and (c) $\{6,1\}$ NTs. Zero energy corresponds to the Fermi level set to the middle of the band gap. Dashed blue lines indicate the gap states developed in the screw dislocated structures.

ZnO structures were performed in [36]. A comparison indicates that all the important features observed with DFTB method, such as the singular band developed in the band gap of screw dislocated ZnO NW, are still present in the DFT results. The effective coupling of the screw dislocation to the electronic states around the Fermi level conduction states is also visible in DFT calculations. Furthermore, the additional plots of spatial wavefunction [36] corresponding to the conduction band minimum evidences that the observed gap states in $\{3,0\}_b$ ZnO NW are due to the new Zn-Zn interactions located in the dislocation core. According to DFTB relaxed configurations, in $\{3,1\}_b$ NT the distances between Zn-Zn atoms do not decrease significantly in comparison with the perfect arraignment of atoms in pristine configuration, while in $\{6,1\}_{3b}$ NT, in spite of the hollow core, the large Burgers vector leads to Zn-Zn interactions. Therefore, the observed band gap modifications in Fig. 5.12 can be related with the presence of highly distorted dislocation core region associated with Zn-Zn interactions.

5.2.4 Summary

In conclusion, using the method of objective MD, we have simulated ultrathin ZnO NWs and NTs with a wurtzite structure containing a screw dislocation and showed that the competition between the lattice strain and surface energy leads to ultrathin chiral NTs made out of nonlayered materials. While accessible in experiment, the characterization of the Burgers vector and atomic structure distortions associated with lattice twisting presents many challenges and sources of errors. At variance with recent experimentation [113], we conclude here that the continuum Eshelby model works very well above a critical size of only a few atomic spacings. This validation opens up the possibility for understanding the stability of a class of nanomaterials [3, 103, 44, 45, 104] with new properties and diverse applications. Our results for equilibrium configurations are in good agreement in all important respects with the recent ZnO NT experiments [3].

Besides, we identified screw-dislocation band gap narrowing, an effect common to ZnO NWs and NTs. By carefully analyzing of the relaxed structures and electronic properties, we traced this effect to the new homo-elemental Zn-Zn interactions created in the screw dislocated ZnO core. This newly identified mechanism act independently from the known quantum confinement effects and should be present in nanostructures with diameters larger than the ones considered here as well as in similar nanostructures

made out of other materials. In ZnO NTs, the band gap appears stable against the shear strain generated by the dislocation in the NT walls. Nevertheless, the band gap modulation effect is still present in thick NTs with large Burgers vectors, due to the same Zn-Zn interactions located in the small open cores.

Chapter 6

Intrinsic twists in graphene nanoribbons

The richness of properties of graphene attracted great interest for nanoelectromechanical and photonics applications [133]. The perfect two-dimensional (2D) graphene sheet has zero-gap and opening a bandgap presents significant practical importance. The possibility of tuning electronic properties through quantum confinement prompted fabrication of graphene nanoribbons (GNRs) [29, 30, 31, 134, 135]. *Ab initio* atomistic simulations obtained that in addition to the GNR's width, an applied mechanical deformation, such as elongation and twist [136], provides another control route over the electronic properties.

The two edges can affect the GNR morphology considerably as they introduce in-plane stress [137, 138]. Wagner et al. [139] obtained that the stress release by out-of-plain relaxations of the OH and SH groups result in rippling of the GNR's edges. Interestingly, Gunlycke et al. [140] found by atomistic simulations that a twisting deformation can release the edge-stress in GNRs with F-saturated edges. Thus, predicting the equilibrium morphologies and electronic properties of GNRs requires a detailed understanding of GNRs out-of-plane deformation mechanics and how it impacts the electronic states.

Our main goal is to build a model based on atomistic data that gives the structural parameters of GNR as a function of its edge chemistry and axial deformation. However, the applicability of continuum models for nanoscale structures still remains an open and

interesting problem. In Section 5.2, where the effect of screw dislocations in nanostructures was investigated, we found that above a critical size of only a few atomic spacings continuum model based on linear elasticity supplemented by a nonlinear core term describes well the energetics of screw-dislocated NTs and NWs of ZnO. To the contrary, in Section 5.1, where single-walled NTs made out of one-atom thin layers of ZnO were considered, the lack of shear strain energy in screw-dislocated NT wall suggested the invalidity of the continuum plate model associated with the monolayer. The breakdown of the plate phenomenology for the out-of-plane deformations of graphene was also mentioned in [112, 141, 142]. For example, the work on bending of graphene [112] revealed that strain energy due to pure bending arises from different sources for multilayer and monolayer graphene. According to atomistic simulations combined with a bond orbital analysis, in multilayer graphene σ-bonds are stretched and compressed in agreement with the plate model, while in monolayer the main source of strain comes from π-orbital misalignment, which leads to inapplicability of the plate phenomenology for monolayer. Moreover, a twisted H-saturated GNR does not store shear but tensile strain [143] and exhibits an inverse Poynting effect [142]. Therefore, in order to predict the morphologies of twisted GNR we propose a new approach based on second-order phase transition model that does not make recourse to the plate idealization.

Relying on atomistic simulations, in this study we identify a gallery of twisted GNRs with bare, F-, and OH-saturated armchair edges. In particular, in F- and OH-GNRs we identify a robust out-of-plane asymmetric edge relaxation mechanism that significantly twists GNRs, especially the very narrow ones, and renders as energetically distinct the left and right-handed chiralities. By contrast, in the bare-edge case, where twist is generated by the in-plain edge stress, GNRs are twisted only above a critical width size. The left and right-handed GNR chiralities are energetically degenerate. In the current work the structural parameters of all these uniformly twisted GNRs are predicted with a phase transition model informed by our DFTB atomistic data, which avoids the difficulties of modeling GNRs as classical mechanical plates.

This Chapter, which describes the work published in [37], is organized as follows. First, the non-standard atomistic method used to carry out the simulations is discussed. Then, the simulation results are presented. Afterwards, the proposed Landau phase transition model, that adequately predicts the most important features observed in

simulations, is illustrated. The next section confirms that twist modifies the bandgap of F- and OH-GNRs via the same ε_{eff} mechanism acting on H-saturated GNRs [143, 142]. Finally, our main results are summarized.

6.1 Methodology

Because torsional deformation alters translational periodicity, atomistic simulations of twisted GNRs are beyond reach for common PBC treatment. The presented calculations were carried out with objective MD [89] coupled with DFTB method [78]. The valence shell basis set used here contains *sp* basis functions for C, O, F and *s* for H. The method, previously used to study the torsional response of carbon nanomaterials [105, 144, 143, 142, 34], is based on the description of an infinitely-long twisted GNR as an objective structure [90], using translations and rotations operations

$$\mathbf{X}_{j,\zeta} = \mathbf{R}^{\zeta}\mathbf{X}_j + \zeta\mathbf{T}. \tag{6.1}$$

Index j runs over the atoms at the positions $\mathbf{X}_j$ inside the objective domain, while index ζ labels various replicas of the domain. The rotational matrix $\mathbf{R}$ of angle θ around the axis delineated by vector $\mathbf{T}$ define the applied helical operations. When $\theta = 0$, the above equation describes a flat GNR with translational periodicity T, which is the modulus of vector $\mathbf{T}$.

Our calculations were carried out on GNRs with armchair edges as in this orientation electronic properties are most sensitive to twist [140, 145]. We characterize the GNR's width in terms of the number of C-C dimer lines, N. As such, the objective simulation domain contains $2N$ C atoms. To enable a comprehensive analysis, our calculations considered a large GNR set, with N varying between 5 and 30.

6.2 Atomistic simulation results

Our initial PBC calculations, i.e. $\theta = 0$ in eq. (6.1), give flat GNR morphologies with translational periodicities slightly larger than in 2D grahene and with bonding characteristics that change abruptly at the edges. As an example calculations, we present in Fig. 6.1 the relaxed configurations obtained for the $N = 14$ GNRs with bare,

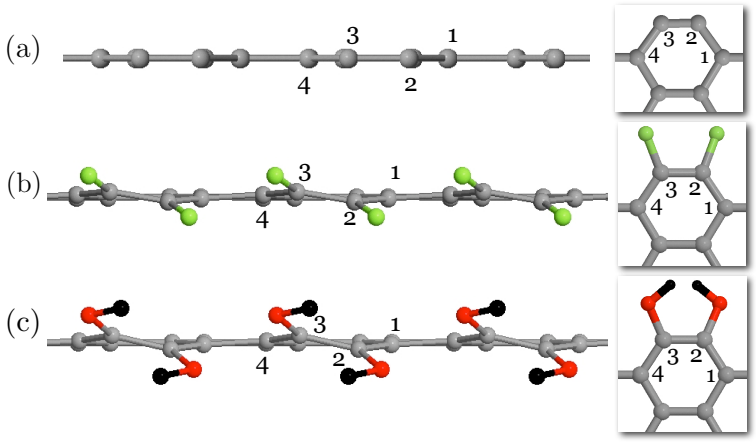

Figure 6.1: Side views of the PBC relaxed $N = 14$ GNRs with (a) bare, (b) F-, and (c) OH-saturated armchair edges. Inserts show top views of the edge atoms. The edge C atoms labeled 1,2,3, and 4 delineate the dihedral angle Ω reported in Table 6.1.

F-, and OH-edges. The relaxed bare-edge GNRs remain flat, as previously obtained for H-saturated GNRs [143]. The C-C bonds situated on the outermost dimer lines (bonds 2-3 in Fig. 6.1) undergo severe compressions, as documented in the first line of Table 6.1. In edge-saturated GNRs, the F and OH groups undergo severe left-right and up-down displacements. The edge distortion is more complex as the outermost C atoms now undergo out-of-plane displacements as well. This can be quantitatively seen in the large positive dihedral angles Ω, as the ones listed in Table 6.1. Note that the edge C-C bonds are still compressed but to a smaller extent in comparison with the bare edges. The axial pre-strains plotted in Fig. 6.2(a) indicates that the next-nearest-neighbor C atoms along the edge dimer lines practically "repel" each other.

Next, energy minimizations enforcing finite θ values obtain energy lowering by twisting for all GNRs but the very narrow bare-edge ones with $N < 11$, Fig. 6.2(b). For a visual comparison the relaxed $N = 14$ GNRs are presented in Fig. 6.3. Structural information concerning these GNRs is listed in Table 6.1. We refer to the angle θ that minimizes the strain energy of the objective cell as the intrinsic twist angle. An important observation is that although the pre-strain values are similar, larger intrinsic angles are introduced by the F and OH-edges, especially in the very narrow GNRs.

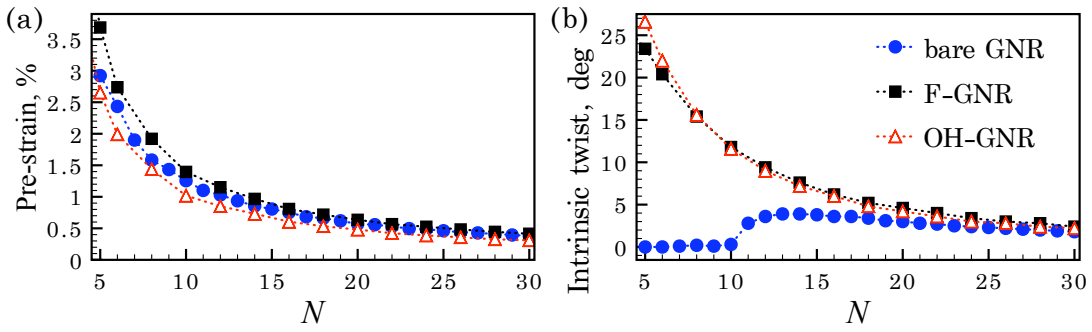

Figure 6.2: (a) Axial pre-strain and (b) intrinsic twist angle as a function of N for GNRs with bare, F-, and OH-saturated armchair edges. In each objective GNR calculation, parameter T was kept at the optimal value found by the PBC calculations.

Focusing on the bare-edge GNR, it is important to note that twist introduces a dihedral angle on the edge bonds, an effect not signaled in the previous works [140, 143]. This observation is important since depending on the twist sign, this angle might be of same or opposite sign to the one introduced by the F and OH-saturation. This means that for the saturated edges cases, the applied twists sign matters as it rotates the bond formed by atoms 3 and 4 in the opposite or same direction with respect to the plane delineated by atoms 1, 2, and 3, to lower or increase Ω. The minima listed in the second lines of each sections of Table 6.1 exhibit smaller Ω values than when untwisted.

Finally, energy minimizations under both T and θ scans found that all GNRs undergo an inverse Poynting effect [142], i.e., when twisted GNRs tend to decrease in length. Combined with an increase in the intrinsic twist angle, these calculations give that the stress-free GNRs store even larger intrinsic twist rates. This behavior, documented for $N = 14$ GNRs in the third lines of each sections of Table 6.1, resembles the previous findings from calculations carried out on H-saturated GNRs [143, 142].

More insight can be gained from Fig. 6.4(a) and Fig. 6.5, which show typical plots of the strain energy as a function of θ for the $N = 14$ GNRs at various strain levels (measured with respect to 2D graphene). Under the same edge conditions and GNR widths, there is a morphology transition controlled by the parameter ε.

Under small axial tension or compression, the energy curves present two energy minima which correspond to twisted GNRs with left- and right-handed chiralities. There

Table 6.1: Structural and energetic comparison of the relaxed $N = 14$ GNRs under different structural parameters T and θ. Here $\varepsilon = (T - T_0)/T_0$ and $\varepsilon_{\text{edge}} = (a - a_{\text{C-C}})/a_{\text{C-C}}$ the bond-edge strain, both measured with respect to the 2D graphene, where a is the length of the 2-3 edge C-C bond shown in Fig. 6.1, $a_{\text{C-C}} = 1.42$ Å, and $T_0 = 3a_{\text{C-C}}$. θ is the twist angle of eq. (6.1) and Ω is the dihedral angle delineated by the edge carbon atoms 1, 2, 3, and 4 shown in Fig. 6.1. The last column lists the energy measured with respect to the PBC relaxation.

Edge	ε (%)	θ	$\varepsilon_{\text{edge}}$ (%)	Ω	E (meV/atom)
bare	ε_0 0.85	0°	-12.15	0°	0
bare	ε_0 0.85	4.0°	-12.09	-3.0°	-0.34
bare	ε_f 0.28	5.8°	-12.06	-4.2°	-0.81
bare	1.2	1.8°	-12.11	-1.2°	0.34
bare	1.4	0°	-12.10	0°	0.88
F	ε_0 0.97	0°	-4.06	18.9°	0
F	ε_0 0.97	7.6°	-3.43	9.4°	-8.66
F	ε_f -0.98	10.4°	-3.37	6.4°	-13.72
F	5.0	1.4°	-3.10	9.4°	37.74
F	7.0	0°	-2.63	2.3°	83.24
OH	ε_0 0.73	0°	-2.15	26.4°	0
OH	ε_0 0.73	7.2°	-1.63	18.6°	-6.55
OH	ε_f -0.96	9.8°	-1.60	16.0°	-9.87
OH	5.0	1.6°	-0.97	20.9°	38.15
OH	7.0	0.8°	-0.45	19.1°	81.02

is a notable contrasting behavior introduced by edges: While the energy for bare-edge GNR is a symmetric function of θ, the F- and OH-GNRs display asymmetric behavior and the left- and right-handed chiralities are distinct. Microscopically, this asymmetry originates in the way twist affects the edge dihedral angle Ω introduced by the F and OH groups. As a vanishing Ω is associated with lowest local strain, a positive (negative) twist applied to the GNR lowers (increases) the initial Ω and thus the strain energy. The morphologies characterized in Table 6.1 have positive twists.

As the axial tension is increased, the intrinsic twist generally decreases. For the bare-edge GNR the flat morphology becomes favorable under only $\varepsilon = 1.4$ %. For the

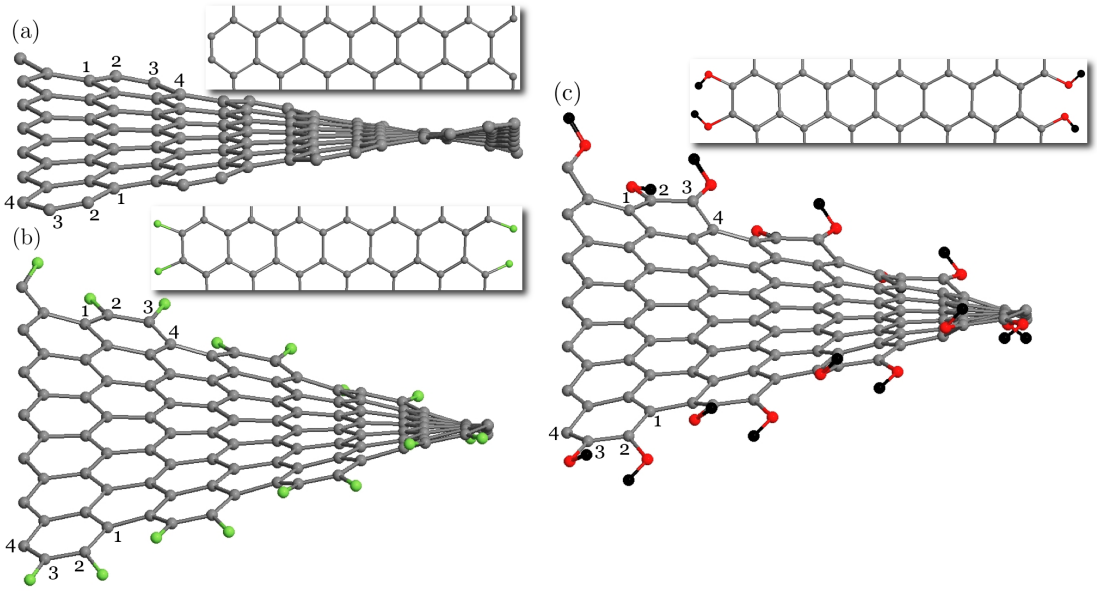

Figure 6.3: Side views of the objective MD relaxed $N = 14$ GNRs with (a) bare, (b) F-, and (c) OH-saturated armchair edges. Inserts show top views of the objective domains used to carry out the simulations.

F- and OH-GNRs, tension suppresses the intrinsic negative twist minima. The intrinsic positive twist is however maintained till larger ε. Under $\varepsilon = 7\%$ the F-GNR already acquired translational periodicity while the OH-GNR is still helical.

6.3 A second-order phase transition model for GNRs

Due to the importance of GNRs for applications, it is desirable to rationalize into a simpler model the complex behavior seen in the atomistic simulations. We propose a unifying model inspired from the celebrated Landau phase transition [146] theory in which the intrinsic twist angle plays the role of a scalar order parameter. θ is zero in the most symmetric flat GNR "phase" but becomes finite in the less symmetric helical GNR "phase".

6.3.1 Graphene nanoribbons with bare edges

Based on microscopic considerations, we now present a model for the strain energy (measured per atom) of bare-edge GNRs. For the case of GNRs with H-saturated edges, where edge stress is released by H atoms, we proposed a microscopic energy model based on discrete summation of each bond contribution [142]. Building on this model, we now write for a flat bare-edge GNRs

$$E = \frac{C\varepsilon^2}{2}\frac{(N-2)}{N} + \frac{C_e(\varepsilon-\varepsilon_e)^2}{N}, \tag{6.2}$$

where C and C_e are the elastic in-plane stiffness of graphene sheet and the edge stiffness, ε and ε_e are axial and edge strains. Thus, we capture the effect of the microscopic repulsive forces at the edges with an in-plane edge stress [137, 140] $\tau_e = C_e\varepsilon_e$. The pre-strain due to the bare-edge is obtained by a minimization procedure as

$$\varepsilon_0 = \frac{2\tau_e/C}{N - 2\Delta C/C}, \tag{6.3}$$

where $\Delta C = C - C_e$. The edge parameters C_e and ε_e are found by fitting to eq. (6.3) our ε_0 versus N data. The obtained curve (solid line), with $C_e/C = 0.41$, where $C = 66$ eV/atom, and $\varepsilon_e = 13.5$ %, together with atomistic data (symbols) are shown in Fig. 6.4(b).

For twisted GNRs, the strain energy has two components

$$E = E_{\rm s} + E_\pi, \tag{6.4}$$

namely the strain energy $E_{\rm s}$ caused by in-plane deformations (tensile or compressive) and an energy term E_π that comes from π-orbital misalignment.

Since in twisted GNRs, the axial bonds at dimer line n undergo additional stretching with strain $\varepsilon_n = \theta^2 d_n^2/2T^2$, where $d_n = (1/2)a_{\text{C-C}}\sqrt{3}(n-(N+1)/2)$ is the distance between n-th dimer and the GNR axis, $E_{\rm s}$ is found by summing over contributions from strained dimers and normalizing by N, and by accounting for the edge stress

$$E_{\rm s} = \frac{C}{2N}\sum_{n=2}^{N-1}(\varepsilon+\varepsilon_n)^2 + \frac{C_e}{N}(\varepsilon+\varepsilon_N-\varepsilon_e)^2. \tag{6.5}$$

Here ε_N is local tensile strain at the edge dimer line N.

Following the previous work [142], E_π is calculated as a difference between hopping integrals of misaligned π-orbitals on the nearest carbon atoms in twisted configuration and parallel π-orbitals in the flat case. The torsional misalignment angles for each of three π-bonds are $\varphi_1 = 2\theta/3$ and $\varphi_2 = \varphi_3 = \theta/3$. Considering small angles of twist θ and taking a Taylor series expansion up to the desired order, we obtain

$$E_\pi = \frac{\sqrt{3}}{3}|V_{pp\pi}|\sum_{i=1}^{3}\left(\frac{\varphi_i^2}{2!} - \frac{\varphi_i^4}{4!}\right) = \frac{\sqrt{3}}{9}|V_{pp\pi}|\theta^2 - \frac{\sqrt{3}}{324}|V_{pp\pi}|\theta^4 = \alpha\theta^2 + \beta\theta^4, \tag{6.6}$$

where $\alpha = \sqrt{3}|V_{pp\pi}|/9$, $\beta = -\sqrt{3}|V_{pp\pi}|/324$, $V_{pp\pi}$ is the interatomic Hamiltonian matrix element. In our model, the $V_{pp\pi} = -2.3$ eV value has been used.

Using eqs. (6.5) and (6.6), and further assuming $\varepsilon \ll 1$ and $\theta^2 \sim \varepsilon$, we obtain

$$E = \mathrm{E}_0(\varepsilon) + \mathrm{E}_2(\varepsilon)\theta^2 + \mathrm{E}_4\theta^4 + O(\varepsilon^3, \varepsilon\theta^4, \varepsilon^2\theta^2), \tag{6.7}$$

where the explicit forms of the Landau theory-like coefficients E_0, E_2, and E_4 are

$$\begin{aligned} \mathrm{E}_0(\varepsilon) &= \frac{C\varepsilon^2}{2}\frac{(N-2)}{N} + \frac{C_e(\varepsilon-\varepsilon_e)^2}{N} + \text{const}, \\ \mathrm{E}_2(\varepsilon) &= \alpha + \frac{C(N^2-1)}{288}\varepsilon - \frac{(N-1)^2}{48N}(\Delta C\varepsilon + \tau_e), \\ \mathrm{E}_4 &= \beta + \frac{C(3N^2-7)(N^2-1)}{135\cdot 2^{11}} - \frac{\Delta C(N-1)^4}{9N\cdot 2^{10}}. \end{aligned} \tag{6.8}$$

The obtained expression (6.7) is invariant to the change in twist angle sign $\theta \to -\theta$.

Fig. 6.4(a) displays the energy predicted analytically as a function of θ. There is a good consistency between atomistic simulations data (symbols) and predictions given by eq. (6.7) (solid lines) over the various ε values, demonstrating the ability of the model to capture the atomistic behavior over a large θ range. The variation of the Landau coefficients with strain is presented in Fig. 6.6(a).

In spite of the somewhat cumbersome expressions for the Landau coefficients, the structure of the energy function (6.7) makes it easy to predict the critical strain ε^* below which twisted states are preferred. As it can be seen in Fig. 6.6(a), E_0 and E_4 have only positive values. Then E_2 has opposite signs for the different symmetries, i.e. positive

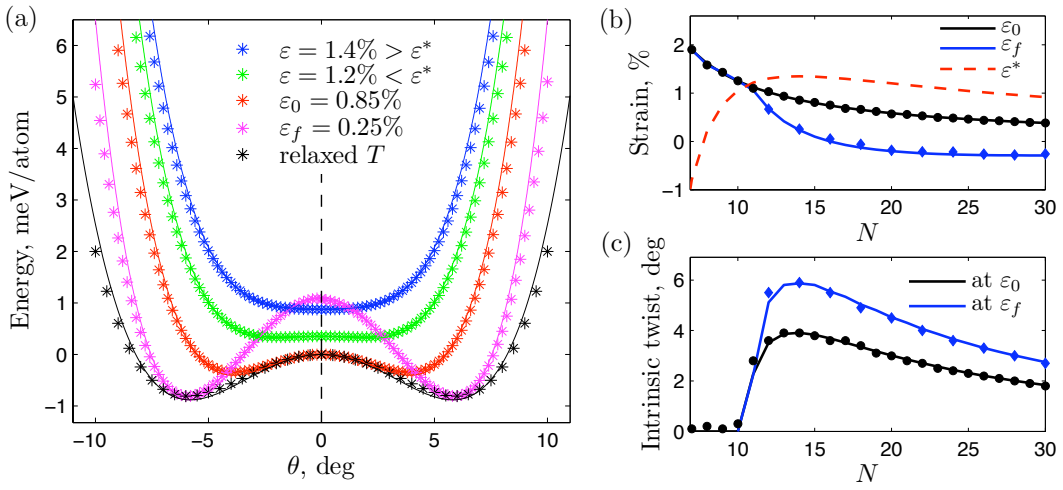

Figure 6.4: (a) Strain energy versus twist angle at different axial strains for bare-edge GNR with N=14. The plots of (b) axial pre-strain ε_0, optimal strain ε_f, critical strain ε^*, and (c) intrinsic twist angle as a function of N for bare-edge GNRs. Symbols denote the simulation data, while solid and dashed lines represent model predictions.

(negative) for more (less) symmetric phase with translation (helical) symmetry. Then transition strain ε^* satisfies $\mathrm{E}_2(\varepsilon^*) = 0$, which gives

$$\varepsilon^* = \frac{\tau_e - 48N\alpha/(N-1)^2}{CN(N+1)/6(N-1) - \Delta C}. \tag{6.9}$$

For the $N = 14$ GNR we obtain $\varepsilon^* = 1.35\%$, in good agreement with the atomistic data of Fig. 6.4(a).

The model captures the unusual morphology change from flat to twist as a function of N specific for bare-edge GNRs and presented earlier in Fig. 6.2(b). The model-simulation agreement can be seen in Fig. 6.4(b), which compares ε^* given by eq. (6.9) with the pre-strain ε_0 of eq. (6.3) generated by the edges. Only for $N \geq 11$, $\varepsilon_0 < \varepsilon^*$ is fulfilled and thus GNRs posses intrinsic twist.

Finally, the model predicts the intrinsic twist values at a given ε as well as the structural parameters of the stress-free GNRs. By minimization of the energy expression (6.7), the intrinsic twist angle at a given strain is found to be $\theta = \sqrt{-\mathrm{E}_2(\varepsilon)/2\mathrm{E}_4}$. After

Table 6.2: Fitting parameters (measured in eV/atom) of energy coefficients for $N = 14$ GNRs with different edge types, where $E_0(\varepsilon) = (a_0\varepsilon+b_0)\varepsilon$, $E_i(\varepsilon) = a_i\varepsilon+b_i$ for $i = 1, .., 4$.

Edge	a_0	b_0	a_1	b_1	a_2	b_2	a_3	b_3	a_4	b_4
F	24.81	-0.49	0.27	-0.045	29.86	-0.70	-	-	-64.79	16.09
OH	22.46	0.33	0.27	-0.053	25.17	-0.42	1.16	0.69	-62.80	10.47

some straightforward algebra, we obtain

$$\theta = \sqrt{c_1\varepsilon + c_2}, \tag{6.10}$$

where

$$\begin{aligned} c_1 &= \frac{\Delta C(N-1)^2 - CN(N^2-1)/6}{96NE_4}, \\ c_2 &= \frac{\tau_e(N-1)^2 - 48N\alpha}{96NE_4}. \end{aligned} \tag{6.11}$$

Similarly, accounting for the inverse Poynting effect, the optimal strain at a given θ is

$$\varepsilon = \varepsilon_0 - \theta^2 \frac{N(N^2-1)/6 - (N-1)^2\Delta C/C}{48(N - 2\Delta C/C)}. \tag{6.12}$$

Substituting formula (6.10) into eq. (6.12), we obtain the strain ε_f as well as twist angle expressions corresponding to the stress-free GNR

$$\varepsilon_f = \frac{2(\tau_e + c_1c_2NE_4)/C}{N - 2\Delta C/C - 2c_1^2NE_4/C}, \tag{6.13}$$

where c_1 and c_2 are the functions of N given in eqs. (6.11). The intrinsic angle at this strain is $\sqrt{-\mathrm{E}_2(\varepsilon_f)/2\mathrm{E}_4}$. The predictive power of this model emerges from Fig. 6.4(b), which compares for all the considered bare-edge GNRs the predicted and atomistically computed ε_f, and Fig. 6.4(c), which compares the θ given by (6.10) at ε_0 and ε_f with the values found in the atomistic simulations.

6.3.2 Graphene nanoribbons with F- and OH-edges

The structure of the energy function (6.7) constructed from microscopic consideration and its predictive power demonstrated for bare-edge GNRs further supports the more

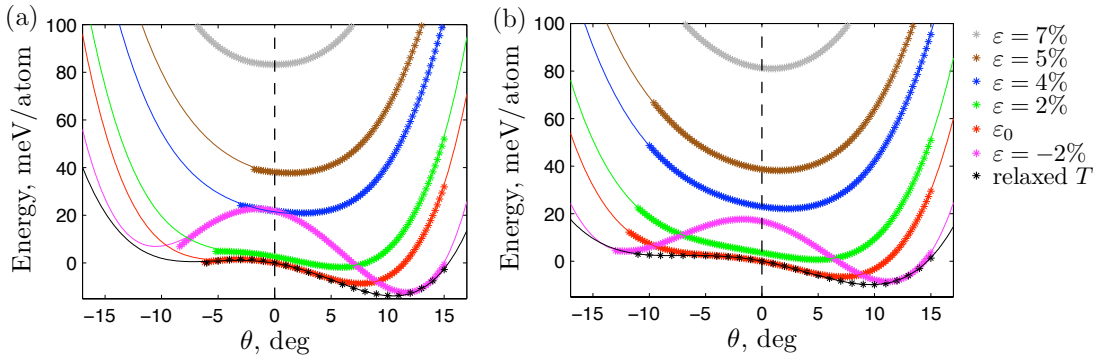

Figure 6.5: Strain energy versus twist angle at different axial strains for (a) F- and (b) OH-GNRs with N=14. Symbols show the simulation results, solid lines denote the fitted with eq. (6.14) data.

pragmatic general approach presented next. We express the total strain energy as a fourth-order polynomial in terms of θ

$$E_{\text{tot}} = E_0 + E_1\theta + E_2\theta^2 + E_3\theta^3 + E_4\theta^4. \tag{6.14}$$

All coefficients are functions of ε. Symmetry considerations help relate the specific effects encapsulated by these terms: The even power terms represent the microscopic bulk, π-orbital misalignment, repulsive edge energies, as already seen in equation (6.7). The odd power terms account instead for the energetics of the out-of-plane edge relaxation, the effect dependent on the twist angle sign.

At a given strain, the Landau coefficients are obtained by directly fitting eq. (6.14) to the atomistic data shown in Fig. 6.5. Thus, all the microscopic effects are now included by numerically fitting to the atomistic data. The energy curves obtained this way are representing very well the atomistic data. Note that data for F-GNRs was fitted without the cubic term since this gives a more accurate behavior of energy as a function of θ. For OH-GNRs, the whole polynomial was used.

The obtained coefficients, plotted in Fig. 6.6, show simple dependences versus the applied axial strain. Thus, they can be fitted to linear and quadratic dependences as summarized in Table 6.2, which further facilitates analytical predictions of the intrinsic twist values. In Fig. 6.6(b) and (c) the fitted points at higher elongations deviate

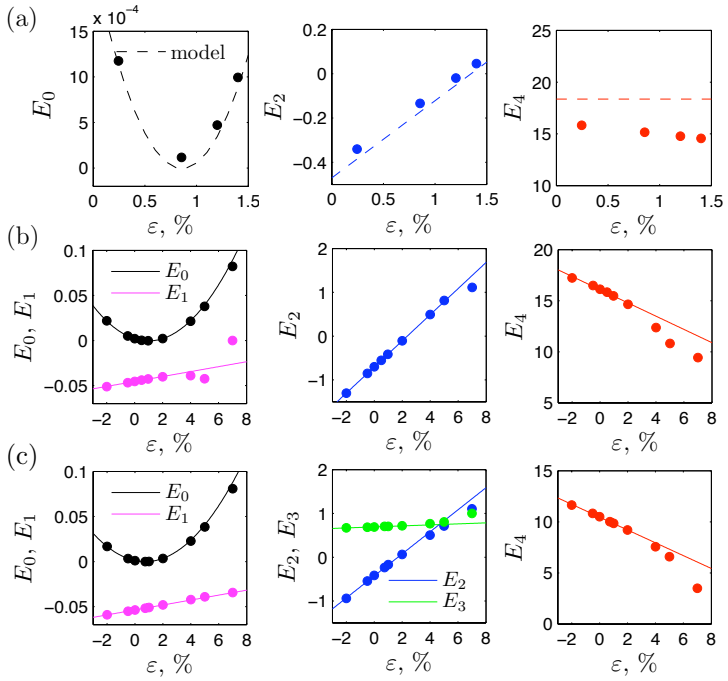

Figure 6.6: The plots of energy coefficients (shown in eV/atom) for (a) bare-edge, (b) F- and (c) OH-GNRs with $N = 14$, where symbols represents fitted to eq. (6.14) values, dashed lines correspond to model predictions given in eq. (6.8) for bare edges and solid lines represent fitted curves (quadric for E_0 and linear for other coefficients) for F- and OH-saturated edges.

noticeably from the fitted curves because of the reduction in the edge distortion. In other words, there is a different edge regime at higher elongations which is not accounted. Fig. 6.6(a) confirms that the earlier microscopic model predictions are close to the fitted coefficients.

Having identified the Landau coefficients, minimizing expression (6.14) gives the order parameter in closed-form. The result is plotted in Fig. 6.7 at various axial strain levels. There is an excellent agreement with the simulated data even at the largest considered strains.

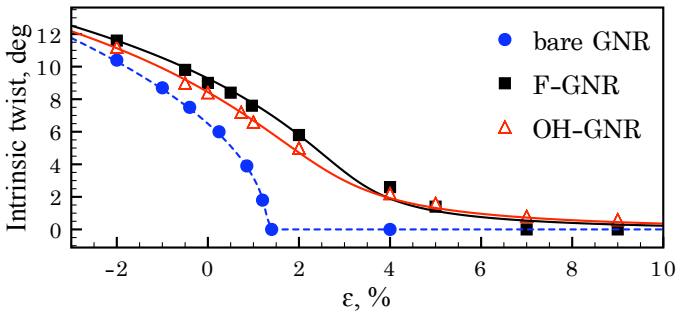

Figure 6.7: Intrinsic twist angle versus ε for $N = 14$ GNRs with bare, F-, and OH-saturated armchair edges. Symbols and lines denote the atomistic results and the model predictions (eq. (6.10) in the case of bare edges), respectively.

6.4 Electronic properties of F- and OH-saturated GNRs

According to the previous study [143], GNR's electromechanical properties can be understood in an intuitive way with an effective tensile strain concept ε_{eff}, defined microscopically as the average axial strain across GNR, that also allows linking the GNR response to those of carbon NTs, which is well understood [132]. It was found [143] that twisted H-saturated GNRs with armchair (zigzag) edges behave as zigzag (armchair) carbon NTs in tension. In agreement with these predictions, *ab initio* calculations [145] demonstrated that the bandgap of GNRs with zigzag edges are insensitive to twist. On the contrary, atomistic simulations showed that twisting GNRs with armchair edges result in bandgap changes [140, 143]. That is why GNRs with more sensitive armchair edges are considered here.

We confirm that twist alters the fundamental bandgap of F- and OH-GNRs. We focused our study on $N = 14$ and $N = 30$ GNRs which were twisted in both positive and negative directions. Twist was applied in two manners, by varying θ while fixing the parameter T at the values found in the PBC calculations (i.e., with GNRs storing a ε_0 pre-strain) and by varying θ and relaxing T.

The bandgaps as a function of θ as well as an effective strain scalar are presented in Fig. 6.8(a) and (b). Large bandgap variations with θ are seen only in the fixed T calculations, a result resembling the previous findings on twisted H-saturated GNRs [143, 142].

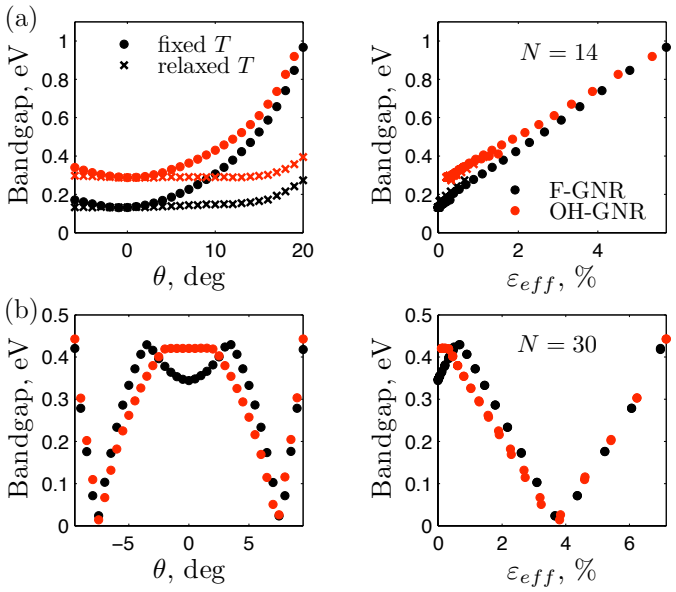

Figure 6.8: Bandgap versus θ (left) and ε_{eff} (right) for F- and OH-GNRs with (a) $N = 14$ and (b) $N = 30$ under fixed and relaxed magnitude of axial vector $\mathbf{T}$.

There, we found that in spite of the inhomogeneous local tension strain created in the twisted GNRs, the bandgap changes are simply proportional with ε_{eff}. When T is relaxed, ε_{eff} and thus the bandgap variations are small.

As in Refs. [143, 142], in Fig. 6.8 we see that in all cases, the quadratic band-gap variations with θ rescale into linear variations with ε^{eff}. Moreover, the curves for the F- and OH-GNRs practically overlap in the ε_{eff} space. This means that the bandgap of F- and OH-saturated GNRs varies to twisting due to the effect of ε_{eff} on the electronic structure near the Fermi level.

6.5 Summary

Using the technique of objective MD based on DFTB potentials, we identified bare-edge, F-, and OH-GNRs that are twisted or flat, depending on their axial strain. Understanding the F- and OH-GNR morphologies is important as twist leads to bandgap changes via the effective strain mechanism identified before for H-saturated GNRs [143]. We

established a basis for systematically predicting these structures starting from GNR's energy, which takes the form of a fourth-order polynomial in the twist angle. The proposed phase transition model can be parameterized in a similar manner, to predict the twisted GNR morphologies with other chemical edge functionalizations observed in experiment [134]. The power and simplicity of the model could make it an attractive tool in the designing of nanoelectromechanical devices based on GNRs. In conjunction with objective MD simulations, our modeling concept could be applied to predict bent GNRs as well, with the bending angle [112] playing the role of the order parameter.

For GNRs with bare edges, the energy function derived microscopically, is invariant with respect to the $\theta \rightarrow -\theta$ change and thus contains only even powers. Under an axial strain, these GNRs undergo a continuous second-order transitions from a twisted (helical symmetry) to a flat (translational symmetry) morphology. The twisted bare-edge GNRs appear to be delicate, as twist angles are small and transition to a flattened structure can be promoted even by a decrease in GNR's width.

Homochirality is commonly encountered in biological macro-molecules such as DNA and proteins. In GNRs with F- and OH-edges, we find that the out-of-plane edge distortion introduces a discrimination between positive and negative twist. This additional effect, captured in additional linear and cubic terms into the energy expression, augments the intrinsic twist value, lowers the energy more significant, and introduces a preferential handedness. The twisted phase is stable against the decrease in GNRs width and much larger external strains are now needed to flatten the GNR structure.

Chapter 7

Conclusion

As the current interest shifts from bulk to nanostructures, which dimensions bring new effects and interesting phenomena not covered with classical continuum mechanics methods, new investigation approaches are needed in order to make progress in this area. This thesis is devoted to the study of mechanical and electronic properties of nanoscale structures by using atomistic simulation methods together with continuum model approaches. Mostly the dissertation focuses on the role of dislocations, defined as line defects, in nanostructures. Finite-size and edge effects in monolayer materials are investigated as well. Current Chapter includes a summary of the main results and specific significance of the presented research.

Firstly, we studied the dislocation processes in carbon nano-onion. The experimentally observed inwards dynamics of dislocations in carbon nano-onions contradicts the current knowledge that dislocations are attracted by free surfaces. Atomistic calculations, based on classical MD approach with REBO potential, carried out on idealized carbon nano-onions combined with rigorous energy analysis clearly revealed the origin of the inward driving force [33]. The dominance of inward over outward glide route was attributed to the reduction in the edge energy component or, equivalently, in the number of dangling bonds with each inward glide step, an effect specic to the spherical topology. This finding has important implications. First, because of their spherical shape carbon nano-onions are researched for tribological applications in extreme environments such as radiation and vacuum. Amongst the different carbon materials nano-onions and multiwalled nanotubes demonstrate the best vacuum tribological performances which

is attributed to rearrangements of the irradiated structures via linking of neighboring graphene shells or migrations of dislocation [147]. Therefore, the identified mechanics of spiroid-to-onion transformation can be used to explain the dislocation migration processes which result in the unzipping and re-zipping of neighboring graphene layers. Second, the transport of carbon atoms in graphitic lattices is also of great importance. The uncovered inwards glide appears as an easier route to transport atoms through the dislocation line, and could shed light on the growth mechanism of carbon nano-onions. Besides, such inward glide motion of the outer edge can provide a route for the transfer or trapping different types of molecules inside of the nano-onion.

Secondly, we investigated the effects of screw dislocations in quasi-one-dimentional ZnO NTs and NWs. Helical SWNTs of ZnO described with density-functional based TB model [34] were considered first. The employed objective MD computational framework, that accounts for helical instead of translational symmetry, allowed for simulating chiral SWNTs represented by screw-dislocated achiral structures. At large diameters (greater than 2 nm), by comparing the microscopic strain stored in the tube wall with the continuum predictions, we observed the invalidity of the continuum plate idealization for the one-atom thick layer. However, the continuum membrane without thickness model can be assumed for the monolayer, since no shear energy cost is associated with creation of an axial screw dislocation with an arbitrary Burgers vector magnitude in SWNT. At small diameters (less than 2 nm), comparing the computed Eshelby twist executed by the one-atom thick layers with the one predicted by pure rolling, we found that a large catalog of SWNTs store intrinsic twists. This unusual intrinsic twist effect is shown to be dependent on chirality and diameter, as a part of the general trend to depart from the standard rolled-up construction. Therefore, the rolled-up predictions for the SWNT translational periodicity, that are usually used for numerical studies of chiral NTs under PBC, should be considered with care. In addition, it was demonstrated that the electronic structure of ZnO SWNTs becomes sensitive to curvature at small diameters, while chirality effects are negligible, except for very small structures.

Next, we studied thick NTs and NWs of ZnO containing axial screw dislocations which were recently synthesized by screw-dislocation growth mechanism [3]. We showed theoretically that once their diameter increases above a critical size of the order of a few atomic spacings, the existence of these structures can be rationalized in terms of

the energetics of surfaces and veritable Eshelby's twist linear elasticity mechanics supplemented by a nonlinear core term [35]. For Burgers vector larger than the minimum allowed one, a twisted NT with well-defined thickness, rather than a NW, is the most stable structure. Results are assistive for designing ultra thin nanostructures made out of nonlayered materials. Besides, the role of the presence of axial screw dislocations in helical ZnO NWs and NTs was investigated in relation to their electronic properties [36]. Relying on objective MD coupled to DFTB simulation method, we concluded that the highly distorted dislocation core is responsible for change of the band gap values. The observed band gap dependences on the size of the Burgers vector and wall thickness could motivate new strategies for growing via screw dislocation mechanism stable nanostructures with desired band gaps.

Because screw dislocation driven growth is catalyst free, nowadays it attracts more attention in the area of nanoscale structures synthesis as a less demanding, scalable, and low-cost alternative growth method. Recently NW and NTs made out of other materials, such as PbS [44], PbSe [45], GaN [148], In_2O_3 [149], InP [113], Cu_2O [150], CdS and CdSe [151], were grown experimentally via this screw dislocation mechanics. However, the structural stability and properties of screw-dislocated nanostructures remain relatively unexplored with standard computational methods at the atomic level. The lack of simulations in this area is related to the fact that standard atomistic approaches based on periodic boundary conditions can not handle structures possessing helical symmetry that naturally presented in screw-dislocated configurations. In the current work this problem was overcome by treating objective instead periodic boundary conditions. The successful application of the objective MD method for investigation of the mechanical and electronic properties of screw-dislocated ZnO NWs and NTs was demonstrated in Chapter 5. Similarly, this method can be used to study dislocated NWs and NTs made out of other materials.

To apply the objective methodology to other materials, more work is needed to improve the existing DFTB MD methodology describing the interatomic interactions more precisely. Most importantly, electrostatic atomic charges interactions need to be included in a self-consistent manner. In other words, the objective boundary conditions could be implemented in the well-tested self-consistent charge (SCC) DFTB

scheme [152]. The SCC DFTB methodology accounts for delicate charge balance between different atoms represented by an additional term in Hamiltonian operator that becomes important in heteronuclear molecules and in polar semiconductors. In summary, the updated objective SCC DFTB MD method with more accurate description of the chemical binding could be used to model efficiently more complicated systems such as structures containing polar surfaces and even biological systems having helical and angular symmetries.

Thirdly, using the same objective MD coupled with DFTB framework, we also studied the role of torsional deformation in stabilization of one-atom thick GNRs with bare, F- and OH-saturated armchair edges [37]. In the case of bare-edges the critical size GNR with $N = 10$ was identified, such that for larger ribbons the ground state is twisted structure, while for smaller ones flat configuration is more favorable. This finding implies that bare-edges GNRs undergo the second-order phase transition, where symmetry changes from translation to helical. A simple phenomenological model based on atomistic simulation data was proposed for this continuous phase transition. As a result of calculations, twist deformation was found to stabilize the edge stresses produced by the presence of F- and OH-saturated edges for all GNR sizes. However, the relaxation is more complex than for bare-edges with severe left-right and up-down displacements of F and OH groups, as well as out-of-plane displacements of the outermost C atoms, that leads to asymmetric response on twist deformations. To capture these effects the proposed phase transition model employs more general form of energy with fitted coefficients, which are functions of the applied axial strain. Moreover, the band gap variations with twist via the effective strain mechanism, previously introduced for H-GNRs [143], were identified for F- and OH-GNRs. Our results indicate that finite-size and edge effects should be attentively considered when designing new nanoelectronic devices based on GNRs.

Likewise, the developed phase transition model can be parametrized and used to predict the twisted GNR morphologies with other chemical edge functionalizations observed in experiments. Besides, similar approach based on the continuous phase transition could be used to describe the intrinsic bending of GNRs with different edge saturations, an effect also attributed to the edge stress. In that case the bending angle will play the role of the order parameter.

The edge types and functional groups saturating the edges significantly influence the properties of GNRs, as was confirmed in Chapter 6. For instance, for bare-GNRs the edge structure may require more sophisticated methods to model them. In order to properly describe GNRs with zigzag, where spin effects are found to be significant [153], instead of considered in this work armchair edges more complicated methods should be used. This is because of the fact that in armchair edge the stable triple bond is formed between the outermost carbon atoms while in zigzag case the electrons from unsaturated edge carbon atoms can not be efficiently shared and edge appears to be metastable, i.e. it is reconstructing spontaneously at high temperature. The accuracy of the simulation method is an important issue since its results are intended to be used for predicting the properties of the system in question and motivate more expensive experimental studies. The Coulomb interaction may also become important in GNRs with various edge morphologies, and hence, more accurate SCC DFTB method enhanced with objective boundary conditions could be further used to study the mechanical and electronic properties of GNRs.

References

[1] J. Heindl, H.P. Strunk, V.D. Heydemann, and G. Pensl. Micropipes: Hollow tubes in Silicon Carbide. *Physica Status Solidi (a)*, 162:251–262, 1997.

[2] S. Jin, M.J. Bierman, and S.A. Morin. A New Twist on Nanowire Formation: Screw-Dislocation-Driven Growth of Nanowires and Nanotubes. *The Journal of Physical Chemistry Letters*, 1(9):1472–1480, 2010.

[3] S.A. Morin, M.J. Bierman, J. Tong, and S. Jin. Mechanism and Kinetics of Spontaneous Nanotube Growth Driven by Screw Dislocations. *Science*, 328(5977):476–480, 2010.

[4] W.T. Read. *Dislocations in Crystals*. McGraw-Hill, 1953.

[5] O.V. Yazyev and S.G. Louie. Topological defects in graphene: Dislocations and grain boundaries. *Physical Review B*, 81(19):195420, 2010.

[6] F. Ding, A.R. Harutyunyan, and B.I. Yakobson. Dislocation theory of chirality-controlled nanotube growth. *Proceedings of the National Academy of Sciences*, 106(8):2506–2509, 2009.

[7] M. Ozawa, H. Goto, M. Kusunoki, and E. Osawa. Continuously Growing Spiral Carbon Nanoparticles as the Intermediates in the Formation of Fullerenes and Nanoonions. *The Journal of Physical Chemistry B*, 106(29):7135–7138, 2002.

[8] J.P. Hirth and J. Lothe. *Theory of dislocations*. Wiley, New York, 1982.

[9] D. Srivastava, M. Menon, and K. Cho. Computational Nanotechnology with Carbon Nanotubes and Fullerenes. *Computing in Science & Engineering*, 3(4):42–55, 2001.

[10] H.W. Kroto and K. McKay. The formation of quasi-icosahedral spiral shell carbon particles. *Nature*, 331:328–331, 1988.

[11] D. Ugarte. Onion-like graphitic particles. *Carbon*, 33(7):989–993, 1995.

[12] H.W. Kroto, J.R. Heath, S.C. O'Brien, R.F. Curl, and R.E. Smalley. C_{60}: Buckminsterfullerene. *Nature*, 318:162–163, 1985.

[13] P.W. Fowler. How unusual is C_{60}? Magic number for carbon cluster. *Chemical Physics Letters*, 131(6):444–450, 1986.

[14] A. Hirata, M. Igarashi, and T. Kaito. Study on solid lubricant properties of carbon onions produced by heat treatment of diamond clusters or particles. *Tribology International*, 37:899–905, 2004.

[15] H. Sano, N.and Wang, I. Alexandrou, M. Chhowalla, K.B.K. Teo, G.A.J. Amaratunga, and K.J. Iimura. Properties of carbon onions produced by an arc discharge in water. *Journal of Applied Physics*, 92(5):2783, 2002.

[16] E. Koudoumas, O. Kokkinaki, M. Konstantaki, S. Couris, S. Korovin, P. Detkov, V. Kuznetsov, S. Pimenov, and V. Pustovoi. Onion-like carbon and diamond nanoparticles for optical limiting. *Chemical Physics Letters*, 357:336–340, 2002.

[17] S. Iijima. Helical microtubules of graphitic carbon. *Nature*, 354(6348):56–58, 1991.

[18] R. Tenne, L. Margulis, M. Genut, and G. Hodes. Polyhedral and cylindrical structures of tungsten disulphide. *Nature*, 360:444–446, 1992.

[19] Y. Feldman, E. Wasserman, D.J. Srolovitz, and R. Tenne. High-Rate, Gas-Phase Growth of MoS_2 Nested Inorganic Fullerenes and Nanotubes. *Science*, 267(5195):222–225, 1995.

[20] N.G. Chopra, R.J. Luyken, K. Cherrey, V.H. Crespi, M.L. Cohen, S.G. Louie, and A. Zettl. Boron nitride nanotubes. *Science*, 269(5226):966–967, 1995.

[21] B. Liu, Y. Bando, M. Wang, C. Tang, M. Mitome, and D. Golberg. Crystallography and elasticity of individual GaN nanotubes . *Nanotechnology*, 20(18):185705, 2009.

[22] Z. Zhou, J. Zhao, Y. Chen, P. Schleyer, and Z. Chen. Energetics and electronic structures of AlN nanotubes/wires and their potential application as ammonia sensors. *Nanotechnology*, 18(42):424023, 2007.

[23] B. Liu and H.C. Zeng. Direct growth of enclosed ZnO nanotubes. *Nano Research*, 2(3):201–209, 2009.

[24] A. Dev, A. Elshaer, and T. Voss. Optical Applications of ZnO Nanowires. *IEEE Journal of Selected Topics in Quantum Electronics*, 17(4):896–906, 2011.

[25] M. Law, L.E. Greene, J.C. Johnson, R. Saykally, and P. Yang. Nanowire Dye-Sensitized Solar Cells. *Nature Materials*, 4:455–459, 2005.

[26] C.-H. Chen, S.-J. Chang, S.-P. Chang, M.-J. Li, I.-C Chen, T.J. Hsueh, and C.-L. Hsu. Electroluminescence from n-ZnO nanowires/p-GaN heterostructure light-emitting diodes. *Applied Physics Letters*, 95(22):223101, 2009.

[27] H. Kind, H. Yan, B. Messer, M. Law, and P. Yang. Nanowire Ultraviolet Photodetectors and Optical Switches. *Advanced Materials*, 14(2):158–160, 2002.

[28] Nakada K., Fujita M., G. Dresselhaus, and M.S. Dresselhaus. Edge state in graphene ribbons: Nanometer size effect and edge shape dependence. *Physical Review B*, 54(24):17954–17961, 1996.

[29] X. Li, X. Wang, L. Zhang, S. Lee, and H. Dai. Chemically Derived, Ultrasmooth Graphene Nanoribbon Semiconductors. *Science*, 319:1229–1232, 2008.

[30] L. Y. Jiao, L. Zhang, X. Wang, G. Diankov, and H. Dai. Narrow graphene nanoribbons from carbon nanotubes. *Nature*, 458:877–880, 2009.

[31] L. Jiao, X. Wang, G. Diankov, H. Wang, and H. Dai. Facile Synthesis of High-Quality Graphene Nanoribbons. *Nature Nanotechnology*, 5:321–325, 2010.

[32] P. Zhao, J. Chauhan, and J. Guo. Computational Study of Tunneling Transistor Based on Graphene Nanoribbon. *Nano Letters*, 9(2):684–688, 2009.

[33] E. Akatyeva, J. Y. Huang, and T. Dumitrică. Edge-Mediated Dislocation Processes in Multishell Carbon Nano-Onions? *Physical Review Letters*, 105(10):106102, 2010.

[34] D.-B. Zhang, E. Akatyeva, and T. Dumitrică. Helical BN and ZnO nanotubes with intrinsic twisting: An objective molecular dynamics study. *Physical Review B*, 84(11):115431, 2011.

[35] E. Akatyeva and T. Dumitrică. Eshelby Twist and Magic Helical Zinc Oxide Nanowires and Nanotubes. *Physical Review Letters*, 109(3):035501, 2012.

[36] E. Akatyeva, L. Kou, I. Nikiforov, Th. Frauenheim, and T. Dumitrică. Electrically Active Screw Dislocations in Helical ZnO and Si Nanowires and Nanotubes. *ACS Nano*, 6(11):10042–10049, 2012.

[37] E. Akatyeva and T. Dumitrică. Chiral graphene nanoribbons: Objective molecular dynamics simulations and phase transition modeling. *Journal of Chemical Physics*, 137(23):234702, 2012.

[38] A. Kelly and G.W. Groves. *Crystallography and Crystal Defects*. Logman, London, 1970.

[39] F.C. Frank. Capillary Equilibria of Dislocated Crystals. *Acta Crystallographica*, 4:497–501, 1951.

[40] J.D. Eshelby. Screw Dislocations in Thin Rods. *Journal of Applied Physics*, 24(2):176–179, 1953.

[41] J.D. Eshelby. The twist in a crystal whisker containing a dislocation. *Philosophical Magazine*, 3(29):440–447, 1958.

[42] G.W. Sears. Twist in Lithium Fluoride Whiskers. *The Journal of Chemical Physics*, 31(1):53–54, 1959.

[43] G.W. Sears, R.C. DeVries, and C. Huffine. Twist in Alumina Whiskers. *The Journal of Chemical Physics*, 34(6):2142–2143, 1961.

[44] M.J. Bierman, Y.K Albert Lau, A.V. Kvit, A.L. Schmitt, and S. Jin. Dislocation-Driven Nanowire Growth and Eshelby Twist. *Science*, 320(5879):1060–1063, 2008.

[45] J. Zhu, H. Peng, A.F. Marshall, D.M. Barnett, W.D. Nix, and Y. Cui. Formation of chiral branched nanowires by the Eshelby Twist. *Nature Nanotechnology*, 3:477–481, 2008.

[46] K. Yoshida. Twists and Hollow Dislocations in KCl Tubular Whiskers. *Japanese Journal of Applied Physics*, 3(10):565–571, 1964.

[47] F.C. Frank. The influence of dislocations on crystal growth. *Discussions of the Faraday Society*, 5:48–54, 1949.

[48] W.K. Burton, N. Cabrera, and F.C. Frank. The Growth of Crystals and the Equilibrium Structure of their Surfaces. *Philosophical Transactions of the Royal Society A*, 243:299–358, 1951.

[49] F.H. Horn. Spiral Growth on Graphite. *Nature*, 170:581, 1952.

[50] B.T. Kelly. *Physics of Graphite*. Applied Science, London, 1981.

[51] A.J. Stone and D.J. Wales. Theoretical studies of icosahedral C_{60} and some related species. *Chemical Physics Letters*, 128(5):501–503, 1986.

[52] F. Ding, K. Jiao, M. Wu, and B.I. Yakobson. Pseudoclimb and Dislocation Dynamics in Superplastic Nanotubes. *Physical Review Letters*, 98(7):075503, 2007.

[53] T. Dumitrica, M. Hua, and B.I. Yakobson. Symmetry-, time-, and temperature-dependent strength of carbon nanotubes. *Proceedings of the National Academy of Sciences*, 103(16):6105–6109, 2006.

[54] M. Marchand, C. Journet, D. Guillot, J.-M. Benoit, B.I. Yakobson, and S.T. Purcell. Growing a Carbon Nanotube Atom by Atom: "And Yet It Does Turn". *Nano Letters*, 9(8):2961–2966, 2009.

[55] T. Belytschko, S.P. Xiao, G.C. Schatz, and R.S. Ruoff. Atomistic simulations of nanotube fracture. *Physical Review B*, 65(23):235430, 2002.

[56] S. Zhang, S.L. Mielke, R. Khare, D. Troya, R.S. Ruoff, G.C. Schatz, and T. Belytschko. Mechanics of defects in carbon nanotubes: Atomistic and multiscale simulations. *Physical Review B*, 71(11):115403, 2005.

[57] G. Cao and X. Chen. Buckling of single-walled carbon nanotubes upon bending: Molecular dynamics simulations and finite element method. *Physical Review B*, 73(15):155435, 2006.

[58] D.-B. Zhang, M. Hua, and T. Dumitrică. Stability of polycrystalline and wurtzite Si nanowires via symmetry-adapted tight-binding objective molecular dynamics. *The Journal of Chemical Physics*, 128:084104, 2008.

[59] B.J. Alder and T.E. Wainwright. Studies in Molecular Dynamics. I. General Method. *Journal of Chemical Physics*, 31(2):459–466, 1959.

[60] H.C. Andersen. Molecular dynamics simulations at constant pressure and/or temperature. *The Journal of Chemical Physics*, 72:2384, 1980.

[61] D. Frenkel and B. Smit. *Understanding molecular simulation : from algorithms to applications*. Academic Press, London, 2002.

[62] P. Deak, T. Frauenheim, and M.R. Pederson. *Computer simulation of materials at atomic level*. Chichester : Wiley-VCH, Berlin, 2000.

[63] M.S. Daw and M.I. Baskes. Embedded-atom method: Derivation and application to impurities, surfaces, and other defects in metals. *Physical Review B*, 29(12):6443–6453, 1984.

[64] F.H. Stillinger and T.A. Weber. Computer simulation of local order in condensed phases of silicon. *Physical Review B*, 31(8):5262–5271, 1985.

[65] D.W. Brenner, O.A. Shenderova, J.A. Harrison, S.J. Stuart, B. Ni, and S.B. Sinnott. A second-generation reactive empirical bond order (REBO) potential energy expression for hydrocarbons. *Journal of Physics: Condensed Matter*, 14(4):783802, 2002.

[66] J. Tersoff. New empirical model for the structural properties of silicon. *Physical Review Letters*, 56(6):632–635, 1986.

[67] J. Tersoff. Empirical Interatomic Potential for Carbon, with Applications to Amorphous Carbon. *Physical Review Letters*, 61(25):2879–2882, 1988.

[68] G.C. Abell. Empirical chemical pseudopotential theory of molecular and metallic bonding. *Physical Review B*, 31(10):6184–6196, 1985.

[69] D.W. Brenner. Empirical potential for hydrocarbons for use in simulating the chemical vapor deposition of diamond films. *Physical Review B*, 42(15):9458–9471, 1990.

[70] S. Irle, Y. Ohta, Y Okamoto, A. J. Page, Y. Wang, and K. Morokuma. Milestones in Molecular Dynamics Simulations of Single-Walled Carbon Nanotube Formation: A Brief Critical Review. *Nano Research*, 2:755–767, 2009.

[71] A. Siber. Energies of sp^2 carbon shapes with pentagonal disclinations and elasticity theory. *Nanotechnology*, 17:3598–3606, 2006.

[72] B.-W. Jeong, J.-K. Lim, and S.B. Sinnott. Torsional stiffening of carbon nanotube systems. *Applied Physics Letters*, 91:093102, 2007.

[73] J.E. Lennard-Jones. Cohesion. *The Proceedings of the Physical Society*, 43:462–482, 1931.

[74] M. Born and K. Huang. *Dynamical Theory of Crystal Lattices*. Oxford University Press, New York, 1959.

[75] J. Tersoff. Energies of fullerenes. *Physical Review B*, 46(23):15546–15549, 1992.

[76] K.N. Kudin, G.E. Scuseria, and B.I. Yakobson. C_2F, BN, and C nanoshell elasticity from ab initio computations. *Physical Review B*, 64(23):235406, 2001.

[77] C.H. Xu, C.Z. Wang, C.T. Chan, and K.M. Ho. A transferable tight-binding potential for carbon. *Journal of Physics: Condensed Matter*, 4(28):6047–6054, 1992.

[78] D. Porezag, T. Frauenheim, T. Köhler, G. Seifert, and R. Kaschner. Construction of tight-binding-like potentials on the basis of density-functional theory: Application to carbon. *Physical Review B*, 51(19):12947–12957, 1995.

[79] V. Sankaran, K.W. Kim, and G.J. Iafrate. Tight-binding study of optical properties in short-period $In_{0.53}Ga_{0.47}As/InP$ superlattices. *Physical Review B*, 53(11):6939–6942, 1996.

[80] M. Born and R. Oppenheimer. Zur Quantentheorie der Molekeln. *Annalen der Physik*, 389(20):457–484, 1927.

[81] W.A. Harrison. *Electronic structure and the properties of solids: The physics of the chemical bond*. Freeman, San Francisco, 1980.

[82] R.G. Parr and W. Yang. *Density-functional theory of atoms and molecules*. Oxford University Press, New York, 1989.

[83] E. Runge and E.K.U. Gross. Density-Functional Theory for Time-Dependent Systems. *Physical Review Letters*, 52(12):997–1000, 1984.

[84] J.C. Slater. Atomic Shielding Constants. *Physical Review B*, 36(1):5764, 1930.

[85] T. Frauenheim, F. Weich, T. Köhler, S. Uhlmann, D. Porezag, and G. Seifert. Density-functional-based construction of transferable nonorthogonal tight-binding potentials for Si and SiH. *Physical Review B*, 52(15):11492–11501, 1995.

[86] J. Widany, Th. Frauenheim, and W.R.L. Lambrecht. Investigation of the stability of the hexagonal–cubic born nitride prism interface. *Journal of Materials Chemistry*, 6(5):899–901, 1996.

[87] C. Fisker and T.G. Pedersen. Density-functional based tight-binding modeling of ZnO structures. *Physica Status Solidi B*, 246(2):354–360, 2009.

[88] F. Decremps, F. Datchi, A.M. Saitta, A. Polian, S. Pascarelli, A.D. Cicco, J.P. Itié, and Baudelet F. Local structure of condensed zinc oxide. *Physical Review B*, 68(10):104101, 2003.

[89] T. Dumitrică and R.D. James. Objective molecular dynamics. *Journal of the Mechanics and Physics of Solids*, 55(10):2206–2236, 2007.

[90] R.D. James. Objective Structures. *Journal of the Mechanics and Physics of Solids*, 54:2354–2390, 2006.

[91] J.Y. Huang, F. Ding, K. Jiao, and B.I. Yakobson. Self-Templated Growth of Carbon-Nanotube Walls at High Temperatures. *Small*, 3(10):1735–1739, 2007.

[92] J.Y. Huang, F. Ding, and B.I. Yakobson. Dislocation Dynamics in Multiwalled Carbon Nanotubes at High Temperatures. *Physical Review Letters*, 100(3):035503, 2008.

[93] I. Suarez-Martinez, G. Savini, G. Haffenden, J.-M. Campanera, and M.I. Heggie. Dislocations of Burgers vector $c/2$ in graphite. *Physica Status Solidi (c)*, 4(8):2958–2962, 2007.

[94] J.Y. Huang. In Situ Observation of Quasimelting of Diamond and Reversible Graphite-Diamond Phase Transformations. *Nano Letters*, 7(8):2335–2340, 2007.

[95] L. Sun, A.V. Krasheninnikov, T. Ahlgren, K. Nordlund, and F. Banhart. Plastic Deformation of Single Nanometer-Sized Crystals. *Physical Review Letters*, 101(15):156101, 2008.

[96] F. Banhart and P.M. Ajayan. Carbon onions as nanoscopis pressure cells for diamond formation. *Nature*, 382:433–435, 1996.

[97] Y. Gan and F. Banhart. The Mobility of Carbon Atoms in Graphitic Nanoparticles Studied by the Relaxation of Strain in Carbon Onions. *Advanced Materials*, 20(24):4751–4754, 2008.

[98] L.D. Landau and E.M. Lifshitz. *Theory of Elasticity*. Pergamon, Oxford, 1986.

[99] R. Tenne. Inorganic nanotubes and fullerene-like nanoparticles. *Nature Nanotechnology*, 1:103–111, 2006.

[100] X. Liu, X. Wu, H. Cao, and R.P.H. Chang. Growth mechanism and properties of ZnO nanorods synthesized by plasma-enhanced chemical vapor deposition. *Journal of Applied Physics*, 95(6):3141–3147, 2004.

[101] P. Yang, H. Yan, S. Mao, R. Russo, J. Johnson, R. Saykally, N. Morris, J. Pham, R. He, and H.-J. Choi. Controlled growth of ZnO nanowires and their optical properties. *Advanced Functional Materials*, 12(5):323–331, 2002.

[102] G.-W. She, X.-H. Zhang, W.-S. Shi, X. Fan, J.C Chang, C.-S. Lee, S.-T. Lee, and C.-H Liu. Controlled synthesis of oriented single-crystal ZnO nanotube arrays on transparent conductive substrates. *Applied Physics Letters*, 92(5):053111, 2008.

[103] S.A. Morin and S. Jin. Screw Dislocation-Driven Epitaxial Solution Growth of ZnO Nanowires Seeded by Dislocation in GaN Substrates. *Nano Letters*, 10(9):3459–3463, 2010.

[104] F. Meng, S.A. Morin, and S. Jin. Rational Solution Growth of α-FeOOH Nanowires Driven by Screw Dislocations and Their Conversion to α-Fe_2O_3 Nanowires. *Journal of the American Chemical Society*, 133(22):8408–8411, 2011.

[105] D.-B. Zhang, R.D. James, and T. Dumitrică. Dislocation onset and nearly axial glide in carbon nanotubes under torsion. *Journal of Chemical Physics*, 130(7):071101, 2009.

[106] R. Rurali and E. Hernández. Trocadero: a multiple-algorithm multiple-model atomistic simulation program. *Computational Materials Science*, 28(2):85–106, 2003.

[107] Z. Zhou, Y. Li, L. Liu, Y. Chen, S.B. Zhang, and Z. Chen. Size- and Surface-dependent Stability, Electronic Properties, and Potential as Chemical Sensors: Computational Studies on One-dimensional ZnO Nanostructures. *Journal of Physical Chemistry C*, 112(36):13926–13931, 2008.

[108] D.-B. Zhang, T. Dumitrică, and G. Seifert. Helical Nanotube Structures of MoS_2 with Intrinsic Twisting: An Objective Molecular Dynamics Study. *Physical Review Letters*, 104(6):065502, 2010.

[109] D Teich, T. Lorenz, J.-O. Joswig, G. Seifert, D.-B. Zhang, and T. Dumitrică. Structural and Electronic Properties of Helical TiS_2 Nanotubes Studied with Objective Molecular Dynamics. *Journal of Physical Chemistry C*, 115(14):6392–6396, 2011.

[110] D.G. Vercosa, E.B. Barros, A.G Souza Filho, J. Mendes Filho, Ge.G. Samsonidze, R. Saito, and M.S. Dresselhaus. Torsional instability of chiral carbon nanotubes. *Physical Review B*, 81(16):165430, 2010.

[111] R. Saito, G. Dresselhaus, and M.S. Dresselhaus. *Physical properties of carbon nanotubes*. Imperial College Press, London, 1998.

[112] D.-B. Zhang, E. Akatyeva, and T. Dumitrică. Bending Ultrathin Graphene at the Margins of Continuum Mechanics. *Physical Review Letters*, 106(25):255503, 2011.

[113] L.H.G. Tizei, A.J. Craven, L.F. Zagone, M. Tence, O. Stephan, T. Chiaramonte, M.A. Cotta, and Ugarte D. Enhanced Eshelby Twist on Thin Wurtzite InP Nanowires and Measurement of Local Crystal Rotation. *Physical Review Letters*, 107(19):195503, 2011.

[114] J.H. Song, X.D. Wang, E. Riedo, and Z.L. Wang. Elastic Property of Vertically Aligned Nanowires. *Nano Letters*, 5(10):1954–1958, 2005.

[115] G. Stan, C.V. Ciobanu, P.M. Parthangal, and R.F. Cook. Diameter-Dependent Radial and Tangential Elastic Moduli of ZnO Nanowires. *Nano Letters*, 7(12):3691–3697, 2007.

[116] H. Pan and Y.P. Feng. Semiconductor Nanowires and Nanotubes: Effects of Size and Surface-to-Volume Ratio. *ACS Nano*, 2(11):2410–2414, 2008.

[117] H. Xu, R.Q. Zhang, X. Zhang, A.L. Rosa, and Th. Frauenheim. Structural and electronic properties of ZnO nanotubes from density functional calculations. *Nanotechnology*, 18(48):485713, 2007.

[118] W. Fan, H. Xu, A.L. Rosa, Th. Frauenheim, and R.Q. Zhang. First-principles calculations of reconstructed [0001] ZnO nanowires. *Physical Review B*, 76(7):073302, 2007.

[119] I. Nikiforov, D.-B. Zhang, and T. Dumitrică. Screw Dislocation in $< 100 >$ Silicon Nanowires: An Objective Molecular Dynamics Study. *The Journal of Physical Chemistry Letters*, 2(20):2544–2548, 2011.

[120] N.H. Moreira, G. Dolgonos, B. Aradi, A.L. Rosa, and Th. Frauenheim. Toward an Accurate Density-Functional Tight-Binding Description of Zinc-Containing Compounds. *Journal of Chemical Theory and Computation*, 5(3):605–614, 2009.

[121] B. Meyer and D. Marx. Density-Functional Study of the Structure and Stability of ZnO Surfaces. *Physical Review B*, 67(3):035403, 2003.

[122] A. Wander and N.M. Harrison. An ab-initio study of ZnO (11$\bar{2}$0). *Surface Science Letters*, 468:L851–L855, 2000.

[123] T.B. Bateman. Elastic Moduli of Single-Crystal Zinc Oxide. *Journal of Applied Physics*, 33(11):3309, 1962.

[124] J.-A. Yan, L. Yang, and M.Y. Chou. Size and Orientation Dependence in the Electronic Properties of Silicon Nanowires. *Physical Review B*, 76(11):115319, 2007.

[125] S.C. Erwin, L. Zu, M.I. Haftel, Al.L. Efros, T.A. Kennedy, and D.J. Norris. Doping Semiconductor Nanocrystals. *Nature*, 436:91–94, 2005.

[126] M. Nolan, S. O'Callaghan, G. Fagas, J.C. Greer, and Th. Frauenheim. Silicon Nanowire Band Gap Modification. *Nano Letters*, 7(1):34–38, 2007.

[127] Y. Yang, X.H. Yan, Y. Xiao, and D. Lu. Size-Dependent Strain Effects on Electronic and Optical Properties of ZnO Nanowires. *Applied Physics Letters*, 97(3):033106, 2010.

[128] M. Huang, C.S. Ritz, B. Novakovic, D. Yu, Y. Zhang, F. Flack, D.E. Savage, P.G. Evans, I. Knezevic, F. Liu, and M.G. Lagally. Mechano-Electronic Superlattices in Silicon Nanoribbons. *ACS Nano*, 3(3):721–727, 2009.

[129] M.H. Huang, S. Mao, H. Feick, H. Yan, Y. Wu, H. Kind, E. Weber, R. Russo, and P. Yang. Room-Temperature Ultraviolet Nanowire Nanolasers. *Science*, 292(5523):1897–1899, 2001.

[130] H. F. Matare. *Defect Electronics in Semiconductors*. Wiley-Interscience, New York, 1971.

[131] E. Müller, D. Gerthsen, P. Brückner, F. Scholz, Th. Gruber, and A. Waag. Probing the Electrostatic Potential of Charged Dislocations in n-GaN and n-ZnO Epilayers by Transmission Electron Holography. *Physical Review B*, 73(24):245316, 2006.

[132] L. Yang and J. Han. Electronic Structure of Deformed Carbon Nanotube. *Physical Review Letters*, 85(1):154–157, 2000.

[133] T Dumitrică, S Kodambaka, and S. Jun. Synthesis, electromechanical characterization, and applications of graphene nanostructures. *Nanophotonics*, 6(1):064501, 2012.

[134] A. Chuvilin, E. Bichoutskaia, M. C. Gimenez-Lopez, T. W. Chamberlain, G. A. Rance, N. Kuganathan, J. Biskupek, U. Kaiser, and A. N. Khlobystov. Self-Assembly of a Sulphur-Terminated Graphene Nanoribbon within a Single-Walled Carbon Nanotube. *Nature Materials*, 10:687–692, 2011.

[135] A.V. Talyzin, I.V. Anoshkin, A.V. Krasheninnikov, R.M. Nieminen, A.G. Nasibulin, H. Jiang, and E. I. Kauppinen. Synthesis of Graphene Nanoribbons Encapsulated in Single-Walled Carbon Nanotubes. *Nano Letters*, 11(10):4352–4356, 2011.

[136] O. Hod and G.E. Scuseria. Electromechanical Properties of Suspended Graphene Nanoribbons. *Nano Letters*, 9(7):2619–2622, 2009.

[137] V.B. Shenoy, S.D. Reddy, A. Ramasubramaniam, and Y.W. Zhang. Edge-Stress-Induced Warping of Graphene Sheets and Nanoribbons. *Physical Review Letters*, 101(24):245501, 2008.

[138] B. Huang, M. Liu, N. Su, J. Wu, W. Duan, Gu B., and Liu F. Quantum Manifestations of Graphene Edge Stress and Edge Instability: A First-Principles Study. *Physical Review Letters*, 102(16):166404, 2009.

[139] P. Wagner, C.P. Ewels, V.V. Ivanovskaya, P.R Briddon, A. Pateau, and B. Humbert. Ripple edge engineering of graphene nanoribbons. *Physical Review B*, 84(13):134110, 2011.

[140] D. Gunlycke, J. Li, J.W. Mintmire, and C.T. White. Edges Bring New Dimension to Graphene Nanoribbons. *Nano Letters*, 10(9):3638–3642, 2010.

[141] L. Tapaszto, T. Dumitrică, S.J. Kim, P. Nemes-Incze, C. Hwang, and L. P. Biro. Breakdown of continuum mechanics for nanometre-wavelength rippling of graphene. *Nature Physics*, 8:739–742, 2012.

[142] D.-B. Zhang and T. Dumitrică. Role of Effective Tensile Strain in Electromechanical Response of Helical Graphene Nanoribbons with Open and Closed Armchair Edges. *Physical Review B*, 85(3):035445, 2012.

[143] D.-B. Zhang and T. Dumitrică. Effective-Tensional-Strain-Driven Bandgap Modulations in Helical Graphene Nanoribbons. *Small*, 7(8):1023–1027, 2011.

[144] D.-B. Zhang, R.D James, and T. Dumitrică. Electromechanical characterization of carbon nanotubes in torsion via symmetry adapted tight-binding objective molecular dynamics. *Physical Review B*, 80(11):115418, 2009.

[145] I.V. Lebedeva, A.M. Popov, A.A. Knizhnik, A.N. Khlobystov, and B.V. Potapkin. Chiral graphene nanoribbon inside a carbon nanotube: ab initio study. *Nanoscale*, 4:4522–4529, 2012.

[146] L.D. Landau and E.M Lieshitz. *Statistical Physics*. Pergamon, Oxford, 1980.

[147] R.A. Alduhaileb, K. Xie, J.C. Myers, V.M. Ayres, B.W. Jacobs, K. McElroy, T. Bieler, M. Crimp, X. Fan, R.M. Ronningen, A.F. Zeller, T. Baumann, and A. Hirata. Responses of Carbon Onions to High Energy Heavy Ion Irradiation. *MRS Proceedings*, 1298, 2011.

[148] B.W. Jacobs, M.A. Crimp, K. McElroy, and V.M. Ayres. Nanopipes in Gallium Nitride Nanowires and Nanorods. *Nano Letters*, 8(12):4353–4358, 2008.

[149] D. Maestre, D. Haussler, A. Cremades, W. Jager, and J. Piqueras. Nanopipes in In_2O_3 Nanorods Grown by a Thermal Treatment. *Crystal Growth and Design*, 11(4):1117–1121, 2011.

[150] S. Hacialioglu, F. Meng, and S. Jin. Facile and mild solution synthesis of Cu_2O nanowires and nanotubes driven by screw dislocations. *Chemical Communications*, 48(8):1174–1176, 2012.

[151] H. Wu, F. Meng, L. Li, S. Jin, and G. Zheng. Dislocation-Driven CdS and CdSe Nanowire Growth. *ACS Nano*, 6(5):4461–4468, 2012.

[152] M. Elstner, D. Porezag, G. Jungnickel, J. Elsner, M. Haugk, Th. Frauenheim, S. Suhai, and G. Seifert. Self-consistent-charge density-functional tight-binding

method for simulations of complex materials properties. *Physical Review B*, 58(11):7260–7268, 1998.

[153] S. Lakshmi, S. Roche, and G. Cuniberti. Spin-valve effect in zigzag graphene nanoribbons by defect engineering. *Physical Review B*, 80(19):193404, 2009.

[154] J.C. Slater and G.F. Koster. Simplified LCAO Method for the Periodic Potential Problem. *Physical Review*, 94(6):1498–1524, 1954.

Appendix A

Acronyms and abbreviations

For convenience some minimal number of acronyms have been used in this thesis. This appendix presents a table of acronyms and their meaning.

Table A.1: List of used acronyms and abbreviations.

Acronym	Meaning
C	Carbon
ZnO	Zinc oxide
H	Hydrogen
F	Fluorine
MD	Molecular Dynamics
REBO	Reactive empirical bond-order
TB	Tight-binding
DFTB	Density-functional tight-binding
PBC	Periodic boundary conditions
OBC	Objective boundary conditions
NT	Nanotube
SWNT	Singe-walled nanotube
NW	Nanowire
GNR	Graphene nanoribbon
SCC	Self-consistent charge

Appendix B

Matrix element derivatives

The form of the atomic matrix elements has been given by Slater and Koster [154]. The derivatives of these matrix elements, containing d orbitals, are presented in the Tables B.1, B.2, and B.3 as functions of the direction cosines, $l = x/r$, $m = y/r$, $n = z/r$. Some of the derivatives, that can be found by permuting indices and variables, are not shown in these tables. The following notation is used here: $E_{\alpha,\alpha'}$ is the energy integral, $V_{l'dm'} = \eta_{l'dm'} \frac{\hbar^2 r_d^{3/2}}{m r^{7/2}}$ and $V_{ddm'} = \eta_{ddm'} \frac{\hbar^2 r_d^3}{m r^5}$ are the matrix elements, where $l^{'}$ and $m^{'}$ denote the atomic orbital (s, p) and the bonding type (σ, π, δ), respectively.

Table B.1: The sd matrix element derivatives.

$\frac{\partial E_{s,xy}}{\partial x}$	$\sqrt{3}m\left[\frac{dV_{sd\sigma}}{dr}l^2 + \frac{V_{sd\sigma}}{r}(1-2l^2)\right]$
$\frac{\partial E_{s,xy}}{\partial z}$	$\sqrt{3}lmn\left[\frac{dV_{sd\sigma}}{dr} - 2\frac{V_{sd\sigma}}{r}\right]$
$\frac{\partial E_{s,x^2-y^2}}{\partial x}$	$\frac{\sqrt{3}}{2}l\left[\frac{dV_{sd\sigma}}{dr}(l^2-m^2) + 2\frac{V_{sd\sigma}}{r}(1+l^2-m^2)\right]$
$\frac{\partial E_{s,x^2-y^2}}{\partial z}$	$\frac{\sqrt{3}}{2}n(l^2-m^2)\left[\frac{dV_{sd\sigma}}{dr} - 2\frac{V_{sd\sigma}}{r}\right]$
$\frac{\partial E_{s,3z^2-r^2}}{\partial x}$	$\frac{1}{2}l\left[\frac{dV_{sd\sigma}}{dr}(3n^2-1) - 6n^2\frac{V_{sd\sigma}}{r}\right]$
$\frac{\partial E_{s,3z^2-r^2}}{\partial z}$	$\frac{1}{2}n\left[\frac{dV_{sd\sigma}}{dr}(3n^2-1) + 6(1-n^2)\frac{V_{sd\sigma}}{r}\right]$

Table B.2: The *pd* matrix element derivatives.

$\frac{\partial E_{x,xy}}{\partial x}$	$\sqrt{3}lm\left[\frac{dV_{pd\sigma}}{dr}l^2+\frac{V_{pd\sigma}}{r}(2-3l^2)\right]+lm\left[\frac{dV_{pd\pi}}{dr}(1-2l^2)-\frac{V_{pd\pi}}{r}(1-6l^2)\right]$
$\frac{\partial E_{x,xy}}{\partial y}$	$\sqrt{3}l^2\left[\frac{dV_{pd\sigma}}{dr}m^2+\frac{V_{pd\sigma}}{r}(1-3m^2)\right]$
	$+\left[\frac{dV_{pd\pi}}{dr}m^2(1-2l^2)+\frac{V_{pd\pi}}{r}(n^2-l^2+6l^2m^2)\right]$
$\frac{\partial E_{x,xy}}{\partial z}$	$\sqrt{3}l^2mn\left[\frac{dV_{pd\sigma}}{dr}-3\frac{V_{pd\sigma}}{r}\right]+mn\left[\frac{dV_{pd\pi}}{dr}(1-2l^2)-\frac{V_{pd\pi}}{r}(1-6l^2)\right]$
$\frac{\partial E_{x,yz}}{\partial x}$	$mnl^2\left[\sqrt{3}\frac{dV_{pd\sigma}}{dr}-2\frac{dV_{pd\pi}}{dr}\right]+\left[\sqrt{3}\frac{V_{pd\sigma}}{r}-2\frac{V_{pd\pi}}{r}\right]mn(1-3l^2)$
$\frac{\partial E_{x,yz}}{\partial y}$	$lnm^2\left[\sqrt{3}\frac{dV_{pd\sigma}}{dr}-2\frac{dV_{pd\pi}}{dr}\right]+\left[\sqrt{3}\frac{V_{pd\sigma}}{r}-2\frac{V_{pd\pi}}{r}\right]ln(1-3m^2)$
$\frac{\partial E_{x,x^2-y^2}}{\partial x}$	$\frac{\sqrt{3}}{2}\left[\frac{dV_{pd\sigma}}{dr}l^2(l^2-m^2)+\frac{V_{pd\sigma}}{r}(3l^2m^2+3l^2-m^2-3l^4)\right]$
	$+\left[\frac{dV_{pd\pi}}{dr}l^2(1-l^2+m^2)+\frac{V_{pd\pi}}{r}(1-3l^2m^2-4l^2+m^2+3l^4)\right]$
$\frac{\partial E_{x,x^2-y^2}}{\partial y}$	$\frac{\sqrt{3}}{2}lm\left[\frac{dV_{pd\sigma}}{dr}(l^2-m^2)-\frac{V_{pd\sigma}}{r}(2+3(l^2-m^2))\right]$
	$+lm\left[\frac{dV_{pd\pi}}{dr}(1-l^2+m^2)+\frac{V_{pd\pi}}{r}(1+3(l^2-m^2))\right]$
$\frac{\partial E_{x,x^2-y^2}}{\partial z}$	$\frac{\sqrt{3}}{2}ln(l^2-m^2)\left[\frac{dV_{pd\sigma}}{dr}-3\frac{V_{pd\sigma}}{r}\right]$
	$+ln\left[\frac{dV_{pd\pi}}{dr}(1-l^2+m^2)-\frac{V_{pd\pi}}{r}(1-3(l^2-m^2))\right]$
$\frac{\partial E_{z,x^2-y^2}}{\partial x}$	$\left[\frac{\sqrt{3}}{2}\frac{dV_{pd\sigma}}{dr}-\frac{dV_{pd\pi}}{dr}\right]ln(l^2-m^2)+\left[\frac{\sqrt{3}}{2}\frac{V_{pd\sigma}}{r}-\frac{V_{pd\pi}}{r}\right]ln(2-3(l^2-m^2))$
$\frac{\partial E_{z,x^2-y^2}}{\partial z}$	$\left[\frac{\sqrt{3}}{2}\frac{dV_{pd\sigma}}{dr}-\frac{dV_{pd\pi}}{dr}\right]n^2(l^2-m^2)+\left[\frac{\sqrt{3}}{2}\frac{V_{pd\sigma}}{r}-\frac{V_{pd\pi}}{r}\right](l^2-m^2)(1-3n^2)$
$\frac{\partial E_{x,3z^2-r^2}}{\partial x}$	$\frac{1}{2}\left[\frac{dV_{pd\sigma}}{dr}l^2(3n^2-1)+\frac{V_{pd\sigma}}{r}\left((3n^2-1)(1-3l^2)-l^2\right)\right]$

Continued on next page

Table B.2 – continued from previous page

	$-\sqrt{3}n^2\left[\frac{dV_{pd\pi}}{dr}l^2+\frac{V_{pd\pi}}{r}(1-3l^2)\right]$
$\frac{\partial E_{x,3z^2-r^2}}{\partial y}$	$\frac{lm}{2}\left[\frac{dV_{pd\sigma}}{dr}(3n^2-1)+\frac{V_{pd\sigma}}{r}(9n^2-1)\right]+\sqrt{3}lmn^2\left[\frac{dV_{pd\pi}}{dr}-3\frac{V_{pd\pi}}{r}\right]$
$\frac{\partial E_{x,3z^2-r^2}}{\partial z}$	$\frac{ln}{2}\left[\frac{dV_{pd\sigma}}{dr}(3n^2-1)+\frac{V_{pd\sigma}}{r}(7-9n^2)\right]+\sqrt{3}ln\left[\frac{dV_{pd\pi}}{dr}n^2+\frac{V_{pd\pi}}{r}(2-3n^2)\right]$
$\frac{\partial E_{z,3z^2-r^2}}{\partial x}$	$\frac{ln}{2}\left[\frac{dV_{pd\sigma}}{dr}(3n^2-1)+\frac{V_{pd\sigma}}{r}(3n^2+1)\right]$
	$+\sqrt{3}ln\left[\frac{dV_{pd\pi}}{dr}(1-n^2)+\frac{V_{pd\pi}}{r}(3n^2-1)\right]$
$\frac{\partial E_{z,3z^2-r^2}}{\partial z}$	$\frac{n^2}{2}\left[\frac{dV_{pd\sigma}}{dr}(3n^2-1)+\frac{V_{pd\sigma}}{r}(1-n^2)(1-9n^2)\right]$
	$+\sqrt{3}\left[\frac{dV_{pd\pi}}{dr}n^2(1-n^2)+\frac{V_{pd\pi}}{r}(1-n^2)(1-3n^2)\right]$

Table B.3: The *dd* matrix element derivatives.

$\frac{\partial E_{xy,xy}}{\partial x}$	$3lm^2\left[\frac{dV_{dd\sigma}}{dr}l^2+\frac{V_{dd\sigma}}{r}2(1-2l^2)\right]$
	$+l\left[\frac{dV_{dd\pi}}{dr}(l^2+m^2-4l^2m^2)+\frac{V_{dd\pi}}{r}2(1-5m^2-l^2+8l^2m^2)\right]$
	$+l\left[\frac{dV_{dd\delta}}{dr}(n^2+l^2m^2)+\frac{V_{dd\delta}}{r}2(m^2-n^2-2l^2m^2)\right]$
$\frac{\partial E_{xy,xy}}{\partial z}$	$3l^2m^2n\left[\frac{dV_{dd\sigma}}{dr}-4\frac{V_{dd\sigma}}{r}\right]$
	$+n\left[\frac{dV_{dd\pi}}{dr}(l^2+m^2-4l^2m^2)-\frac{V_{dd\pi}}{r}2(m^2+l^2-8l^2m^2)\right]$
	$+n\left[\frac{dV_{dd\delta}}{dr}(n^2+l^2m^2)+\frac{V_{dd\delta}}{r}2(1-n^2-2l^2m^2)\right]$
$\frac{\partial E_{xy,yz}}{\partial x}$	$3m^2n\left[\frac{dV_{dd\sigma}}{dr}l^2+\frac{V_{dd\sigma}}{r}(1-4l^2)\right]$
	$+n\left[\frac{dV_{dd\pi}}{dr}l^2(1-4m^2)+\frac{V_{dd\pi}}{r}(1-4m^2-2l^2+16l^2m^2)\right]$

Continued on next page

Table B.3 – continued from previous page

	$+n\left[\frac{dV_{dd\delta}}{dr}l^2(m^2-1)+\frac{V_{dd\delta}}{r}(m^2-1-4l^2m^2+2l^2)\right]$
$\frac{\partial E_{xy,yz}}{\partial y}$	$3lmn\left[\frac{dV_{dd\sigma}}{dr}m^2+\frac{V_{dd\sigma}}{r}2(1-2m^2)\right]$
	$+lmn\left[\frac{dV_{dd\pi}}{dr}(1-4m^2)+\frac{V_{dd\pi}}{r}2(8m^2-5)\right]$
	$+lmn\left[\frac{dV_{dd\delta}}{dr}(m^2-1)+\frac{V_{dd\delta}}{r}4(1-m^2)\right]$
$\frac{\partial E_{xy,x^2-y^2}}{\partial x}$	$\left[\frac{3}{2}\frac{dV_{dd\sigma}}{dr}-2\frac{dV_{dd\pi}}{dr}+\frac{1}{2}\frac{dV_{dd\delta}}{dr}\right]l^2m(l^2-m^2)$
	$+\left[\frac{3}{2}\frac{V_{dd\sigma}}{r}-2\frac{V_{dd\pi}}{r}+\frac{1}{2}\frac{V_{dd\delta}}{r}\right]m(3l^2-m^2-4l^2(l^2-m^2))$
$\frac{\partial E_{xy,x^2-y^2}}{\partial z}$	$\left[\frac{3}{2}\frac{dV_{dd\sigma}}{dr}-2\frac{dV_{dd\pi}}{dr}+\frac{1}{2}\frac{dV_{dd\delta}}{dr}\right]lmn(l^2-m^2)$
	$-\left[\frac{3}{2}\frac{V_{dd\sigma}}{r}-2\frac{V_{dd\pi}}{r}+\frac{1}{2}\frac{V_{dd\delta}}{r}\right]4lmn(l^2-m^2)$
$\frac{\partial E_{yz,x^2-y^2}}{\partial x}$	$\left[\frac{3}{2}\frac{dV_{dd\sigma}}{dr}-2\frac{dV_{dd\pi}}{dr}+\frac{1}{2}\frac{dV_{dd\delta}}{dr}\right]lmn(l^2-m^2)$
	$+\left[\frac{3}{2}\frac{V_{dd\sigma}}{r}-2\frac{V_{dd\pi}}{r}+\frac{1}{2}\frac{V_{dd\delta}}{r}\right]2lmn(1-2(l^2-m^2))$
	$+\left[\frac{dV_{dd\delta}}{dr}-\frac{dV_{dd\pi}}{dr}+2\frac{V_{dd\pi}}{r}-2\frac{V_{dd\delta}}{r}\right]lmn$
$\frac{\partial E_{yz,x^2-y^2}}{\partial z}$	$\left[\frac{3}{2}\frac{dV_{dd\sigma}}{dr}-2\frac{dV_{dd\pi}}{dr}+\frac{1}{2}\frac{dV_{dd\delta}}{dr}\right]mn^2(l^2-m^2)$
	$+\left[\frac{3}{2}\frac{V_{dd\sigma}}{r}-2\frac{V_{dd\pi}}{r}+\frac{1}{2}\frac{V_{dd\delta}}{r}\right]m(l^2-m^2)(1-4n^2)$
	$+\left[\frac{dV_{dd\delta}}{dr}-\frac{dV_{dd\pi}}{dr}\right]mn^2-\left[\frac{V_{dd\pi}}{r}-\frac{V_{dd\delta}}{r}\right]m(1-2n^2)$
$\frac{\partial E_{xy,3z^2-r^2}}{\partial x}$	$\frac{\sqrt{3}}{2}m(3n^2-1)\left[\frac{dV_{dd\sigma}}{dr}l^2+\frac{V_{dd\sigma}}{r}(1-4l^2)\right]$
	$-2\sqrt{3}mn^2\left[\frac{dV_{dd\pi}}{dr}l^2+\frac{V_{dd\pi}}{r}(1-4l^2)\right]-\sqrt{3}\frac{V_{dd\sigma}}{r}l^2m$
	$+\frac{\sqrt{3}}{2}m\left[\frac{dV_{dd\delta}}{dr}l^2(1+n^2)+\frac{V_{dd\delta}}{r}(1+n^2-2l^2-4l^2n^2)\right]$

Continued on next page

Table B.3 – continued from previous page

$\frac{\partial E_{xy,3z^2-r^2}}{\partial z}$	$\frac{\sqrt{3}}{2}lmn\left[\frac{dV_{dd\sigma}}{dr}(3n^2-1)-\frac{V_{dd\sigma}}{r}12n^2+\frac{dV_{dd\delta}}{dr}(1+n^2)-\frac{V_{dd\delta}}{r}4n^2\right]$
	$-2\sqrt{3}lmn\left[\frac{dV_{dd\pi}}{dr}n^2+\frac{V_{dd\pi}}{r}2(1-2n^2)\right]$
$\frac{\partial E_{yz,3z^2-r^2}}{\partial x}$	$\frac{\sqrt{3}}{2}lmn(3n^2-1)\left[\frac{dV_{dd\sigma}}{dr}-4\frac{V_{dd\sigma}}{r}\right]+\sqrt{3}lmn(1-2n^2)\left[\frac{dV_{dd\pi}}{dr}-4\frac{V_{dd\pi}}{r}\right]$
	$-\frac{\sqrt{3}}{2}lmn(l^2+m^2)\left[\frac{dV_{dd\delta}}{dr}-4\frac{V_{dd\delta}}{r}\right]+\sqrt{3}lmn\left[2\frac{V_{dd\pi}}{r}-\frac{V_{dd\sigma}}{r}-\frac{V_{dd\delta}}{r}\right]$
$\frac{\partial E_{yz,3z^2-r^2}}{\partial z}$	$\frac{\sqrt{3}}{2}mn^2(3n^2-1)\left[\frac{dV_{dd\sigma}}{dr}+(1-4n^2)\frac{V_{dd\sigma}}{r}\right]+2\sqrt{3}mn^2\left[\frac{V_{dd\sigma}}{r}-\frac{V_{dd\pi}}{r}\right]$
	$-\frac{\sqrt{3}}{2}mn^2(l^2+m^2)\left[\frac{dV_{dd\delta}}{dr}+(1-4n^2)\frac{V_{dd\delta}}{r}\right]$
	$+\sqrt{3}mn^2(1-2n^2)\left[\frac{dV_{dd\pi}}{dr}+(1-4n^2)\frac{V_{dd\pi}}{r}\right]$
$\frac{\partial E_{x^2-y^2,x^2-y^2}}{\partial x}$	$\left[\frac{3}{4}\frac{dV_{dd\sigma}}{dr}-\frac{dV_{dd\pi}}{dr}+\frac{1}{4}\frac{dV_{dd\delta}}{dr}\right]l(l^2-m^2)^2+l\left[\frac{dV_{dd\pi}}{dr}(l^2+m^2)+\frac{V_{dd\pi}}{r}2n^2\right]$
	$+\left[\frac{3}{4}\frac{V_{dd\sigma}}{r}-\frac{V_{dd\pi}}{r}+\frac{1}{4}\frac{V_{dd\delta}}{r}\right]4l(l^2-m^2)(1-l^2+m^2)+ln^2\left[\frac{dV_{dd\delta}}{dr}-2\frac{V_{dd\delta}}{r}\right]$
$\frac{\partial E_{x^2-y^2,x^2-y^2}}{\partial z}$	$\left[\frac{3}{4}\frac{dV_{dd\sigma}}{dr}-\frac{dV_{dd\pi}}{dr}+\frac{1}{4}\frac{dV_{dd\delta}}{dr}\right]n(l^2-m^2)^2+\left[\frac{dV_{dd\pi}}{dr}-2\frac{V_{dd\pi}}{r}\right]n(l^2+m^2)$
	$-\left[\frac{3}{4}\frac{V_{dd\sigma}}{r}-\frac{V_{dd\pi}}{r}+\frac{1}{4}\frac{V_{dd\delta}}{r}\right]4n(l^2-m^2)^2+n\left[\frac{dV_{dd\delta}}{dr}n^2+\frac{V_{dd\delta}}{r}2(1-n^2)\right]$
$\frac{\partial E_{3z^2-r^2,x^2-y^2}}{\partial x}$	$\sqrt{3}\left[\frac{3}{4}\frac{dV_{dd\sigma}}{dr}-\frac{dV_{dd\pi}}{dr}+\frac{1}{4}\frac{dV_{dd\delta}}{dr}\right]ln^2(l^2-m^2)$
	$+\sqrt{3}\left[\frac{3}{4}\frac{V_{dd\sigma}}{r}-\frac{V_{dd\pi}}{r}+\frac{1}{4}\frac{V_{dd\delta}}{r}\right]2ln^2(1-2l^2+2m^2)$
	$-\frac{\sqrt{3}}{4}\left(\left[\frac{dV_{dd\sigma}}{dr}-\frac{dV_{dd\delta}}{dr}\right]l(l^2-m^2)+\left[\frac{V_{dd\sigma}}{r}-\frac{V_{dd\delta}}{r}\right]2l(1-l^2+m^2)\right)$
$\frac{\partial E_{3z^2-r^2,x^2-y^2}}{\partial z}$	$\sqrt{3}\left[\frac{3}{4}\frac{dV_{dd\sigma}}{dr}-\frac{dV_{dd\pi}}{dr}+\frac{1}{4}\frac{dV_{dd\delta}}{dr}\right]n^3(l^2-m^2)$
	$+\sqrt{3}\left[\frac{3}{4}\frac{V_{dd\sigma}}{r}-\frac{V_{dd\pi}}{r}+\frac{1}{4}\frac{V_{dd\delta}}{r}\right]2n(l^2-m^2)(1-2n^2)$
	$-\frac{\sqrt{3}}{4}n(l^2-m^2)\left[\frac{dV_{dd\sigma}}{dr}-\frac{dV_{dd\delta}}{dr}-2\frac{V_{dd\sigma}}{r}+2\frac{V_{dd\delta}}{r}\right]$

Continued on next page

Table B.3 – continued from previous page

$\frac{\partial E_{3z^2-r^2,3z^2-r^2}}{\partial x}$	$l(3n^2-1)\left[\frac{dV_{dd\sigma}}{dr}\frac{(3n^2-1)}{4}-\frac{V_{dd\sigma}}{r}3n^2\right]$
	$+3l(1-n^2)\left[\frac{dV_{dd\delta}}{dr}\frac{(1-n^2)}{4}+\frac{V_{dd\delta}}{r}n^2\right]$
	$+3ln^2\left[\frac{dV_{dd\pi}}{dr}(1-n^2)-\frac{V_{dd\pi}}{r}2(1-2n^2)\right]$
$\frac{\partial E_{3z^2-r^2,3z^2-r^2}}{\partial z}$	$n(3n^2-1)\left[\frac{dV_{dd\sigma}}{dr}\frac{(3n^2-1)}{4}+\frac{V_{dd\sigma}}{r}3(1-n^2)\right]$
	$+3n(1-n^2)^2\left[\frac{dV_{dd\delta}}{dr}\frac{1}{4}-\frac{V_{dd\delta}}{r}\right]+3n(1-n^2)\left[\frac{dV_{dd\pi}}{dr}n^2+\frac{V_{dd\pi}}{r}2(1-2n^2)\right]$